TECHNISCHE UNIVERSITÄT WIEN

DISSERTATION

Modelling and simulation concepts for fibre reinforced polymers

carried out for the purpose of obtaining the degree of Doctor technicae (Dr. techn.)
under the supervision of

Assoc.Prof. Dipl.-Ing. Dr.techn. Heinz Pettermann
Institute of Lightweight Design and Structural Biomechanics, E317

and co-advised by

Assoc.Prof. Dipl.-Ing. Dr.techn. Melanie Todt
Institute of Lightweight Design and Structural Biomechanics, E317

submitted at TU Wien,
Faculty of Mechanical and Industrial Engineering,
by

Tilen Ceglar, MSc
Mat.Nr.: 01529637
Sechshauser Straße 68-70
1150 Wien

Wien, im Februar 2021 Tilen Ceglar

Affidavit

I declare in lieu of oath, that I wrote this thesis and performed the associated research myself, using only literature cited in this volume. If text passages from sources are used literally, they are marked as such. I confirm that this work is original and has not been submitted elsewhere for any examination, nor is it currently under consideration for a thesis elsewhere.

Vienna, February 2021

Tilen Ceglar

Acknowledgment

This work was carried out in the course of my employment at the Institute of Lightweight Design and Structural Biomechanics (ILSB) at the Vienna University of Technology. First, I want to express my deepest gratitude to my thesis advisor, Assoc. Prof. Heinz Pettermann, for his guidance and valuable feedback in the past years. Numerous discussions we had always helped me focus on the important issues and, most importantly, taught me to think critically and develop new ideas. I also need to thank Assoc. Prof. Melanie Todt for her feedback, which was always on point and very detailed.

Without my colleagues Jan Kaul, Benjamin Werner and Martin Springer all of the long hours in the office would not be the same. They always found time for valuable discussions or just a quick chat, which created a wonderful working environment at the ILSB.

However, this work would not be possible without the support of my family, friends and above all Manca for being the wonderful person she is.

The work presented in Chapters 4, 5 and 6 is funded by the Polymer Competence Center Leoben GmbH (PCCL) within the COMET-program by the Austrian Federal Ministry for Transport, Innovation and Technology (BMVIT), the Austrian Federal Ministry of Digital and Economic Affairs (BMDW), Österreichische Forschungsförderungsgesellschaft mbH (FFG), the Provinces of Styria, Lower Austria and Upper Austria, which is gratefully acknowledged.

Contents

Abstract

The present thesis focuses on the development of efficient methods for modelling the nonlinear behaviour of fibre reinforced composites in the framework of the Finite Element Analysis. Two types of composites – fibre reinforced plastics and fibre reinforced elastomers – are studied with the perspective of structural simulations.

To begin with, delamination in textile laminates is studied by introducing an efficient modelling strategy. A multi-scale embedding method is employed in order to include a detailed representation of the textile plies at the delaminating interface, while the rest of the laminate is modelled with homogenised plies. Except for the cohesive interfaces, the entire laminate is represented with shell elements only. The developed approach is employed to study delamination of 2/2 Twill Weave laminate under the Double Cantilever Beam and Three Point End Notch Flexure test set–up using standard desktop hardware. Delamination is characterized with load–displacement curves, energy release rates and evaluation of the process zones in the cohesive interfaces. The change in the local stiffness at the delamination front due to the laminate's topology and the size of the cohesive process zone translates into a quasi-stepwise reduction of the reaction force, which is in line with the experimental observations found in the literature. The results highlight the high predictive capabilities and exceptional efficiency in terms of the computational effort.

Next, the present work focuses on the effective behaviour of fibre reinforced elastomers. Nonlinear homogenisation by the unit cell approach is used to obtain the effective response of multi-fibre unit cells with random fibre arrangement in the ini-

tial linearised and finite strain regime. In order to predict the effective behaviour of the multi-fibre unit cells, the readily available Holzapfel-Gasser-Ogden (HGO) anisotropic hyperelastic material model is employed. A novel calibration method for the material parameters is developed here, which takes place at the initial or undeformed state of the material. The initial deviatoric elasticity of the HGO model is used to derive relations between the material parameters and the material properties of a transversely isotropic material, such as the shear and the Young's moduli. The latter are estimated using analytical homogenisation method and therefore the calibration avoids any material parameter fitting or numerical homogenisation schemes. The proposed method is successfully verified under various load cases for glass fibre reinforced rubber-like material. The calibrated HGO model is further employed for predicting the effective response of a symmetrical cross-ply laminate unit cell under shear deformations. The results expose the HGO model's limited ability to emulate fibre rotation at moderate stretches. Moreover, the calibrated HGO model is used to simulate wrinkling of thin sheets under tensile loads. Linear eigenvalue analysis with a preload is used to identify the eigenmodes with the smallest positive eigenvalues, which are used as a geometrical imperfection. This way, the wrinkling is predicted at the critical loads and upon further tensile loading, the amplitude of the wrinkles diminishes.

Kurzfassung

Die vorliegende Arbeit konzentriert sich auf die Entwicklung effizienter Methoden zur Modellierung des nichtlinearen Verhaltens von Faserverbundwerkstoffen im Rahmen der Finite-Elemente-Analyse. Zwei Arten von Verbundwerkstoffen - faserverstärkte Thermo- und Duroplaste und faserverstärkte Elastomere - werden unter dem Gesichtspunkt der Struktursimulation untersucht. Zunächst wird die Delamination in textilen Laminaten durch Einführung einer effizienten Modellierungsstrategie untersucht. Eine mehrskalige Einbettungsmethode wird verwendet, um eine detaillierte Darstellung der textilen Lagen an der Delaminationssgrenzfläche zu erhalten, während der Rest des Laminats mit homogenisierten Lagen modelliert wird. Mit Ausnahme der kohäsiven Grenzflächen wird das gesamte Laminat nur durch Schalenelemente beschrieben. Der entwickelte Ansatz wird verwendet um die Delamination von Laminaten mit 2/2 Köperbindung im DCB (Double Cantilever Beam) und Dreipunkt ENF (End Notch Flexure) Testaufbau mit Standard-Desktop-Hardware zu untersuchen. Die Delamination wird mit Kraft-Verschiebungs-Kurven, Energiefreisetzungsraten und der Bewertung der Prozesszonen in den kohäsiven Grenzflächen charakterisiert. Die Änderung der lokalen Steifigkeit an der Delaminationsfront aufgrund der Topologie des Laminats und der Größe der kohäsiven Prozesszone führt zu einer quasi schrittweisen Verringerung der Reaktionskraft, was mit den experimentellen Beobachtungen in der Literatur übereinstimmt. Die Ergebnisse unterstreichen die hohen Vorhersagefähigkeiten und die außergewöhnliche Effizienz im Bezug auf den Berechnungsaufwand.

Als Nächstes konzentriert sich die vorliegende Arbeit auf die effektiven Eigenschaften von faserverstärkten Elastomeren. Die nichtlineare Homogenisierung mit dem Einheitszellenansatz wird verwendet, um die effektive Materialantwort von Mehrfaser-Einheitszellen mit zufälliger Faseranordnung mit linearisierten und großen Verzerrungen zu erhalten. Um das effektive Verhalten der Mehrfaser-Einheitszellen vorherzusagen, wird das leicht zugängliche anisotrope hyperelastische Holzapfel-Gasser-Ogden (HGO) Materialmodell verwendet. Es wird ein neuartiges Kalibrierverfahren für die Materialparameter entwickelt, das im initialen oder unverformten Zustand des Materials erfolgt. Die initiale deviatorische Elastizität des HGO-Modells wird verwendet, um Zusammenhänge zwischen dessen Materialparametern und den Materialeigenschaften eines transversal isotropen Materials abzuleiten, wie z.B. den Schub- oder Elastizitätsmodul. Letztere werden mit Hilfe einer analytischen Homogenisierungsmethode abgeschätzt, und daher vermeidet die Kalibrierung jegliches "fitten" der Materialparameter oder numerische Homogenisierungsmethoden. Die vorgeschlagene Methode wird erfolgreich unter verschiedenen Lastfällen für glasfaserverstärktes gummiartiges Material verifiziert. Das kalibrierte HGO-Modell wird ferner zur Vorhersage der effektiven Eigenschaften einer Einheitszelle eines symmetrischen bidirektional Geleges unter einer Schubverformungen verwendet. Die Ergebnisse zeigen die begrenzte Fähigkeit des HGO-Modells auf, die Faserrotation bei moderaten Dehnungen zu emulieren. Darüber hinaus wird das kalibrierte HGO-Modell zur Simulation der Faltenbildung bei dünnen Schichten unter Zugbelastung verwendet. Eine lineare Eigenwertanalyse wird verwendet, um die Eigenmoden mit den kleinsten positiven Eigenwerten zu identifizieren, die als geometrische Imperfektion aufgebracht werden. Auf diese Weise wird die Faltenbildung bei den kritischen Belastungen vorhergesagt und bei weiterer Zugbelastung nimmt die Amplitude der Falten ab.

Notations

Abbreviations

2D	Two–Dimensional
3D	Three–Dimensional
3ENF	Three-Point End Notched Flexure
5HS	Five Harness Satin
8HS	Eight Harness Satin
BK	Benzeggagh–Kenane
CBT	Corrected Beam Theory
CCM	Compliance Calibration Method
CZ	Cohesive Zone
CZM	Cohesive Zone Model
CSM	Conventional Shell Model
DCB	Double Cantilever Beam
DOF	Degrees Of Freedom
ENF	End Notched Flexure
FEM	Finite Element Method
FRE	Fibre Reinforced Elastomers
HGO	Holzapfel–Gasser–Ogden
UD	Unidirectional
MSM	Multi-Scale laminate Model

MSMI	Multi-Scale laminate model with heterogeneous cohesive Interfaces
MSMID	Multi-Scale laminate model with heterogeneous cohesive Interfaces and Damage law in tows
RVE	Representative Volume Element
UC	Unit Cell
MFUC	Multi-Fibre Unit Cell
SWB	South–West–Bottom
SWT	South–West–Top
SEB	South–East-Bottom
SET	South–East–Top
NWB	North–West–Bottom
NWT	North–West–Top
NEB	North–East-Bottom
NET	North–East–Top
VCCT	Virtual Crack Closure Technique
triso	transversely isotropic
dev	deviatoric
axi	axial
trv	transverse
comb	combined

Scalars

$\alpha^{(m)}$	Material parameter (Ogden hyperelastic model)
δ	Displacement
ε	Component of a strain tensor
λ	Stretch

λ	Eigenvalue
ν	Poisson ration
θ	Angle
$\mu^{(m)}$	Material parameter (Ogden hyperelastic model)
ξ	Viscosity
a	Average delamination length
f	Fibre volume fraction
k_1	Material parameter (HGO)
k_2	Material parameter (HGO)
l	Dimension
$\bar{p}$	Lagrange multiplier
r	Fibre radius
u	Node displacement
$\underline{k}$	Hill's parameter
$\underline{l}$	Hill's parameter
$\underline{m}$	Hill's parameter
$\underline{n}$	Hill's parameter
$\underline{p}$	Hill's parameter
C_{10}	Material parameter (HGO)
$D^{(m)}$	Material parameter (Ogden hyperelastic model)
E	Young's modulus
$\overline{\overline{E}}_1$	Component of HGO strain energy form
G	Shear modulus
K	Bulk modulus
I	Invariant of a tensor
J	Volume change
J^{el}	Elastic volume change

P	Reaction force
S	Shear nominal strength Hashin
U	Effective strain energy
U_d	Damage dissipation energy
X	Nominal strength Hashin
Z	Zener parameter
$\mathscr{G}$	Energy release rate

Vectors

$\mathbf{a}$	Fibre direction
$\mathbf{e}$	Basis vector
$\mathbf{n}$	Principal direction

Tensors

ε	Strain tensor
δ	Kronecker delta
σ	Stress tensor
$\boldsymbol{\sigma}$	Stress tensor
$\boldsymbol{\varepsilon}$	Strain tensor
$\boldsymbol{e}$	Deviatoric strain tensor
$\boldsymbol{s}$	Deviatoric stress tensor
$\mathbf{C}$	Right Cauchy-Green stretch tensor
$\bar{\mathbf{C}}$	Deviatoric right Cauchy-Green stretch tensor
$\bar{\mathbf{D}}_0$	Initial deviatoric elasticity tensor
$\mathbf{E}$	Elasticity tensor
$\mathbf{F}$	Deformation gradient

$\mathbf{I}$	Second order unit tensor
$\mathbf{R}$	Rotational tensor
$\mathscr{I}$	Fourth order unit tensor
$\mathscr{P}$	Projection tensor

Symbols for Operation

$:$	Double contraction
$\otimes$	Dyadic product
$\bar{\mathbf{x}}$	Deviatoric part
$\widehat{x}$	Effective entity
$\langle \mathbf{x} \rangle$	Macroscopic entity
$H(x)$	Heaviside unit step function

Voigt-Nye notation

The Voigt-Nye notation [76] is used to represent higher-order tensors. Due to the symmetry of the stress and the strain tensor they can be represented as vectors in a six-dimensional space

$$\boldsymbol{\sigma} = \begin{pmatrix} \sigma_{11} \\ \sigma_{22} \\ \sigma_{33} \\ \sigma_{12} \\ \sigma_{13} \\ \sigma_{23} \end{pmatrix}, \quad \boldsymbol{\varepsilon} = \begin{pmatrix} \varepsilon_{11} \\ \varepsilon_{22} \\ \varepsilon_{33} \\ 2\varepsilon_{12} \\ 2\varepsilon_{13} \\ 2\varepsilon_{23} \end{pmatrix} . \tag{1}$$

Note that the shear components of the strain tensor are equal to the shear-angles $\gamma_{ij} = 2\varepsilon_{ij}$.

Chapter 1

Introduction

Throughout the history of technological advancement, the development and design of structures have always been restricted with materials and production capabilities. It is the discovery and invention of new materials that fuelled industrial progress. In recent decades it is arguably the composite material that had the biggest impact on how structures can be designed and manufactured. This is certainly true for lightweight design where laminated composite materials have had the biggest success due to their exceptional high stiffness to weight and strength to weight ratio. Moreover, these materials exhibit good fatigue resistance, are weather-proof and can be formed and manufactured in complex shapes. Unsurprisingly, composites such as fibre reinforced plastics (FRP) are being widely used in the aerospace industry. Considering the latest passenger aeroplanes as e.g. the Airbus 350 series, the share of composite materials in total aeroplane structural mass is exceeding 50% [2]. Moreover, even the load carrying structural parts such as the wingbox, are made from laminated FRP composites in the latest generation of commercial aeroplanes. Therefore, detailed knowledge about nonlinear mechanical behaviour of structures made of FRPs under various loading scenarios must be obtained in order to successfully design such components. In particular it is required to determine the load carrying capabilities and often the structural response beyond local material failure. Laminated

FRP exhibit complex failure modes in the form of fibre rupture, matrix cracking and debonding of plies. The latter called delamination is the predominant failure mode in laminates without reinforcement through the thickness [14, 42] and is challenging to visually identify. Clearly, there is a big interest and need for modelling and predicting delamination in laminated structures. The state of the art approach uses the Finite Element Method (FEM), where the main challenge is resolving the complex topology and material behaviour at appropriate length scales in order to configure computationally efficient simulations.

Commonly composite materials have been thought as an alternative to metals and plastics in solid structural applications. However, novel material combinations in composites lead the way for applications, which can substitute not just structures but also mechanisms. A common example are the so called "soft" composites or fibre reinforced elastomers (FRE), where relatively stiff fibres or particles are reinforcing a compliant matrix, e.g. a rubber-like material. FRE materials exhibit load carrying capabilities in specific directions and loading scenarios while being highly flexible under other configurations, hence enabling large deformation of the structure. Such composites are commonly used in robotics, where instead of having a robotic arm with joints and several actuators, a single inflatable structure made from fibre reinforced rubber is used. Thereby, the movement is actuated only by the internal pressure. The layout and orientation of the fibres define the movement of the robotic arm and thereby its operation. FRE material can also be utilized in lightweight deployable structures. The main objective for such structures, e.g. solar panels, is to take as little space as possible during transport and once in place be deployed with a simple actuation. Thereby, FRE material is used for compliant flexure single-piece joints between the panels. These are just a couple of applications, however, the design of FRE components is in general highly dependent of its operation. Experimental characterization of different FRE composite setups with various fibre volume fractions and fibre positions can be very time and cost consuming. Having the tools to tailor the response of FRE composites to the required function in a fast and efficient manner

is essential. FEM simulations provide an established framework for such tasks and can incorporate the predictions of FRE across different length scales. Thereby, FRE can be evaluated in a complete cycle from a material to the structural application.

1.1 Scope of the present work

Chapter 2 reviews the literature on modelling delamination in laminated composites in the framework of FEM, homogenisation of fibre reinforced elastomers, and wrinkling of thin elastic plates under tensile loads.

In Chapter 3 delamination in textile laminates is studied with multi-scale FEM simulations. Thereby, the delamination in textile laminates and the complex interaction between the constituents is studied in order to identify the main mechanisms at work while keeping the computational effort low enough to utilize standard workstation computers. A shell-element based approach is used to create the multi-scale model. Thereby, a microstructure representing textile plies stacked into a laminate is embedded in a conventional composite shell laminate with homogenised material properties. The multi-scale laminate model is simulated in three point end notched flexure and double cantilever beam test set-ups. The multi-scale models are compared with analytical predictions and special emphasis is given to the delamination process and other damage mechanisms within the microstructure.

Chapter 4 studies fibre reinforced elastomers in terms of their macroscopic behaviour. With multi-fibre unit cells the homogenised response is obtained and studied with respect to the fibre volume fraction. An anisotropic hyperelastic material law is employed to predict the homogenised response of the unit cells. Thereby, the material parameters are calibrated using a micromechanical approach for the initial state of the material. Consequently the need for material parameter fitting is minimized. The calibrated material is compared to the effective response of the unit cells under various load cases.

Following the work of calibrating the anisotropic hyperelastic material, the approach is employed in Chapter 5 for predicting the effective behaviour of FRE laminates under different load cases. A large multi-fibre laminate unit cell is used as the benchmark for the behaviour of the homogenised model.

In chapter 6 the focus moves from the homogenisation to the structural response of FRE components. A thin FRE shell under global tension is investigated, which upon stretching beyond the critical load exhibits out-of-plane wrinkling. Thereby, the calibrated material from Chapter 4 is used in the linear eigenvalue analysis with a preload. The obtained eigenmodes are used as geometrical imperfections to estimate the post-buckling behaviour.

Last but not least, Chapter 7 summarises the work presented here, exposes the strengths and weaknesses of the methods employed within, and gives the reader an outlook on how certain problems could be overcome.

Chapter 2

Literature review

2.1 Modelling of delamination in laminated composite structures

The state-of-the-art approach for modelling delamination growth in laminated composites is based on the cohesive zone (CZ) formulation. CZ models use the framework of damage mechanics and fracture mechanics to model the complex damage process occurring at and in-front of the crack tip in the interface of a bi-material compound. Thereby, all in-elastic effects that occur around at the crack tip are inherited into a surface called the cohesive process zone. These models are capable of predicting both onset and propagation of cracks, and therefore, delamination. The constitutive behaviour of CZ models is defined by traction-separation laws, where the damage onset is set by a specific criterion based on maximum tractions, i.e. interface strengths. Once the initiation criterion is reached, the degradation of the interface stiffness is activated. The softening behaviour is controlled by the formulation of the traction-separation law and the critical energy release rate, which is met at complete stiffness degradation. Thereby, new crack surfaces are formed and delamination grows.

Most common CZ formulations are based on the work of Dudgale [30] and Barenblatt [5], which can be related to the Griffith's theory of fracture when the size of the CZ is negligible compared to the characteristic dimensions of the component. In Ref. [46] the CZ approach was first implemented in the framework of FEM, which is able to predict growth of existing crack as well as initiation of new ones. Several earlier application of CZ models presented in Refs. [3, 41, 70, 90, 93] have been successful at predicting delamination growth in laminates under single or mixed-mode conditions and validated with experimental results. There the uni-direction (UD) laminates are modelled as a stack of homogeneous layers with CZ interfaces in between.

Decohesion elements have been developed by Camanho et al [14, 15] based on the CZ formulation for modelling steady-state delamination growth under mixed-mode conditions. Decohesion elements are formulated based on continuum finite elements, which are placed between solid finite elements and have typically very small or zero initial thickness. The damage onset criterion in the CZ is based on the quadratic interaction of interface tractions. Damage onset is followed by softening behaviour defined by the traction-separation law (bi-linear), critical energy release rate, and the mixed-mode ratio at damage onset. Mixed-mode loading is evaluated using a criterion proposed by Benzeggagh and Kenane, cf. [8]. Thereby, the mixed-mode conditions are constant during the softening behaviour. Therefore, this formulation should not be used under variable mode loading as this might not satisfy the Clausius-Duhem inequality. Based on the decohesion elements [14, 15], cohesive elements are implemented in the FEM code `Abaqus` *(Dassault Systèmes Simulia Corp., Providence, RI, USA)*. Thereby, different traction separation laws, damage onset and propagation criterion, and mixed-mode evaluations can be used.

In Ref. [93] a methodology for predictions of delamination growth under mixed-mode fracture with cohesive elements is proposed. Thereby, the changes in the local mode ratio during the evolution of damage under mixed-mode loading are captured. It is shown that even under loading, which has according to linear elastic fracture mechan-

ics a constant mode, variations can occur and consequently effects the determination of the energy dissipation.

In order to obtain mesh-independent results the discretization of the CZ interface should be fine enough, that the tractions are captured correctly. Thereby, the discretizing elements should be relatively small compared to the size of the CZ. The length of the CZ is defined from the crack tip to the point of damage onset, e.g. where the maximum traction is reached for single mode delamination. An assessment of the cohesive process zone length based on the material properties is given in Ref. [100]. In Ref. [41] a proposal for the characteristic length of cohesive elements is given based on the interface properties for mode I and II. Thereby, sufficient number of elements should be ensured within the cohesive process zone in order to accurately capture the damage onset and evolution. However, in Ref. [92] it is shown that the cohesive process zone length can be artificially increased with lowering the interfacial strength while still accurately predicting the delamination growth when the critical energy release rate remains the same. In addition, an estimation of minimum initial stiffness of the CZ interface is given, which ensures that the effects on the global compliance are negligible.

In terms of modelling laminated composites, using shell elements for discretization of plies is a preferable choice due to the typically very small thickness compared to the other dimensions. The so-called stacked shell approach models laminates with stacking shell layers with cohesive elements in between, cf. Ref. [83]. Thereby, the cohesive elements with non-zero geometrical thickness connect the nodes on the shell reference planes of the shell layers via tie constraints or by sharing the nodes. The latter results in the same planar discretization of the CZ interface as the shell layers. The stacked shell approach is beneficial when the plies are modelled as homogeneous with effective properties.

Multi-scale modelling

In Ref. [98] a multi-scale finite element analysis of mode I delamination growth in a fabric laminate has been presented. The detailed meso–scale structure of five harness satin (5HS) weave fabric is embedded at the initial crack tip by a macro–scale homogeneous model with orthotropic effective properties. The unit cell representing the 5HS weave fabric geometry at the meso–scale is discretized using continuum finite elements for yarns and matrix. Contact elements with bilinear CZ law are used to model the delamination path between the yarns and the matrix. Moreover, CZ contact elements are planted in a coarse grid around the yarn to represent the cured matrix and enable separation of yarns in the individual ply. Thereby, the model predicts weft yarn bridging during delamination which, besides the inter-ply delamination, account for the major toughening mechanism that causes stress relaxation. However, to keep the model size manageable in terms of computational effort, the meso–scale model was limited to only 4 warp and 5 weft yarns and a single ply on each sublaminate, while shorting the whole laminate and applying a correction factor.

2.2 Effective behaviour of fibre reinforced elastomers

FRE composites exhibit complex geometry and interactions between its constituents at the microscale. In order to bridge the length scales and to predict the effective macroscopic or effective behaviour of heterogeneous materials, several tools have been developed. One of such tools are analytical homogenisation models, which can give useful bounds and estimates of both linear and non-linear composites.

In terms of non-linear composites, important work has been done by Ponte Castañeda [16, 17], who developed an analytical second-order homogenisation framework for non-linear isotropic composites. In Ref. [17] a variational formulation gives bounds and estimation of the effective strain energy density of non-linear composites based on the properties for linear composites with the same microstructure distribution of phases.

Based on the second-order homogenisation framework for nonlinear composites incorporating field fluctuations [18], Ref. [64] derives analytical estimates for the effective behaviour of porous elastomers. The method is applicable to a large class of hyperelastic composites including reinforced and porous rubber.

The second-order homogenisation framework has been applied for fibre reinforced rubbers in Ref. [65, 66]. Thereby, the framework accounts for the evolution of the microstruture, including fibre rotation. The method uses estimates for a comparison composite which is defined by linearization of the constitutive behaviour of the elastomer phases. In Ref. [66] the estimates are applied for elastomer composite reinforced with cylindrical fibres with random distribution under finite deformations. A strong influence of the evolution of the microstructure on the overall behaviour is reported. Additionally, the microstructure evolution also has implications for the overall stability of the composite, when a sufficiently large compressive component of the applied deformation along the axes of the fibres is present. When the fibres are considered as rigid and the interface between the constituents as perfect, the elastomer composite is prone to "lock-up" effects due to the stretching of the polymer chains.

In Ref. [13] homogenisation estimates are proposed for fibre reinforced elastomers with periodic microstructure based on the second-order homogenisation framework. The subtle influence of the distribution, volume fraction and stiffness of the fibre on the effective behaviour and macroscopic instabilities is investigated. Following the same framework, Ref. [1] presents a constitutive model for the effective response of incompressible fibre reinforced elastomers with perfectly aligned and randomly distributed fibres, leading to overall transversely isotropic behaviour. The model provides a generalization of the results in Ref. [65, 66] for plane-strain loading with rigid fibres.

A different homogenisation framework for estimating the effective behaviour of a transversely isotropic fibre reinforced elastomers is derived in Ref. [27]. Thereby, the effective strain energy density function is expressed in terms of the properties of the

incompressible neo-Hookean phases and their spatial distribution. At the initial state of the material, i.e. in the limit of small deformation elasticity, the expression agrees with the Hashin-Shtrikman bounds. Moreover, for a hexagonal unit cell, the estimates capture the behaviour given by numerical micromechanical models undergoing finite deformations under general loading modes.

Another important set of tools are the numerical homogenisation methods, which model the composite geometry at an appropriate length scale and estimate the effective response under different loading conditions. Periodic microfield models such as unit cells with periodic boundary conditions within the framework of FEM have been successful for obtaining valid estimates of the effective behaviour of fibre reinforced elastomers with periodic and random fibre distribution.

In general, unit cells representing fibre reinforced composites with random fibre arrangement are not a rigorous representative volume element (RVE), due to the randomness in the fibre distribution, and therefore, are associated with size effects. In Ref. [56, 57] an elaborate study is presented on the effective response of fibre reinforced rubber composites. Using kinematic, static and mixed uniform boundary conditions, windowing approaches and ensemble averages it is shown that a sufficient unit cells size depends on the quantity of interest, deformation mode and intensity, and the mismatch of the phase properties. Therefore, no estimation of a general sufficient size is given, however, the maximum mismatch in the initial shear modulus of phases is ten, at which the inclusions cannot be considered as rigid compare to the matrix.

In the recent Ref. [63], multi fibre unit cells with random fibre distribution and periodic boundary conditions are utilized to investigate the size effect on the in-plane direction dependency in the small strain regime, where the composite can be approximated as linear elastic, and at larger strains across different fibre volume fractions.

Ref. [72] studies the in-plane deformation of incompressible elastomers uniaxially reinforced with rigid fibres by means of unit cell models. The results of unit cells are taken as quasi-exact and are used to check the accuracy of the second-order homogenisation model with field fluctuations [66] and sequentially laminated composite model developed in Ref. [26]. In case of neo-Hookean matrix and fibres with circular cross-section, both analytical models accurately predicted the behaviour of these FRE. However, in the case of Gent matrices, lock-up effects occur at lower values of the applied stretch which the analytical homogenisation model are unable to predict. In addition, results for the case of elliptical fibres are compared, with the second-order homogenisation model [66] being in good agreement as fibre rotation is included in the model. However, numerical simulations also showed the development of instabilities when all ellipses are oriented with their shortest in-plane axis parallel to the stretching direction.

Constitutive modelling

FRE composites exhibit hyperelastic anisotropic effective behaviour. Surprisingly, within the literature, the first anisotropic hyperelastic constitutive models have been developed with the motivation to model the behaviour of biological tissues such as arterial veins. Thereby, collagen fibres are reinforcing the arterial walls where each layer is treated as a fibre reinforced material. An overview of the numerous formulations of constitutive models for arteries is given in Ref. [53].

A three-axial constitutive law for modelling arteries is proposed in Ref. [20], which is determined from a strain energy function in exponential form. The strain energy density function, named the generalized Fung's form, is based on components of the modified Green strain tensor and a fourth-order tensor of anisotropic material constants. However, in Ref. [48] it is exposed that the generalized Fung's form is not convex for all possible sets of material parameters and therefore strong restrictions on the parameters must be enforced to avoid material instabilities.

A phenomenological constitutive law has been developed in Ref. [49], where the strain energy density function is formulated in terms of invariants of the distortional part of the Green strain tensor. Named as Holzapfel–Gasser–Ogden (HGO) model, the strain energy density function consists of the "isotropic" contribution, defined with a reduced polynomial form, volumetric part and the fibre contribution. Thereby, the fibre main orientation and dispersion can be defined. However, due to the physical nature of collagen fibres, the fibres cannot carry compressive loads, which is implemented in the HGO model. The HGO model incoporates a relatively low number of material parameters, which is preferable when these parameters are fitted to experimental or numerical results.

While within the literature there are more formulations of the strain energy density function for anisotropic hyperelastic materials, the generalized Fung's form and the HGO model are readily available in the FEM code Abaqus.

2.3 Wrinkling of thin elastic sheets under tensile loads

Ref. [80] gives an overview on buckling of elastic structures under tensile loads. A preceding work in Ref. [31] studies the instability of stretched metallic sheets, where buckling occurs as a result of special boundary conditions. Thereby, the thin elastic sheet is clamped on the short edges, which prevents the lateral contraction due to the Poisson's effect. This leads to lateral compressive stresses at a distance from the clamped edges, which causes wrinkling. The paper introduced a diagram with the critical buckling coefficient as a function of the aspect ratio, which allows the estimation of the critical tensile stress in the same way as used for conventional buckling problems.

Ref. [45] considers the wrinkling of highly stretched thin sheets. The authors propose a rational model which accounts for large mid-plane strain. Thereby, a numerical

bifurcation analysis is performed to identify stable solutions, which are compared to the Föppl-von Kármán theory of plates. The proposed method shows that the amplitude of wrinkles decreases towards zero with increasing macroscopic strain. This is in contrast to the Föppl-von Kármán theory which predicts an ever-increasing wrinkling amplitude as the macroscopic strain is increased.

In Ref. [62] the stability boundaries are determined for the wrinkling of highly stretched thin hyperelastic sheets with respect to a given thickness and aspect ratio. Results are compared for the Föppl-von Kármán plate model, a correction of the latter and the effective finite elasticity membrane model based on the incompressible neo-Hookean and the Mooney-Rivlin materials, respectively.

In Ref. [89] a model for finite bending and stretching of thin sheets is derived from the Koiter's nonlinear plate theory. The model is used in numerical analyses of wrinkling in thin sheets under tensile loads and compared to the experimental data. The proposed approach is applicable to a wide variety of problems without prior knowledge of the solution, e.g. no eigenmodes are required to obtain the wrinkling and post-buckling behaviour.

In Ref. [32] a modelling and solution framework is developed for instability problems such as wrinkling. Thereby, the nonlinear Föppl-von Kármán thin plate models is extended for the finite membrane strain regime for various hyperelastic materials. The developed framework combines the asymptotic numerical method and discretization by a spectral method. Based on the proposed approach, post-buckling response is investigated with respect to the effects of different incompressible and compressible hyperelastic constitutive models. It is shown that for compressible materials, Poisson's ratio plays a critical role in the onset of wrinkling and disappearance of it.

A study on stretch-induced wrinkling of hyperelastic thin sheets based on nonlinear FEM is presented in Ref. [75]. A plane stress analysis is used to determine the stress distribution patterns in the hyperelastic sheet (without wrinkling). Thereby, the development of compressive stresses in the transverse direction which is necessary

for wrinkling, depends on the aspect ratio and applied tensile load. An eigenvalue analysis is performed to obtain potential buckling modes, which are used in the post-buckling analysis. It is shown that the shell thickness is critical for wrinkling and post-buckling behaviour, in addition to the aspect ratio and the tensile strains. In general, the wrinkle wavelength decreases with increasing strain, whereas the amplitude first increases prior to the critical load and afterwards decreases, eventually flattening out at a moderately large tensile strain.

Anisotropic hyperelastic material

Stretch-induced wrinkles in thin elastic tapes with isotropic material are widely studied within the literature. The wrinkles are in general predicted perpendicular to the stretching direction. However, in anisotropic materials, the wrinkling direction changes according to the material direction. This topic has only recently been studied according to the literature search. In Ref. [62], orthotrophy-related wrinkles and their morphological evolution is studied. A mathematical model is developed by introducing an orthotropic, elastic constitutive law into the extended Föppl-von Kármán plate theory. The developed model is used in the framework of the asymptotic numerical method coupled with the spectral discretization. The authors report that the degree of orthotropy and shear modulus significantly affects the critical buckling strain and the appearance and disappearance of wrinkling. Furthermore, the orientation of wrinkles strongly depends on the angle between the orthotropy and the stretching direction. Based on this work, Ref. [101] reports that stiffer fibres lead to later onset of wrinkling, lower amplitude and earlier disappearance of wrinkles. The authors present a phase diagram on stability boundaries, which can guide wrinkle-free design for membrane structures.

In Ref. [21], a large deformation theory of gradient-elastic membranes has been developed and applied to predict the wrinkling in thin hyperelastic sheets using the FEM. The developed formulation is used to predict wrinkling not only in isotropic mate-

rials, but also anisotropic materials such as pantographic lattices as well as fabric reinforced materials modelled as gradient-enhanced composite laminae.

In Ref. [88], a two-dimensional model of thin anisotropic incompressible sheets with wavy fibre reinforcement is presented. Several equilibrium problems involving rectangular sheets reinforced with sinusoidal fibres are solved using the method of dynamic relaxation. Thereby, a parameter study involving fibre amplitude, wavelength and orientation results in different wrinkling patters in both the longitudinal and lateral direction. The study suggest that even small distortions in fibres are significant, which shows the importance of including the undulation of fibres due to manufacturing process, defects or woven design.

Chapter 3

Nonlinear multi-scale simulations of delamination in textile laminates

A modelling strategy for simulating delamination in textile laminates within the framework of Finite Element Method is presented. An efficient shell element based modelling approach is employed to resolve the textile microstructure at the region of interest which is embedded into a conventional laminate model. Thereby, the model retains high predictive capabilities while being numerically efficient. Double cantilever beam and three point end notch flexure simulations of a six layer 2/2 Twill Weave laminate are conducted. The multi-scale shell element based models are compared to the conventional shell model and analytical predictions. Additionally, locally varying critical energy release rates, damage evolution in the adjacent interfaces and the effects of different ply stacking patterns on the delamination process are investigated.

3.1 Introduction

Composite laminates are widely used in many applications due to their exceptional mechanical properties. Recent developments in the experimental characterization

and computational analysis of composite materials lead to improved performance of complex structures with respect to their load carrying capacity.

In order to further exploit the use of composite laminates, it is necessary to develop and improve modelling approaches and computational methods which are capable of predicting their nonlinear mechanical behaviour under various load cases. In particular this applies to textile laminates which exhibit complex hierarchical structures and their response is determined by the interaction of constituents at various length scales. All laminates without any reinforcement in the thickness direction are prone to interlaminar fracture or delamination which leads to significant degradation of stiffness and strength of the laminated structure. Such type of failure in laminated structures is particular challenging as it is in general difficult to visually identify.

While delamination in unidirectional (UD) composite laminates has been studied thoroughly in the recent decades which led to standardised tests for measuring interlaminar fracture toughness under different modes [28, 29], there is less literature to find on delamination in textile laminates.

Experimental work on delamination in textile laminates, e.g. [4, 47, 52, 55, 58, 77], shows that the measured interlaminar fracture toughness depends on the weaving pattern of plies, their stacking configuration at the delamination plane and orientation. Thereby, the delamination process is commonly studied by examining the delaminated area and surfaces at the debonded plies while performing standardised tests for measuring interlaminar fracture toughness in UD laminates. Compared to UD ply laminates, the textile laminates made from similar constituents exhibit in general higher interlaminar fracture toughness [47]. In some specimens the authors in Refs. [4, 6] have observed damage in several interfaces, delamination migration [52], and even broken fibres from fibre bridging [12] when conducting the double cantilever beam (DCB) and three point end notch flexure (ENF) tests on textile laminates. Observations from experiments indicate that the delamination in textile laminates is a complex process, which is difficult to measure and study since there are numerous mechanisms at work.

In terms of numerical predictions of the nonlinear behaviour, the recent research focus is on interface modelling, e.g. [14, 90, 91], delamination in UD laminates, e.g. [41, 82], and impact simulations, e.g. [83, 84]. Finite Element Method (FEM) simulations of damage and failure in laminates require considerable computational power, in particular when material and interface nonlinearities are to be taken into account with high resolution. Additional complexity is added, when attempting to resolve the fabric topology of plies. Conventional modelling strategies make use of continuum finite elements for the plies and zero-thickness interfaces which are applied between them, cf. [41]. The paper [98] presents a multiscale finite element analysis of mode I delamination growth in a DCB specimen. The meso–scale structure of a 5HS weave fabric is embedded at the initial crack tip into a macro–scale homogeneous model. The unit cell at the meso–scale is created using continuum elements for the yarns and CZ contact elements that can model delamination paths within the matrix and between the matrix and the yarns. The outcome of the paper is the identification of two major toughening mechanisms during delamination: the inter-yarn locking ahead of the delamination front causing stress redistribution and formation of intra-ply delamination. Thereby, the inter-yarn locking is identified as the main source of toughening in mode I delamination of fabric composites.

However, continuum element modelling has its limitations when it comes to modelling of textile topologies on a larger scale, where the number of degrees of freedom (DOF) quickly rises above a manageable number with respect to the computational cost. Therefore, the present work proposes a multi-scale shell element based modelling approach for simulating delamination of adjacent plies in a textile laminate component with special emphasis on numerical efficiency while retaining high predictive capabilities. The approach is applied to model a six layer laminate of 2/2 Twill Weave plies and is compared with a conventional laminate model. The simulations are conducted using the commercial FEM solver `Abaqus/Standard 2017` *(Dassault Systèmes Simulia Corp., Providence, RI, USA).*

3.2 Multi-scale FEM modelling

Textile composite laminates exhibit a highly hierarchical structure where different modes of failure can occur at various length scales. In general, failure mechanisms in laminates can be characterized as inter- and intra-laminar, respectively. The latter includes mechanisms within individual plies such as fibre rupture, matrix cracking and plasticity while the inter-laminar one describes the debonding of adjacent plies. Commonly referred as delamination, it is the predominant failure mode in any laminate without reinforcements through the thickness. In order to account for these mechanisms an appropriately resolved model is needed.

In this work, a composite laminate is studied at the following length scales. At the smallest scale the bundles of fibres impregnated with matrix are represented by a homogeneous material referred to as tows (yarns). Consequently, this length scale is denoted as the *tow-scale*. Non-linearities at the tow-scale are modelled using appropriate constitutive laws. A level higher, the topology of interwoven tows embedded in a matrix, i.e. a textile ply or lamina, is resolved at the so called *ply-scale*. The largest scale is denoted as the *component-scale* and at this scale the textile laminate at the ply-scale as well as the entire component is represented.

A multi-scale shell element based modelling strategy for textile laminates is adopted, which resolves the textile topology in a detailed way in the region of interest. Figure 3.1 illustrates a multi-scale textile laminate with initial delamination in the middle interface from the left side. A domain with a detailed representation of the textile laminate at the ply-scale is embedded into conventional shell layers at the component-scale. At the latter, a textile composite laminate is represented by a stack of plies with homogenised orthotropic linear elastic material properties. Such an approach serves as the basis for a numerically efficient model, where the nonlinearities are captured within the tow and ply-scale domain while the embedding at the component-scale provides the global response with low computational effort. However, such an approach does require prior knowledge about the failure in the component as well as

about the limitations imposed by the embedding, e.g. perturbation effects, to be utilized successfully.

At the ply-scale, the textile microstructure is resolved with the shell element based approach developed in [35] for single textile plies and extended to laminates in [36, 85]. Thereby, the two main constituents in a fabric layer, i.e. the tows and the unreinforced matrix pockets, are modelled by shell elements only, cf. Fig. 3.2. Geometrical idealisations are assumed such as perfectly periodic weaving pattern, piecewise linear tow undulation and rectangular tow cross-section that is uniform along the tow undulation path. The tows are resin impregnated bundles of UD fibres and modelled with shell elements. Their reference planes are defined at the tow mid-surfaces and the tow's undulation path follows the assigned weaving pattern, e.g. Twill Weave or eight harness satin (8HS). The unreinforced matrix, i.e. the matrix pockets, are also modelled by shell elements. For modelling reasons, outside tow surfaces are covered with zero thickness matrix layers, too. The shell reference surfaces are placed at the top and bottom surfaces of the ply. To fill the matrix pockets according to

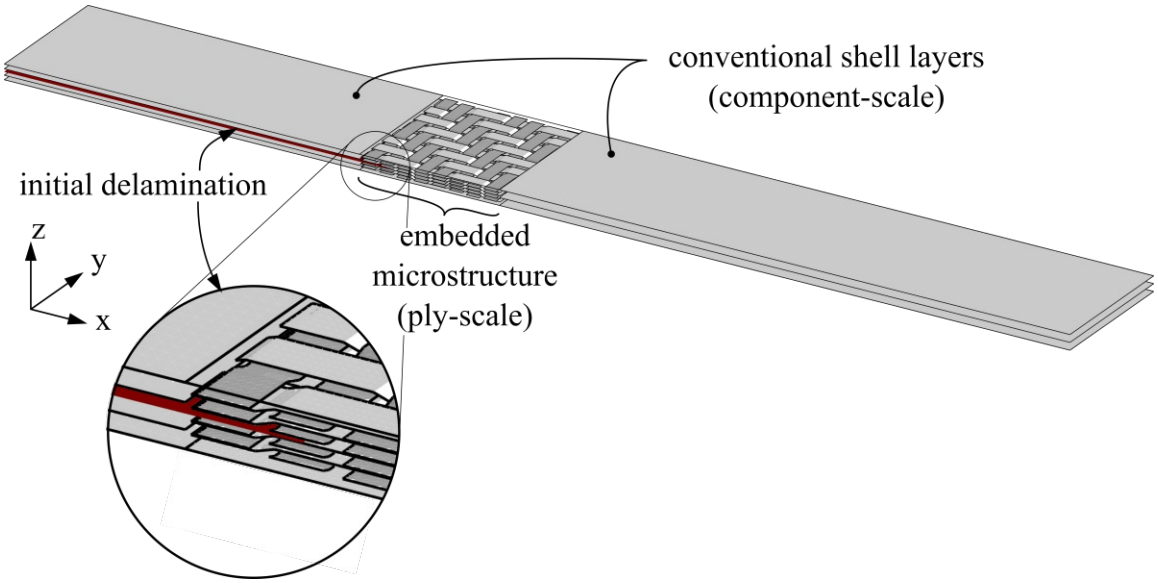

Figure 3.1: Multi-scale shell element based laminate model with conventional shell layers embedding the textile structure at the initial delamination front. The shell layer above the resolved microstructure has been removed to illustrate the embedded woven topology.

the local geometry, a variable shell thickness is applied. The interfaces between the individual overlaying tows and between the tows and matrix are modelled by cohesive elements [14, 23] and tie constraints, respectively. Textile plies can be stacked on top of each other with or without some horizontal shift, resulting in different stacking patterns, cf. Fig. 3.3 for in-phase, mid-phase shift and out-of-phase stacking of a four textile ply laminate. Between the textile plies, zero-thickness cohesive elements are tied to the matrix layers from each adjacent ply, utilizing a surface-to-surface tie constraints.

The ply-scale domain and the shell layers from the component-scale domain are coupled by tie constraints. Figure 3.4 illustrates the coupling techniques used in the present work. At the boundary between the two domains throughout the width of the laminate, the so called edge surface based tie constraint is used, cf. [23]. The definition is based on node to surface formulation, where the slave nodes are projected onto the master surface and their motion is coupled to the motion of the corresponding projected point on the master surface. Through the thickness of a laminate, the ply-scale domain and the shell layers from the component-scale domain are coupled by surface to surface tie constraints, cf. [23]. The surface to surface approach enforces the coupling in an average way over a finite region rather than in a discrete

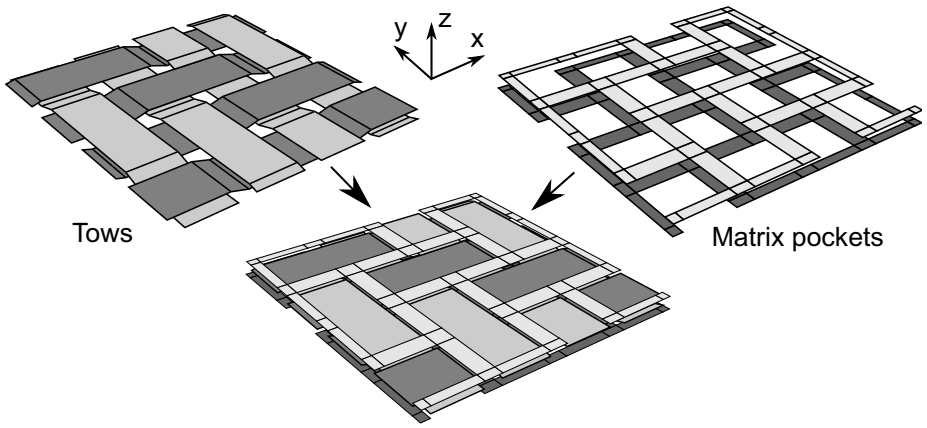

Figure 3.2: Shell element based 2/2 Twill Weave ply assembled (bottom) and disassembled into tow reference planes (left) and matrix reference planes (right) [36].

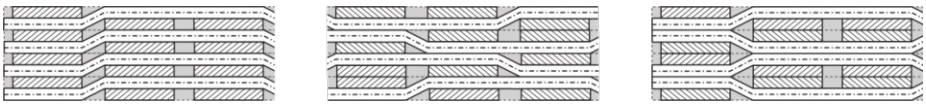

Figure 3.3: Schematic of different stacking patterns. In-phase (left), half-phase shift (middle) and out-of-phase stacking (right) in a four 2/2 Twill Weave ply laminate.

way. Consequently, this approach is advantageous for coupling non-conformal meshes as it minimizes the numerical noise due to averaged kinematic relations between the tied nodes [23].

Between the ply-scale domains, different interface regions are defined by the topologies of adjacent plies. Depending on the weaving pattern, stacking pattern and the orientation of plies, interface properties can be assigned locally for different types of interfaces. In Fig. 3.5 an interface between two in-phase stacked 2/2 Twill Weave plies is illustrated with regions of the interface which locally connect either tows, matrix or combinations of both from adjacent plies. Thereby, tow-tow, tow-matrix, and matrix-matrix interfaces are identified based on the adjacent topology of plies. In case of the 2/2 Twill Weave plies with in-phase stacking, tow-tow interfaces are always between either 0°/90° or 90°/0° oriented tows.

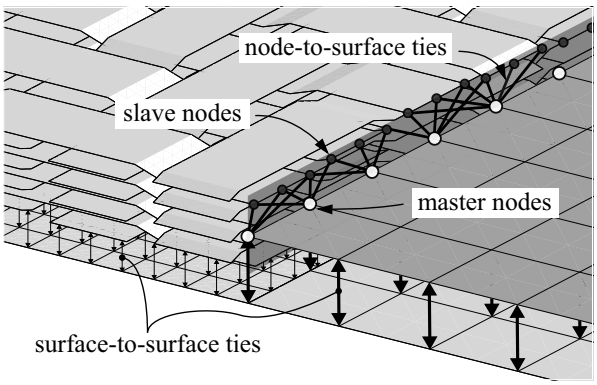

Figure 3.4: Schematic of the coupling between the textile structure and the conventional shell layers. The matrix, cohesive interfaces and some shell layers have been removed in order to illustrate the different coupling techniques.

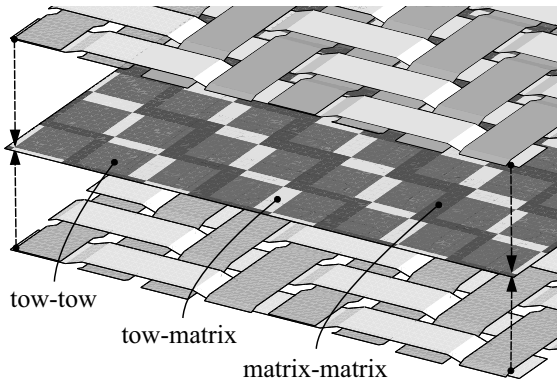

Figure 3.5: Expanded schematic view of different regions in the interface between two in-phase stacked 2/2 Twill Weave plies. Matrix pockets are hidden.

3.3 Application - delamination test set-ups

Simulations of the test set-up for determination of interlaminar fracture toughness energy for mode I, i.e. the double cantilever beam (DCB) [28], and for mode II, i.e the three point end notched flexure (ENF) [29], are performed. Thereby, the multi-scale models of the laminate, cf. Fig. 3.1, are employed. The laminate consists of six layers of 2/2 Twill Weave plies. The dimensions of the complete laminate component are 150 mm in length, 19.68 mm in width and 2.53 mm in thickness. The initial delamination length is 38.68 mm and 53.68 mm for DCB and ENF test simulation, respectively.

Cohesive interfaces between plies and individual tows feature a bi-linear traction separation law with a quadratic nominal stress criterion for damage initiation and an energy based damage evolution. To account for the mode-mix the Benzeggagh–Kenane fracture criterion [9] with a BK parameter of 2 is used.

At first, three different modelling strategies are compared. The conventional shell model (CSM) consists of two sublaminates which are connected by cohesive elements. Each sublaminate is represented by a single composite shell at its mid-plane and is discretized with four-node linear thin shell elements with full integration. The sublaminates are assigned with homogenised material properties for carbon/epoxy

plies, see Tab. 3.1, and thickness of three plies. The homogenised properties are obtained using a numerical homogenisation approach for textile composites based on shell element discretization [35]. Between the sublaminate's mid-planes sits cohesive interface with parameters from Tab. 3.2. The initial stiffness is chosen to approximate quasi-rigid connection between adjacent plies or tows. The nominal strengths for pure mode II and III are taken from a corresponding material data sheet [85]. The nominal strength for mode I is assumed. The critical energy release rates are estimates based on the values published in [40].

Given the proposed modelling in Section 3.2, the multi-scale laminate model, denoted as MSM, embeds a detailed representation of a textile laminate around the initial delamination front. The embedded domain consists of four 2/2 Twill Weave plies which are based on the shell modelling approach from [35]. Within the textile plies at the tow-scale the tow (yarn) width is 1.81 mm, the tow thickness is 0.2018 mm and the spacing between tows is 0.65 mm in both planar directions. The resolved plies at the ply-scale are 19.68 mm in width and length with thickness of 0.4216 mm. The plies are stacked in-phase, cf. Fig. 3.3. At the ply-scale domain, the tows and unreinforced matrix are assigned with properties from Tab. 3.3, while the interfaces between plies are treated as homogeneous and assigned with uniform parameters, cf. Tab. 3.2. The composite shells at the component-scale domain that embed the microstructure are assigned with material properties found in Tab. 3.1.

Motivated by the experimental observations from [4], where authors report that crack propagation along the warp yarns is associated with less resistance than propagation along the weft yarns in a 5HS weave laminate, the MSM model is enhanced with heterogeneous cohesive interfaces and denoted as MSMI model. Thereby, the different regions in the interface, cf. Fig. 3.5, are assigned with modified material parameters.

Table 3.1: Material properties assigned to the homogenised carbon/epoxy plies.

E_1	E_2	ν_{12}	G_{12}
56.589 GPa	56.589 GPa	0.045	4.186 GPa

Table 3.2: Bi-linear traction-separation parameters describing the initial stiffness and the damage initiation and propagation of cohesive interfaces.

	Mode I	Mode II	Mode III
initial stiffness	10^5 N/mm^3	10^5 N/mm^3	10^5 N/mm^3
interlaminar strength	60 MPa	79.289 MPa	79.289 MPa
crit. energy release rate	0.9 N/mm	2.0 N/mm	2.0 N/mm

Table 3.3: Elastic material parameters of the constituent's in carbon/epoxy plies. The subscript 1 and 2 denote the fibre and transverse directions of tows, respectively.

tow	E_1	E_2	ν_{12}	G_{12}
properties	142.177 GPa	13.820 GPa	0.23	6.252 GPa
matrix	E_M	ν_M		
properties	3.25 GPa	0.37		

In the case of tow–tow interfaces, the strength values and the critical energy release rates for all modes are increased by 30% from the values in Tab. 3.2. For the matrix–matrix and tow–matrix regions these interface properties are decreased by 24.2%. This way, the interface properties weighted by the area are the same as in the models with uniform properties. In both multi-scale models the initial delamination reaches one and a half tow width, i.e. 3.68 mm, into the ply-scale domain in order to reduce the perturbation effects from the embedding of the microstructure.

The influence of the stacking pattern is studied by utilizing the MSM model where the plies in the embedded microstructure are stacked in-phase, out-of-phase and mid-phase shift, cf. Fig. 3.3. Other mechanical and geometrical properties, such as e.g. the position of the initial delamination front, remain exactly the same as defined for the MSM model.

An additional insight in the local mechanisms involved during delamination can be obtained when damage modelling is included also for tows in the textile ply layers. In the following case tows are equipped with an anisotropic damage model for

fibre-reinforced material developed by [59], which is readily available in Abaqus. This constitutive model considers four different failure modes - fibre tension, fibre compression, matrix tension, and matrix compression - for composite materials which show no significant plastic deformation before failure. Damage onset is predicted using Hashin's initiation criteria [43, 44] and the evolution of damage is based on fracture energy dissipation, where the increase in damage is governed by linear softening with respect to equivalent displacements. In fact, the evolution law is a generalization of the approach used in cohesive zone modelling [15]. The model in this work that incorporates the constitutive law with tow damage is denoted as MSMID. Table 3.4 lists the nominal strengths and critical energy release rates for all failures modes under Hashin's theory. The values are taken from [85].

Nodal displacement boundary conditions are assigned in both the DCB and the ENF set-ups. Tip displacement, δ_{I}, of 16 mm is applied for the DCB simulations on both arms and central displacement, δ_{II}, of 18 mm for the ENF setup. At the delaminated area, contact constraints are utilized between the adjacent plies using the general contact algorithm in Abaqus/Standard, which is based on the penalty stiffness method. Frictionless contact is defined at both the ply and the component-scale domain. Moreover, as the delamination progresses in the middle interface, contact can be established between plies from either domain. A line search algorithm [23] is used with increased maximum allowed number of iterations (20) and cutbacks (8) within each increment. Viscous regularization with a damping coefficient of $\xi = 10^{-6}\,s$ is

Table 3.4: Nominal strengths and critical energy release rates for the tow's damage initiation and evolution law. The subscripts denote the failure modes where 1 and 2 corresponds to tow's fibre and matrix damage, respectively, under tension (+) and compression (-). S_{12} denote the damage initiation strength under shear loading.

nominal	X_{1+}	X_{1-}	X_{2+}	X_{2-}	S_{12}
strengths	2116.320 MPa	1610.270 MPa	86.138 MPa	333.380 MPa	159.022 MPa
crit. energy	$\mathcal{G}_{\mathrm{Ic}}^{1+}$	$\mathcal{G}_{\mathrm{Ic}}^{1-}$	$\mathcal{G}_{\mathrm{Ic}}^{2+}$	$\mathcal{G}_{\mathrm{Ic}}^{2-}$	
release rates	123.290 N/mm	107.500 N/mm	0.275 N/mm	1.043 N/mm	

prescribed for the cohesive elements. The loading rate for the DCB and ENF simulation is $16\,mm/s$ and $18\,mm/s$, respectively.

In terms of the problem size the MSMI model contains 245000 elements with approximately one million degrees of freedom. All simulations are performed on a standard workstation.

3.4 Results and discussion

3.4.1 ENF simulations

Figure 3.6 shows the load-displacement curves of the ENF simulations where the CSM, MSM and MSMI models are compared. Additionally to the numerical predictions, an analytical solution is given by the Corrected Beam Theory (CBT) [97] for the material properties that describe the homogenised behaviour, cf. Tab. 3.1 and 3.2. The enlarged area in Fig. 3.6 shows the reduction of the reaction force during delamination. While the overall response of the CSM agrees well with the analytical prediction, the MSM show lower peak reaction forces and both multi-scale models exhibit a distinct quasi-stepwise delamination progression.

The delamination progress in the middle interface is shown on Fig. 3.7 (left) for the same models. The central displacement is plotted against the average delamination length in the x direction, where the quasi-stepwise delamination length growth for the multi-scale models is illustrated. The shaded rectangles in the background illustrate the weft pattern, i.e. tows which are oriented transversely to the delamination length growth. This helps to visualise the position of the average delamination front at any given point. Annotation points are added to the response of the MSM model. They are correlated to images in Fig. 3.7 (right), which show the damage initiation criterion, i.e. the quadratic nominal stress criterion, of the cohesive interface in the middle of the laminate. Interface regions where the damage initiation criterion is equal to one and the damage evolution criterion is less than one, is referred as

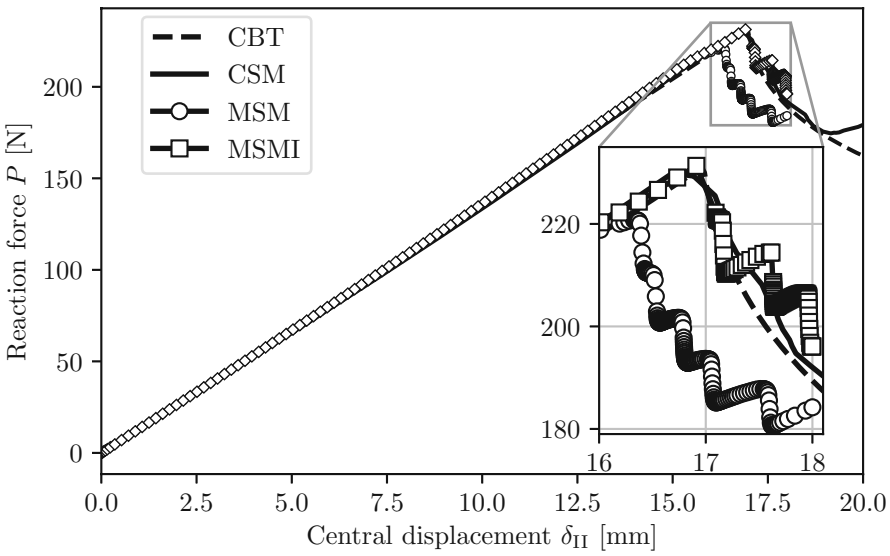

Figure 3.6: Predicted load displacement curves of the ENF setup by the corrected beam theory (CBT), the conventional shell model (CSM), the multi-scale model (MSM) and the multi-scale model with alternating interface properties (MSMI). The enlarged view shows reduction of the reaction force during delamination.

the process zone. Completely damaged elements, i.e. where the damage evolution criterion is equal to one in all of the element's integration points, are removed to illustrate the delamination front.

Figure 3.7 (right) shows the process zone spanning across approximately one and a half tow width and is retarded at regions of the interface which show matrix pockets at either ply. These regions have lower local stiffness compared to the regions reinforced with tows at both plies. Correspondingly, the delamination initiation front forms a distinct shape. From point (a) to (b) the average delamination length increases only marginally compared to the jump between (b) and (c). The sequence in Fig. 3.7 (right) indicates clearly that the shape and the propagation of the process zone is governed by the fabric topology and consequently the alternating local ply stiffness in the vicinity of the delaminating interface.

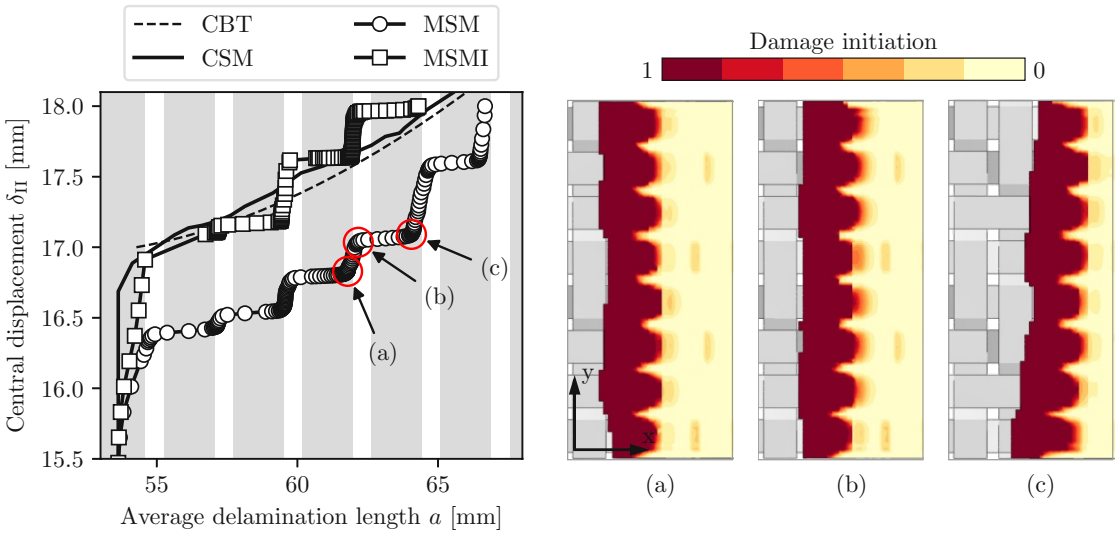

Figure 3.7: Delamination progression for the ENF simulations in terms of the central displacement vs. the average delamination length (left). The damage initiation criterion in the interface (right) is captured at the corresponding annotation points of the response for the MSM model (left). Completely damaged elements are removed to illustrate the delamination front and the process zone, see text for explanation. From the underlying ply only tows are shown.

Note that the delamination front also has a slight angle in Fig. 3.7, right (c). As the delamination front propagates along the interface this angle is alternating due to the twill weave pattern in the plies.

Figure 3.8 show the damage initiation criterion (left) and the damage evolution criterion (right) for all cohesive interfaces between the plies in the MSM model. The images are taken when the delamination front in the middle interface reaches point (*c*) in Fig. 3.7. Damage initiates in a localized pattern in both the top and the bottom cohesive interfaces. However, the damage evolution is limited and the damaged regions do not connect and no delamination is predicted.

Figure 3.9 compares the energy release rates for all models obtained by the modified compliance calibration method (CCM) [25, 54]. The CCM method is chosen because the evaluation of the energy release is based on the compliance of the whole laminate, whereas the CBT relies on the ply and interface material constants. The dashed line

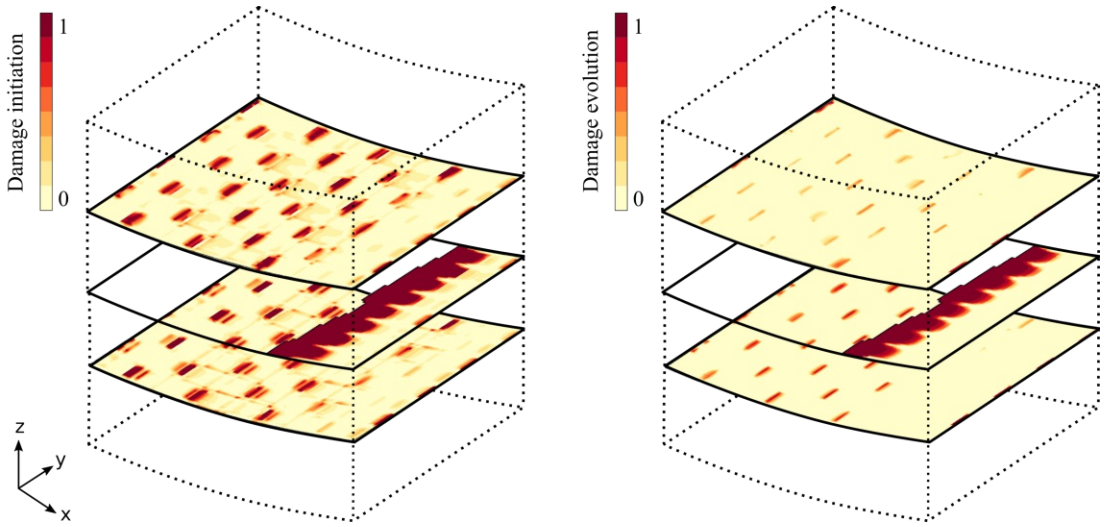

Figure 3.8: Expanded view on damage initiation criterion (left) and damage evolution criterion (right) in the cohesive interfaces of the MSM model for the ENF simulation at load point (c), cf. Fig.3.7.

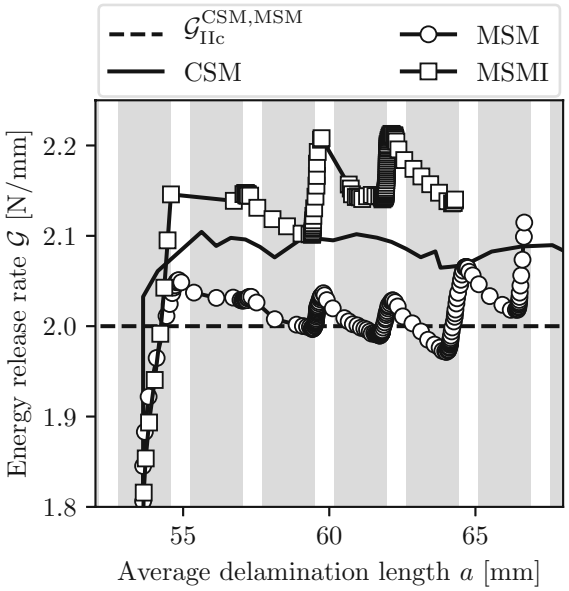

Figure 3.9: Energy release rate evaluated by the CCM method from the ENF simulations and the critical energy release rate (dashed line).

represents the critical energy release rate, $\mathcal{G}_{\mathrm{IIc}}$, used in uniform cohesive interfaces in the CSM and MSM model. The evaluated energy release rate from the MSMI model is approx. 5% larger compared to the MSM model. Note that the initial

delamination front in the multi-scale models is placed one and a half tow width into the embedded microstructure. Consequently, the initial front is placed in the middle of a tow that is oriented along the delamination front at both adjacent plies. There a locally increased fracture toughness is modelled for the MSMI model. In agreement to the delamination length growth jumps, cf. Fig. 3.7, an unstable delamination length growth in terms of $\frac{\partial \mathscr{G}}{\partial a} < 0$ is observed locally for both multi-scale models.

Figure 3.10 shows the delamination growth during the ENF simulation of the MSM models with in-phase, half-phase shift, and out-of-phase stacking pattern, cf. Fig. 3.3. The delamination length growth in the case of out-of-phase stacking has approximately twice the size but half as many quasi-steps compared to in-phase stacking. The predicted delamination growth in the laminate with half-phase shift is roughly between the other two stacking patterns. For a 2/2 Twill Weave in-phase stacked laminate, the tows from neighbouring plies are always transverse to each other. Consequently the tow-tow interface regions form a chequerboard-like pattern, cf. Fig. 3.5. However, in an out-phase stacked laminate, the tow-tow interface regions form a pattern that resembles the 2/2 Twill Weave. Therefore the process zone propagates in a more stable way and with bigger steps in terms of the delamination length growth compared to the other configurations. In terms of the evaluated energy release rate, cf. Fig. 3.11, the out-of-phase stacking exhibits higher energy release rate compared to the rest of stacking sequences.

Figure 3.12 illustrates tow matrix tensile damage initiation criterion in the MSMID which is most present in the ply layer above the middle delaminating interface. The damage initiation is most present on the weft yarns where tows are tied to the cohesive interface, which is depicted with the enlarged view in Fig. 3.12. Note that the overlaying warp yarn have been removed in the enlarged view. Except for the elements at the initial delamination front, the tensile damage variable in the tow matrix does not evolve to complete failure, i.e. the dissipated energy of the elements do not reach the critical values. Note that the shell-based modelling approach used for the microstructure is arguably over-constrained due to the ties between the matrix,

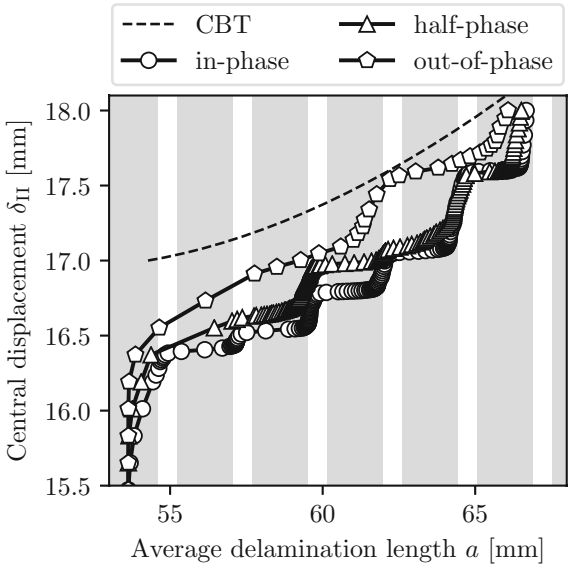

Figure 3.10: Delamination length growth in MSM models with in-phase, half-phase shift, and out-of-phase stacking patterns for the ENF simulations.

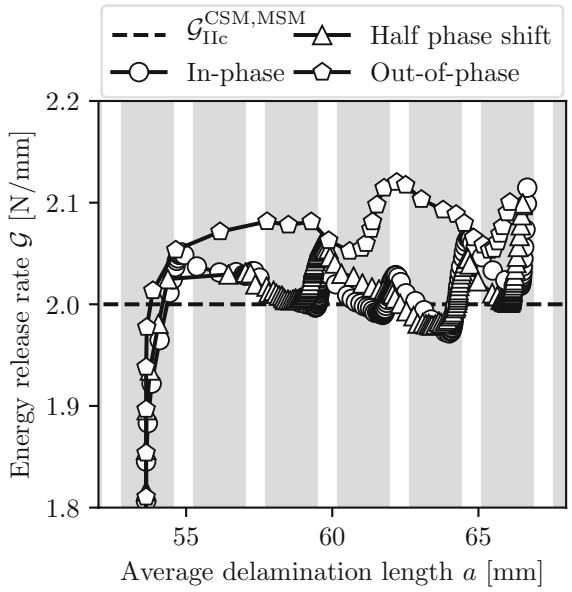

Figure 3.11: Energy release rate evaluated by the CCM method for the MSM models with in-phase, half-phase shift, and out-of-phase stacking.

tows and intra-ply cohesive interfaces. Thereby, tow damage with intra-ply delamination is limited as cohesive interface elements are placed only between overlying

tows. The remaining part of tows is tied directly to the matrix pockets which have varying thickness to fill the gaps. The rest of the Hashin's damage modes, i.e. tow matrix under compression and fibres under both tensile and compressive stresses, are not present in any layer. Compared to the damage dissipation energy in the cohesive interfaces, the dissipated energy in the tows is negligible, cf. Fig. 3.13 (left). On the right, the dissipated energy due to viscous regularization in the model is shown to be insignificant compared to the recoverable strain energy and damage dissipation energy, which is the case also for other variants of the multi-scale models both in the ENF and DCB test simulations.

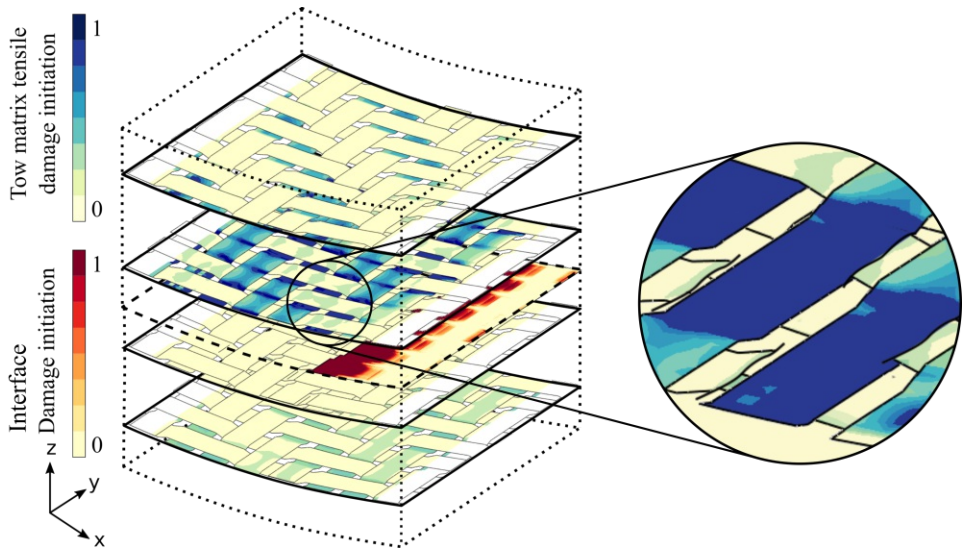

Figure 3.12: Exploded view on the tow matrix tensile damage initiation criterion in the textile layers of the embedded microstructure in the MSMID model. In the middle, damage initiation criterion in the cohesive interface is depicting the current position of the delamination front.

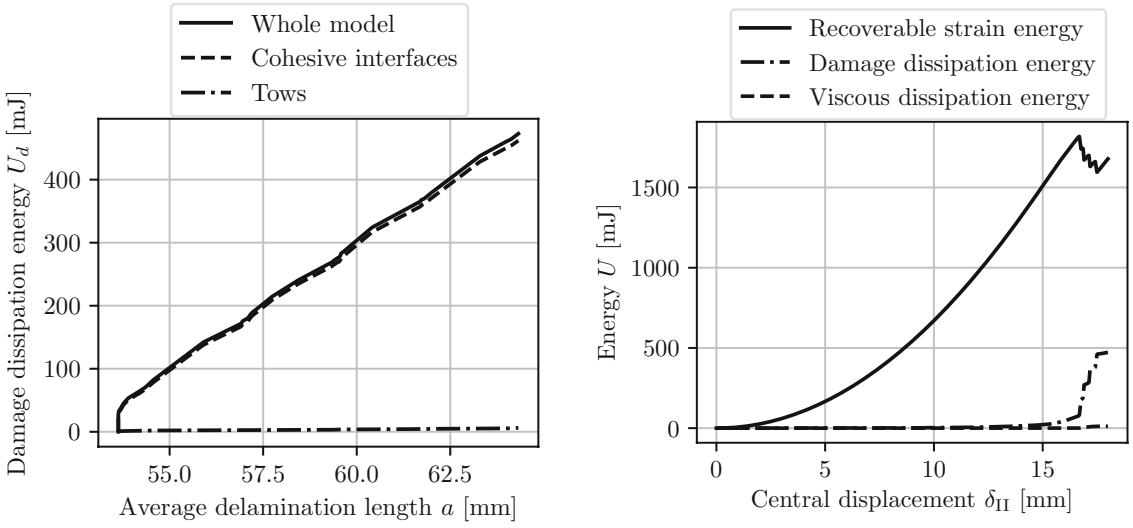

Figure 3.13: Energy allocation in the MSM model during ENF simulation. On the left, damage dissipation energy is compared between the cohesive interfaces and tows, the latter being insignificant to the dissipated energy in the whole model. On the right, the viscous dissipation energy due to viscous regularization is negligible compared to recoverable strain and damage dissipation energy.

3.4.2 DCB simulations

Figure 3.14 shows the load displacement curves of the CSM, MSM and MSMI models with in-phase stacking pattern for the DCB simulations. In all models, the reaction force towards the critical value does not follow the CBT prediction due to the creation of the process zone in the cohesive interfaces. The CSM model agrees well with the CBT prediction. The multi-scale models predict higher peak reaction force and the quasi-stepwise reduction of the reaction force is more pronounced compared to the ENF simulations. The MSMI model predicts smaller but twice as many steps in the reduction of the reaction force compared to the MSM model.

Figure 3.15 shows the delamination progress for the DCB simulations. In the same way as for the ENF simulations in Fig. 3.7, the annotation points on the left graph are presented with contour plots of the process zone in the MSM model on the right. The process zone width is approximately half the tow width and is significantly smaller compared to mode II delamination due to the lower critical energy release rate for mode I. The local ply topology has only small influence on the shape of the process zone, however, the delamination progression is strongly influenced by it. From point (a) to (b) the delamination length growth is very subtle. In this phase the process zone is quasi stationary over the region of tows (from both plies) and he damage initiation front borders with the region of matrix pockets. Looking at the damage initiation front, cf. Fig. 3.15 (right), the jump in the delamination length from point (b) to (c) takes place from one trailing edge of tows to the next one.

In contrast to the MSM, the delamination length growth rate in the MSMI does reduce at matrix pockets. This is seen as the additional steps in the response in Fig. 3.15 (left). A possible explanation for this is the fact that the MSMI model has weaker interfaces at the matrix pockets and stronger interfaces at tows from both plies. This can be observed on Fig. 3.16 where the position of weft yarns are shown and consequently the space in between where the matrix pockets are positioned. Thereby, the additional steps in the delamination growth is a consequence of varying interface

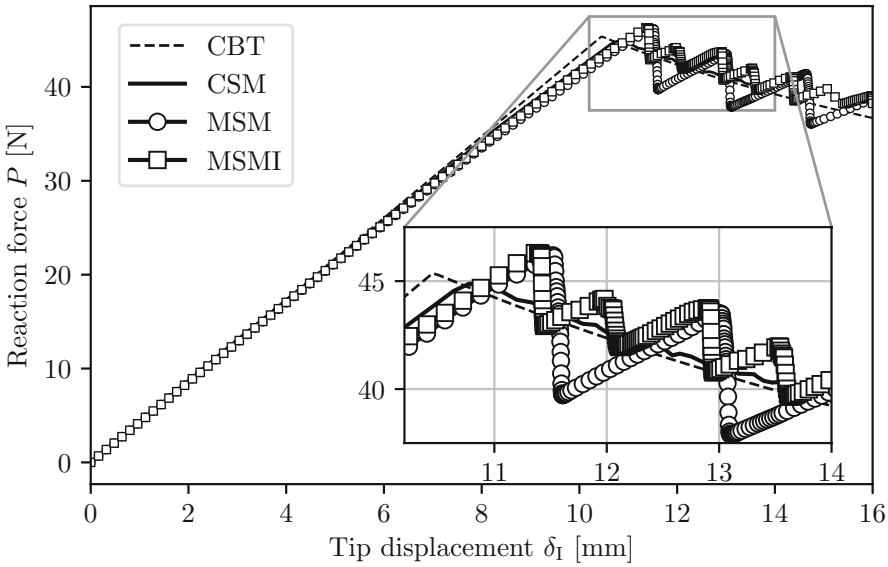

Figure 3.14: Load displacement curves of the DCB simulations. The enlarged view shows the reduction of the reaction force during delamination. CBT denotes the solution given by the corrected beam theory, CSM the conventional shell model, MSM the multi-scale model and MSMI the multi-scale model with alternating interface properties and in-phase stacking.

properties and relatively small process zone in the interface. However, this result only showcases the abilities of the model, since the interface properties of stronger and weaker regions are set without any experimental references and are assumed only from an observation made in other studies, cf. [4].

The energy release rate for the CSM, MSM and MSMI model in the DCB simulation is shown of Fig. 3.16. The energy release rates are obtain using the modified compliance calibration method. Both multi-scale models overshoots the energy release rate by some percent in average and the stepwise response corresponds to the reduction in the reaction force, cf. Fig. 3.14.

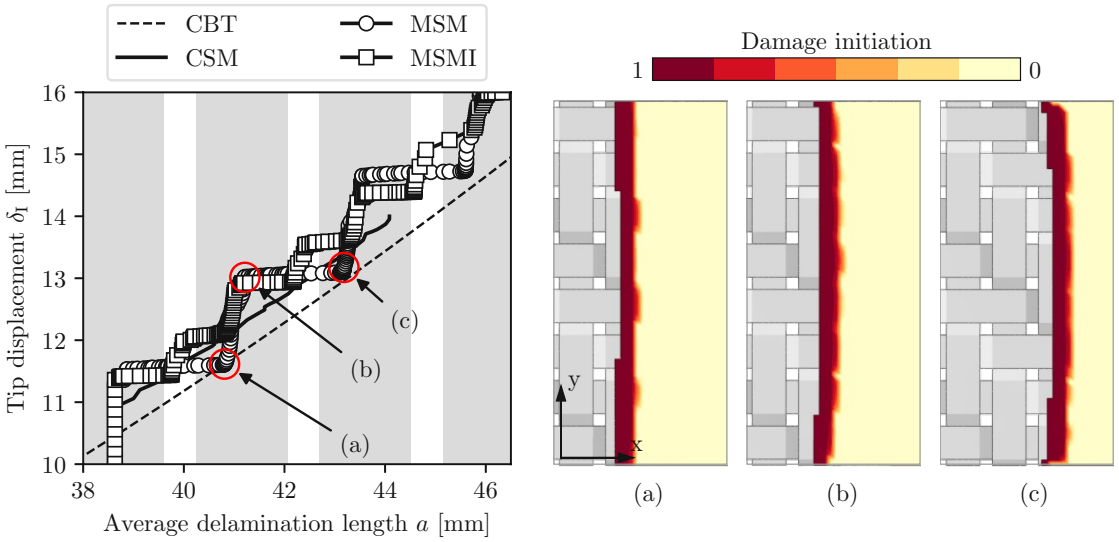

Figure 3.15: Delamination progression for the DCB simulations in terms of the tip displacement vs. the average delamination length (left). The shaded rectangles illustrate the weft yarns. The damage initiation criterion in the interface (right) is captured at the corresponding annotation points of the response for the MSM model.

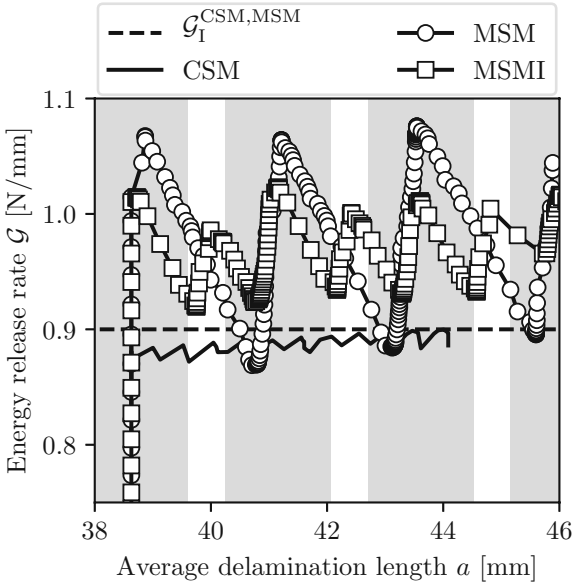

Figure 3.16: Energy release rate evaluated by the CCM method from the DCB simulations and compared to the critical energy release rate (dashed line).

3.5 Summary

A modelling strategy for simulation of delamination in textile laminates by means of the FEM is presented. A multi-scale embedding approach is utilized to include the highly resolved structure of the fabric plies at the region of interest while the rest of the laminate is modelled by a conventional laminate approach. Except for the cohesive interfaces, the model is completely represented by shell elements at all length scales. Such an approach proves to be an efficient modelling strategy that exhibits high predictive capabilities while the computational effort is kept low enough to utilize the simulations using standard desktop hardware. The present modelling approach is used to study delamination in a 2/2 Twill Weave carbon reinforced epoxy laminate. To demonstrate the application, several multi-scale models are simulated for standardised interlaminar fracture test set-ups. Detailed insight into the governing mechanisms at work are obtained by studying the evolution of the process zone at the delaminating interface. A clear relation between the local stiffness of the textile plies and the delamination progress is observed as expected from experimental work in the literature. Furthermore the size of the process zone compared to the width of the yarns in the resolved textile plies has a strong influence on the delamination growth. This causes the delamination growth in the textile microstructure to progress in a quasi step-wise manner, which is clearly seen in the load displacement curves and the evaluated energy release rates. In the multi-scale models, interfaces parallel to the middle one are also prone to delamination. There, damage initiation is recorded in isolated regions, however, the modelling approach limits the separation of tows in the ply domain (intra-ply delamination) which prevents delamination migration to another interface.

In addition, the multi-scale models are equipped with heterogeneous interfaces, where the different interface properties are assigned according to the local topology. Despite the difficulties of obtaining relevant properties from interface characterization, the influence of varying interface is shown to be greater with smaller process zone. In the

DCB simulations, where the process zone is much smaller than the tow width, the weaker interfaces at the matrix pockets retard the delamination growth compared to the model with homogenous interface. The main challenge is the determination of the interface properties, for which extensive experimental studies are required and by our knowledge have not been conducted in the literature. Therefore, this results serve only as a demonstration of the modelling approach and are of qualitative character.

Given that several experimental studies observe some damage in the tows, the multi-scale model is extended with a damage constitutive law for fibre reinforced polymers at the tow-scale. In the ENF simulation, tow's matrix tensile damage initiation is recorded in the ply above the delamination plane. Such damage mode would physically result in separation of bundle of fibres within the tows, which could lead to delamination migration as reported in some studies. However, the tows in the model are constrained by ties to the matrix, which limits the damage of intra-ply cohesive elements and consequently of tows. A possible way to overcome this limitation is to place cohesive elements between each of the constituents in the textile plies. This would significantly increase the problem domain, but ultimately determination of the interface properties for each local region is still the biggest challenge.

Chapter 4

Material calibration framework for fibre reinforced elastomers based on a micromechanical approach

Material models employed to predict the effective behaviour of fibre reinforced elastomers (FRE) often rely on non-trivial material parameter fitting to experimental or numerical results. A calibration method is presented in this work which minimises the need for fitting of material parameters. The method is applied for the Holzapfel–Gasser–Ogden (HGO) anisotropic hyperelastic strain energy density function in order to prescribe the effective behaviour of composites with linear elastic unidirectional fibres with random fibre arrangement and nearly incompressible hyperelastic matrix material for various fibre volume fractions. The calibration of material parameters is based on the initial behaviour of FRE, which is approximated as linear elastic. Thereby, analytical micromechanical methods can be applied to obtain the initial behaviour and calibrate the material parameters. The response of the calibrated HGO model is compared to multi-fibre unit cell models for a scope of fibre volume fractions for different load cases. The presented method is limited to composites where unidirectional fibres can be considered as rigid compared to the matrix.

4.1 Introduction

Fibre reinforced composite materials are useful for many applications due to their exceptional mechanical properties, such as high stiffness-to-weight and strength-to-weight ratios. Recent developments in the experimental characterisation and computational analysis of composite materials can lead to improved performance of complex structures with respect to their load carrying capacity.

In recent years, fibre reinforcements are being used in combination with elastomers and other rubber-like materials in order to exploit the mechanics of highly flexible structures which can serve as alternatives for conventional mechanisms. With this interest, fibre reinforced elastomers (FRE) are commonly used in pneumatic soft composite actuators [37, 74, 79, 87, 95], as lightweight mechanisms in deployable structures [24, 69, 81], and as shape memory composites [39, 67].

FRE composites exhibit complex geometry and interactions between its constituents at the microscale. In order to bridge the length scales and to predict the effective macroscopic behaviour several analytical and numerical methods and tools have been developed. Ponte Castañeda [16] has developed an analytical second-order homogenisation framework for non-linear isotropic composites. Thereby, the effective mechanical properties are obtained from bounds and estimates of a linear comparison composite. Based on this framework analytical homogenisation schemes have been further developed for particle reinforced composites [64–66] and unidirectional fibre reinforced composites with periodic arrangement [13] and random distributions [1]. An expression for the effective strain energy density function of a transversely isotropic hyperelastic fibre-reinforced composite in terms of the properties of the two incompressible neo-Hookean phases and their spatial distribution has been developed by deBottom [27]. The analytical homogenisation schemes are generally successful, however, their estimates are typically limited to certain microstructural geometries, deformation modes and constituent's material properties and contrast.

Numerical homogenisation schemes are based on modelling discrete microgeometries. Among them, periodic microfield models such as the unit cell approaches are a common choice for numerical homogenisation of FRE materials with periodic or random fibre distribution. Moralada et al [72] compare predictions of unit cell models with analytical homogenisation schemes such as the second-order homogenisation estimates [66] and approximations by a sequentially laminated composite model [26] for in-plane finite deformations of random FREs. The authors show that both analytical models are able to capture unit cell's response when Neo-Hookean matrix and circular fibre cross section are used. However, in case of Gent matrices the analytical models overestimate the lock-up stretch, which exposes the difficulties associated with modelling local phenomena by means of homogenisation strategies.

Periodic microfield models where the reinforcement phase is quasi randomly distributed are associated with size effects. Elaborate studies on the representative volume elements (RVE) of fibre reinforced soft composites by Khiseava and Ostoja [56, 57] report that a sufficient RVE size depends on the quantity of interest, e.g. the maximum stretch ratio, the deformation mode or the mismatch of properties of constituents. Thereby, windowing approaches, kinematic, static and mixed uniform boundary conditions and ensemble averages have been used to study the influence of size and material properties. However, the maximum contrast between the initial shear modulus of the constituents is ten, which is too low for FRE composites where fibres can be treated as rigid compared to the matrix. More recently, Lopez Jimenez [63] studies the effects of unit cell size and fibre volume fraction on the direction dependency of the initial shear modulus in the linear regime and effective strain energy density in the non-linear regime for fibre reinforced silicone composites with initial shear modulus contrast of 10^4 between the fibres and matrix. Thereby, a correlation between the variation of the initial shear modulus and the variation of the normalized strain energy in the non-linear regime is reported which enables to predict the direction dependency at large stretches from the initial properties.

Homogenisation frameworks are useful tools for predicting the effective response to given load cases of FRE composites. However, structural simulations require constitutive models which can be employed in the framework of the Finite Element Method (FEM) for structures under arbitrary load cases. Constitutive models for FREs in finite elasticity are in general derived as anisotropic hyperelastic strain energy density functions. The strain-based Fung's form [20, 33] and the invariant based Holzapfel–Gasser–Ogden (HGO) form [38, 49] have been initially developed for arterial walls with collagen fibres. Both are purely phenomenological models and have been successfully employed also for other applications.

Conventionally, fitting material parameters of models relies on experimental data from several load cases such as uniaxial, biaxial and planar tests. The fitting procedure often relies on mathematical methods such as the Gauss-Newton algorithm and the standard non-linear Levenberg-Marquardt algorithm [50].

In applications where the material properties are tailored to specific loading configurations there is a need to avoid the fitting procedure based on experiments, especially if novel material combinations in a composite are of interest. Therefore, this work presents an approach where the fitting of material parameters is minimized by calibration based on micromechanical methods and mechanics of linear elastic materials. Thereby, initial values are obtained which give good approximation for arbitrary load cases. For the non-linear behaviour under larger strains, only a few parameters are required which can be deduced from the constituents properties. Such an approach shows potential for engineering applications where FRE material is employed in a structure and the influence of constituents properties is of interest.

All FEM simulations are conducted using the commercial FEM package `Abaqus 2019` *(Dassault Systèmes Simulia Corp., Providence, RI, USA)*.

4.2 Homogenisation by the unit cell approach

Periodic microfield approaches are an established method to numerically analyse the macroscale and microscale behaviour of composite materials by studying periodic microstructures [11]. A common strategy for analysing strain and stress fields is based on subdividing the micro geometry into periodically repeating unit cells. Unit cells must be used with appropriate boundary conditions in order to generate valid deformed states, i.e. the unit cell must exhibit periodicity of geometry, material, loads and displacements in every state [10]. In manufacturing of fibre reinforced composites the position of fibres is generally difficult to control and often in applications the fibres are assumed to be arranged randomly. The effective behaviour of such composites can be approximated by periodic multi-fibre unit cells that employ quasi-random fibre positions. The estimates provided by multi-fibre unit cells can strongly depend on the size, number of fibres, material mismatch and loading conditions, especially in the non-linear regime. However, this work does not aim to study such effects which have been investigated before but instead to study the effective properties of the unit cells that are utilized and compare the response to a calibrated material model.

4.2.1 Material properties

The unit cells consist of two phases, where linear elastic glass fibres are reinforcing a hyperelastic rubber-like matrix material defined with the Ogden type of the strain energy density function [78], defined as

$$U = \sum_{i=1}^{N} \frac{2\mu_i}{\alpha_i^2} \left(\bar{\lambda}_1^{\alpha_i} + \bar{\lambda}_2^{\alpha_i} + \bar{\lambda}_3^{\alpha_i} - 3 \right) + \sum_{i=1}^{N} \frac{1}{D_i} \left(J^{\mathrm{el}} - 1 \right)^{2i} \quad , \tag{4.1}$$

where $\bar{\lambda}_i = J^{\frac{1}{3}} \lambda_i$ are the deviatoric principal stretches , λ_i are the principal stretches, J^{el} is the non-thermal volume change and μ_i, α_i and D_i are material parameters. The Ogden strain energy density function is defined with a set, N, of material parameters.

Table 4.1 lists the material parameters for both constituents. The interface between constituents is assumed to be perfect.

4.2.2 Geometry and fibre arrangement

The geometry of unit cells are generated with `Digimat-FE 2017` *(e-Xstream engineering SA., Hautcharage, Luxembourg)*. The multi-fibre unit cells are three dimensional models with dimensions $l_x = l_y$ and l_z, which form an idealized composite reinforced with fibres with circular cross section of radius r which are perfectly aligned in the z direction. The fibre distribution is generated using a random seed technique, where the placement of each fibre results from the convergence of an iterative process. The fibre position is accepted if all the constraints are verified, i.e. the minimum distance from other fibres and minimum relative cut-off volume of fibres intersecting the unit cell faces. This is repeated until the criterion for the assigned fibre volume fraction is met or the constraints cannot be fulfilled in maximum number of iterations. Any fibre intersecting one of the unit cell faces has its complement placed on the opposite edge, generating a periodic topology on all sides. The constraints of the fibre placing are necessary to avoid very narrow bands of matrix material between the fibres, which are difficult to discretise and high strain localisation can occur there already at relatively small loads. The minimum cut-off relative volume of fibres placed at the

Table 4.1: Material parameters of constituents in the FRE composite. Initial shear and bulk modulus for the matrix material are denoted as $\mu_0^{(\mathrm{m})}$ and $K_0^{(\mathrm{m})}$, respectively.

Constituent	Material parameters	Initial properties [MPa]
Matrix – Ogden type	$N = 1$	$\mu_0^{(m)} = 3.49 \cdot 10^{-1}$
	$\mu_1^{(\mathrm{m})} = 3.490 \cdot 10^{-1}$ MPa	$K_0^{(m)} = 2.01 \cdot 10^2$
	$\alpha_1^{(\mathrm{m})} = 2.163$	
	$D_1^{(\mathrm{m})} = 9.961 \cdot 10^{-3}$ 1/MPa	
Fibres - linear elastic	$E^{(\mathrm{f})} = 8 \cdot 10^4$ MPa	
	$\nu^{(\mathrm{f})} = 0.2$	

faces is also enforced to improve mesh discretisation. Figure 4.1 illustrates the fibre arrangement of the multi-fibre unit cells with a size of $2r/l_x = 0.15$ for 10.6, 19.4, 30.0, and 40.6% fibre volume fraction. This corresponds to 6, 11, 17, and 23 fibres within each unit cell, respectively.

4.2.3 Model properties and periodic boundary conditions

The unit cells are discretized using eight node continuum elements with linear interpolation functions and hybrid or mixed formulation. Hybrid elements are used to cope with the nearly incompressible material, where the deviatoric and volumetric stress response is treated separately. Thereby, the hydrostatic stress is formulated as a Lagrange multiplier imposing the condition of hydrostatic stress to be zero.

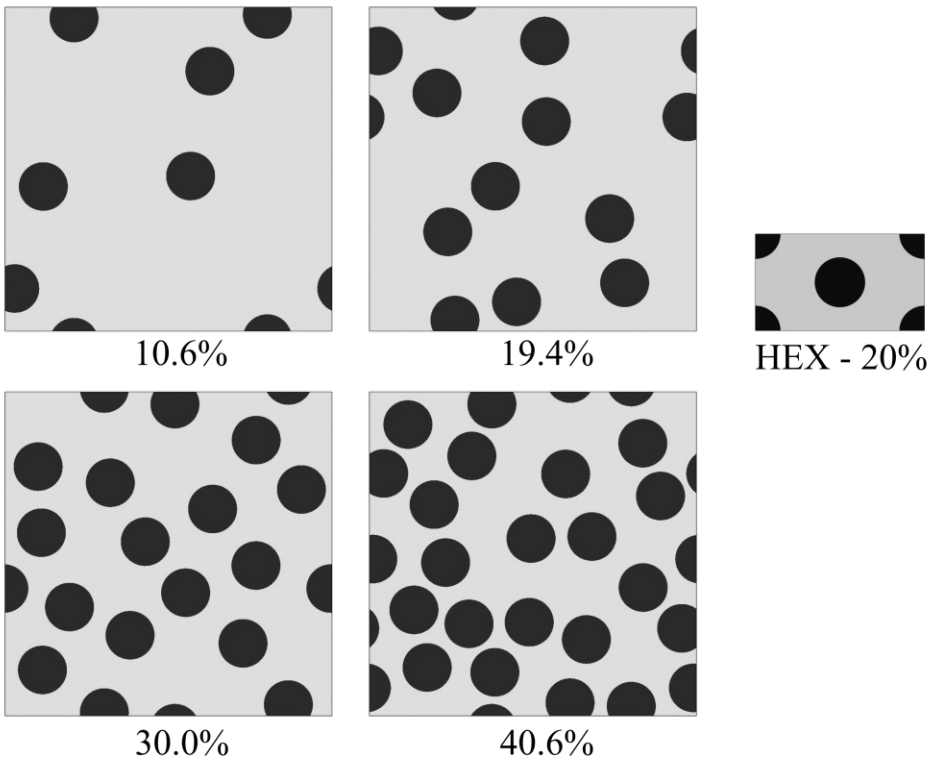

Figure 4.1: Cross section of periodic multi-fibre unit cells with 10.6, 19.4, 30.0, and 40.6% fibre volume fraction (approximately) and the unit cell with hexagonal fibre arrangement (HEX) with 20% fibre volume fraction.

The multi-fibre unit cells are equipped with spatial periodic boundary conditions which ensure valid deformation states under arbitrary load cases. The use of periodic boundary conditions requires conforming meshes on all opposite pairs of surfaces, i.e. the nodes must be positioned at identical face coordinates, $\tilde{s}_j$. Thereby, the displacement of node pairs can be directly constrained. The periodic boundary conditions are summarized as a set of linear constraints

$$u^i_{\Gamma^+_x}(\tilde{s}_j) - u^i_{\Gamma^-_x}(\tilde{s}_j) - u^i_{\text{SEB}} = 0 \tag{4.2}$$

$$u^i_{\Gamma^+_y}(\tilde{s}_j) - u^i_{\Gamma^-_y}(\tilde{s}_j) - u^i_{\text{NWB}} = 0 \tag{4.3}$$

$$u^i_{\Gamma^+_z}(\tilde{s}_j) - u^i_{\Gamma^-_z}(\tilde{s}_j) - u^i_{\text{SWT}} = 0 \quad , \tag{4.4}$$

where i is the degree of freedom, $\Gamma^+_{()}$ and $\Gamma^-_{()}$ denote the opposite faces of the unit cell and $\tilde{s}_j$ are the matching nodes on opposite faces, cf. Fig. 4.2. Displacements of master nodes are denoted as $u^i_{()}$, where SEB, NWB and SWT represent the master nodes at $(l_x, 0, 0)$, $(0, l_y, 0)$ and $(0, 0, l_z)$, respectively, cf. Fig. 4.2. The displacements of the SEB master node at $(0, 0, 0)$ are fixed.

Far field stresses and strains can be applied to unit cell's faces via concentrated nodal forces and displacements at the master nodes, respectively. The effective response

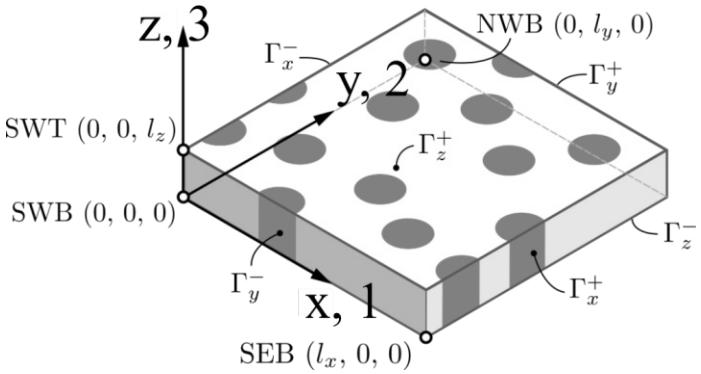

Figure 4.2: Dimensions of the multi fibre unit cell with randomly placed unidirectional fibres. Master nodes are denoted with SWB, SWT, SEB and NWB. Opposite surface pairs are denoted with $\Gamma^+_{()}$ and $\Gamma^-_{()}$.

is obtained by evaluating the master node displacements and forces. This approach was termed "the method of macroscopic degrees of freedom" by Michel et al. [10, 71]. The non-linear homogenisation approach used in this work follows the method of macroscopic degrees of freedom at each increment, where the displacements and forces of the master nodes are extracted. Thereby, the effective strain energy density and the macroscopic deformation gradient are obtained and different stress and strain measures are derived.

4.2.4 Effective behaviour

The response in the fibre direction is dominated by the fibre properties. For fibre materials such as glass the longitudinal stretch is limited by the strength. In this work the focus is on the response transverse to the fibre direction in the non-linear regime where stretches up to $\lambda = 1.5$ are applied. Also treated is the linearised elastic response with respect to the undeformed configuration.

Initial linearised response. The effective behaviour of FRE unit cells in the linear regime can be obtained with the standard linear homogenisation approach, where six independent load cases are applied. Thereby, the effective elasticity or compliance tensor is obtained [10]. A measure for the anisotropy of orthotropic materials is given by the Zener parameters [103]. For the plane transverse to fibre direction the following parameter is used

$$Z_1 = \frac{2\,E_{44}}{E_{11} - E_{12}} \quad , \tag{4.5}$$

which in case of ideal transverse isotropy is equal to unity. If the elasticity tensor is rotated around the fibre axis by an angle, θ, the Zener parameter, Z_1, can be obtained as a periodic function of θ, which is a general property of anisotropic elasticity. Results on Fig. 4.3 shows the Zener anisotropy measure as a function of the in-plane direction for four unit cell realisation with fibre volume fraction ranging from 10.6 to 40.6%. The Zener parameter increases with the fibre volume fraction reaching almost 15%

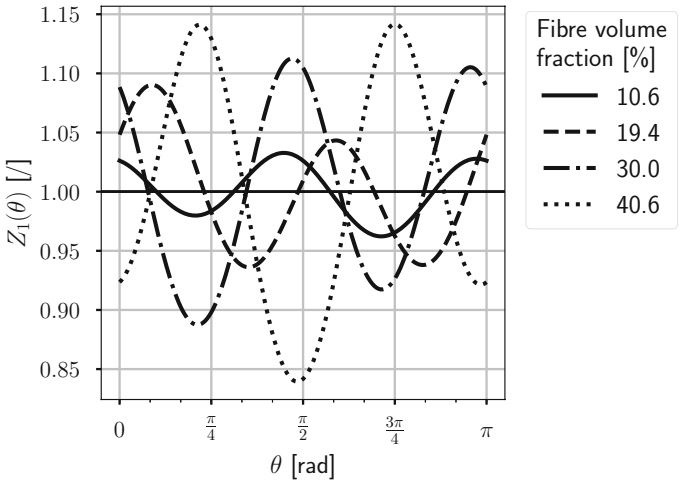

Figure 4.3: Zener anisotropy parameter for the in-plane initial elasticity of four multi fibre unit cells with random unidirection fibre distribution and fibre volume fraction from 10.6 to 40.6%.

deviation for the 40% fibre volume fraction with $\pi/2$ periodicity. Equivalent results were obtained in [63] where the initial shear modulus was obtained by explicitly applying the load in a range of directions. The in-plane anisotropy is an effect of the quasi random fibre placement and unit cell size. The initial response of the particular multi-fibre unit cells does not yield strictly true representative volume elements for a transversely isotropic material. However, for the purpose of this work, their initial effective behaviour can be approximated as such.

Behaviour in the finite strain regime. In-plane direction dependency in the non-linear regime is demonstrated with a specific load case. The stretch, λ, is applied in the direction, θ, as depicted on the Fig. 4.4. All deformations in the fibre direction, i.e. out-of-plane deformations, are fixed. The load case is set as isochoric which directly determines all principal stretches as λ, $1/\lambda$ and 1 for maximum, minimum and middle with corresponding principal directions $\mathbf{n}_{\max} = (\cos\theta, \sin\theta, 0)$, $\mathbf{n}_{\min} = (-\sin\theta, \cos\theta, 0)$ and $\mathbf{n}_{\mathrm{mid}} = (0, 0, 1)$, respectively. By varying the angle from zero to π radians one can compare each response in the principal stretch direction and observe the in-plane direction dependency of the unit cell. Figure 4.5 shows the direction dependent response in the plane perpendicular to the fibre direction for

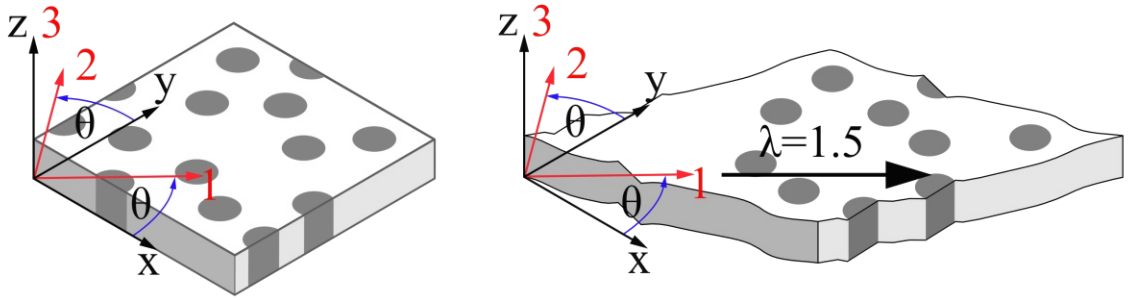

Figure 4.4: Load case for investigating the direction dependency in the plane transverse to the fibre direction.

a multi fibre unit cell with 11 fibres, fibre volume fraction of 19.4%. A stretch of $\lambda = 1.5$ is applied in directions from zero to π radians with a step of $\pi/180$ radians. Thereby, on the left the lowest and the highest value of the strain energy density, $\langle U \rangle$, are shown with respect to the applied stretch, λ. On the right the strain energy is shown with respect to the direction, ϕ, at several values of the applied stretch λ. The coefficient of variation of the strain energy, i.e. the standard deviation of the effective strain energy across all directions normalized by its mean value, increases with the load by 35% from 1.1 to 1.5 stretch. The relative dispersion of the effective response is not only dependent on the direction but also on the magnitude of the applied load.

For comparison Fig. 4.6 shows the periodic response of a unit cell with hexagonal fibre arrangement and 20% fibre volume fraction. Same material is used, cf. Tab. 4.1. Note that hexagonal fibre arrangement in linear-elastic elasticity yields transversely isotropic effective properties. With large strains and hyperelastic matrix, the effective response is strongly dependent on the direction, seen as much larger variation of the effective strain energy. The response is periodic with $\pi/3$ periodicity caused by the initial hexagonal fibre arrangement.

Figure 4.7 show the direction dependency of multi fibre unit cells with 10.6, 19.4, 30.0, and 40.6% fibre volume fraction, cf. Fig. 4.1. The variation of the strain energy

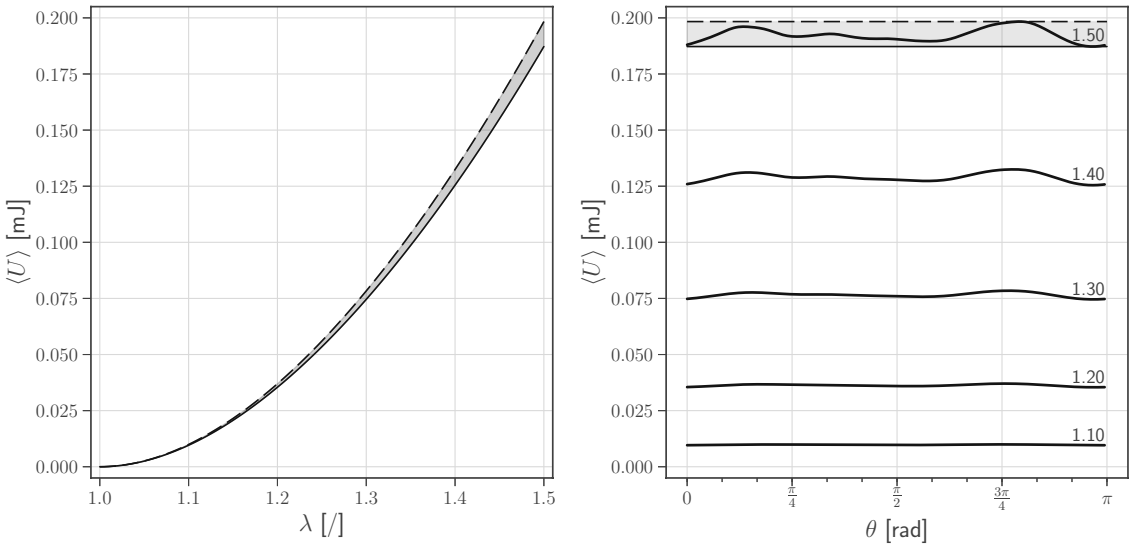

Figure 4.5: Direction dependency of a multi fibre unit cell with 19.4% fibre volume fraction, 11 fibres: (left) the highest and the lowest values of the effective strain energy, $\langle U \rangle$, versus the applied stretch, λ; (right) the effective strain energy at several stretches λ, with respect to the direction θ.

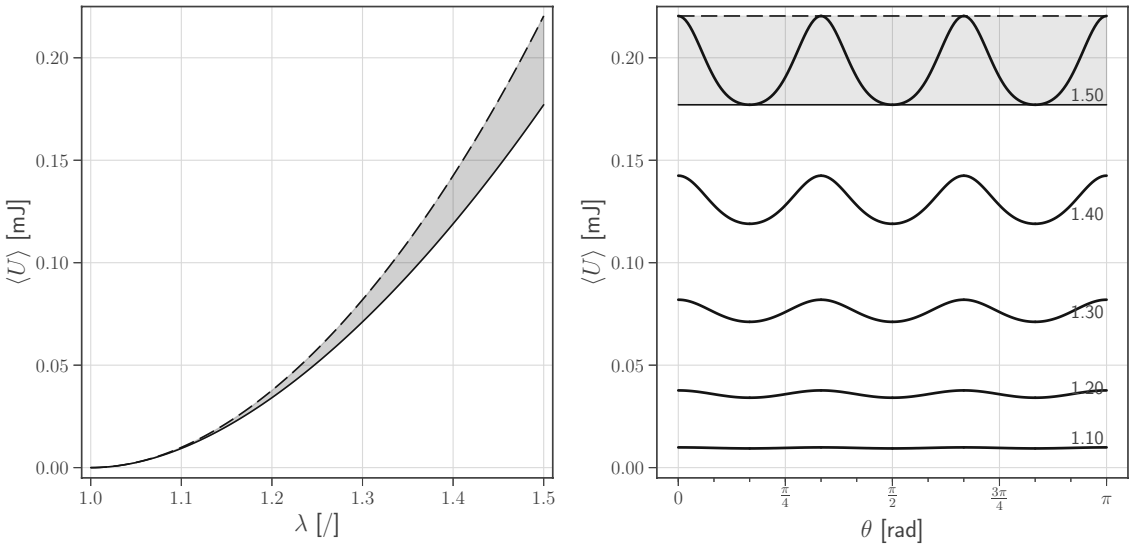

Figure 4.6: Direction dependency of the unit cell with hexagonal fibre arrangement and 19.4% fibre volume fraction: (left) the highest and the lowest values of the effective strain energy, $\langle U \rangle$, versus the applied stretch, λ; (right) the effective strain energy at several stretches λ, with respect to the direction θ.

increases significantly with higher fibre volume fraction. At 40% fibre volume fraction the multi-fibre unit cells exhibit severe element distortion already at moderate stretch values, e.g. at $\lambda = 1.2$ as seen in Fig. 4.7 as discontinuity in the lines. Thereby, larger unit cells, finer discretization, and re-meshing techniques would be necessary to obtain valid results for high stretches.

4.3 Anisotropic hyperelastic material model

The effective response of the multi fibre unit cells is approximated with an anisotropic hyperelasic material model. Readily available in `Abaqus` are the invariant-based Holzapfel-Gasser-Ogden (HGO) model [38, 49] and the strain-based Fung's model [20, 33]. Both models have been initially developed to model biological tissues. A comprehensive comparison between the two models is given in [48], where it is reported that the Fung's model is not convex for all possible sets of material parameters and the model has severe restrictions when strong ellipticity is imposed [96]. In fact, for the composite material considered in this work, cf. Tab. 4.1, suitable material parameters cannot be identified without exhibiting material instabilities. Therefore, only the HGO model is used to demonstrate the approach.

4.3.1 Holzapfel–Gasser–Ogden model

The HGO model has been developed for modelling arterial layers with distributed collagen fibres [49]. The HGO form of the strain energy density function is defined in terms of the invariants of the right Cauchy-Green stretch tensor and the fibre directions based on the continuum theory of fibre-reinforced composites [86]. Due to the nature of collagen fibres the model assumes that the fibres cannot sustain any compressible loads, which is a strong limitation for modelling fibre reinforced elastomers. For this reason we consider only load cases where the fibres are either

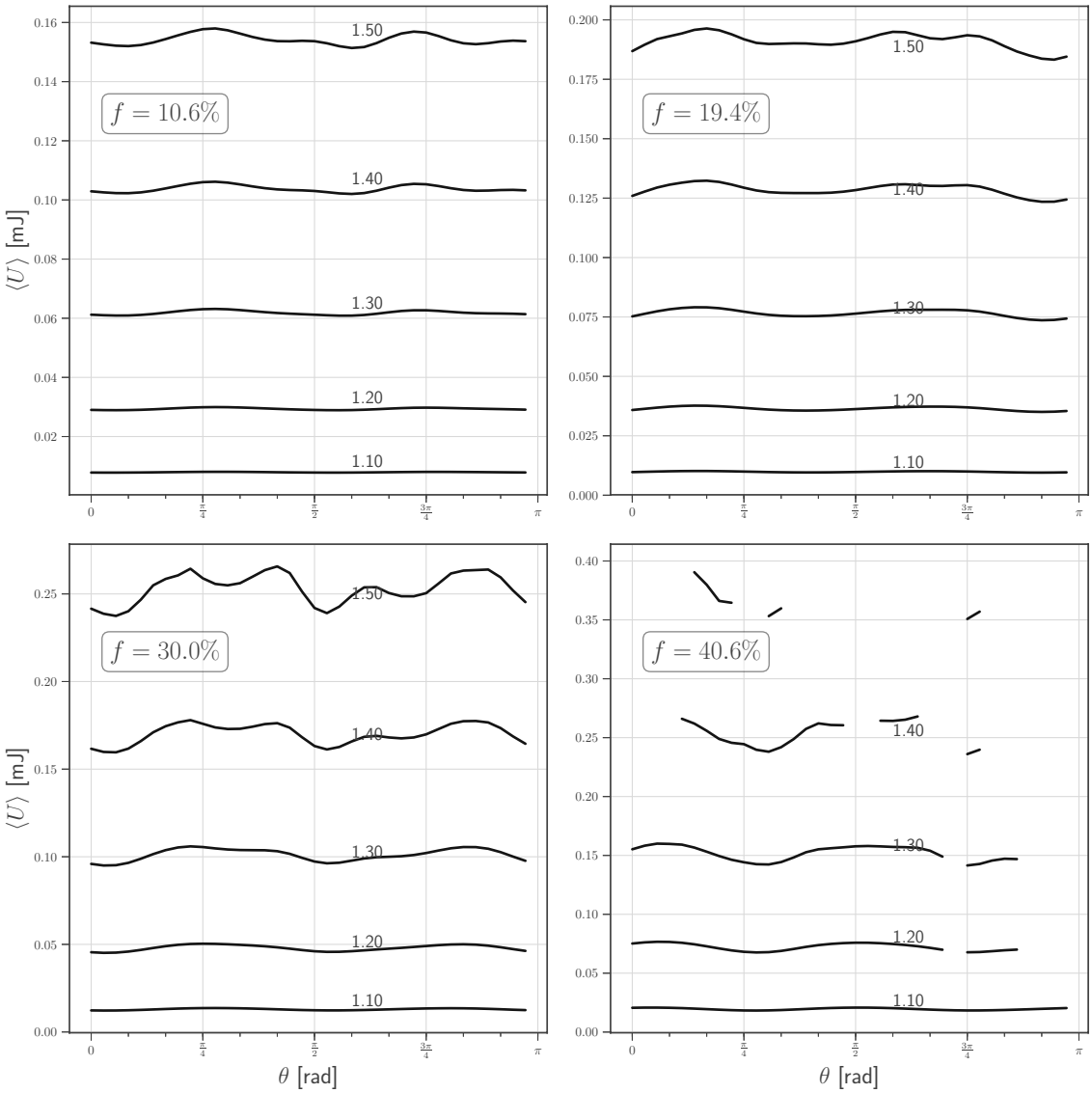

Figure 4.7: Direction dependency of multi fibre unit cells with 10.6, 19.4, 30.0, and 40.6% fibre volume fraction. All unit cells are the same size of $2r/l_x = 0.15$. At 40% fibre volume fraction excessive element distortion is present at higher stretches resulting in failed simulation and discontinued lines.

in tension or are "unloaded". The HGO model is defined as a strain energy density function. For unidirectional fibres the model simplifies to

$$U = C_{10}(\bar{I}_1 - 3) + \frac{1}{D}\left(\frac{(J^{\mathrm{el}})^2 - 1}{2} - \ln J^{el}\right) + \frac{k_1}{2k_2}\left(\exp\left[k_2\langle\overline{\overline{E}}_1\rangle^2\right] - 1\right) \quad , \qquad (4.6)$$

where C_{10}, D, k_1 and k_2 are the material parameters, $\bar{I}_1$ is the first invariant of the deviatoric part of the right Cauchy-Green stretch tensor $\bar{\mathbf{C}} = J^{-\frac{2}{3}}\mathbf{C}$ and J^{el} is the elastic volume ratio. In the exponential function the $\overline{\overline{E}}_1$ is defined as

$$\overline{\overline{E}}_1 = \bar{I}_{4(11)} - 1 \quad , \tag{4.7}$$

where the $\bar{I}_{4(11)}$ is the pseudo-invariant of $\bar{\mathbf{C}}$ and the fibre direction $\mathbf{a}_1$ defined as

$$\bar{I}_{4(11)} = \mathbf{a}_1 \cdot \bar{\mathbf{C}} \cdot \mathbf{a}_1 \quad . \tag{4.8}$$

The Macaulay brackets in Eq. (4.6) denote that only positive values of $\overline{\overline{E}}_1$ contribute to the strain energy density. Thereby, the assumption that fibres only act in tension is enforced. Consequently the HGO model with compression in the fibre direction simplifies to a Neo–Hookean form for the isotropic deviatoric part of the strain energy density function, i.e. $C_{10}(\bar{I}_1 - 3)$. For the general formulation of the HGO strain energy function refer to [22, 48].

Calibration of material parameters. In the present work, it is proposed to start calibration of the material parameters for the HGO model at the initial state or the unloaded configuration of the material. At this state the initial linear elastic behaviour can be obtained by taking the second derivative of the strain energy density function, U, with respect to the right Cauchy-Green stretch tensor, $\mathbf{C}$. Hyperelastic incompressible material models only have energy contributions of distortional deformations. For that reason, the calibration only considers the deviatoric behaviour. At the initial state it is characterized by the initial deviatoric elasticity tensor, which is defined as

$$\bar{\mathbf{D}}_0 = 4\frac{\partial U_{\text{dev}}^2}{\partial \bar{\mathbf{C}} \partial \bar{\mathbf{C}}} \tag{4.9}$$

where $U_{\text{dev}} = U - U_{\text{vol}}$. For the HGO model with unidirectional fibres, the initial deviatoric elasticity tensor reads as [22]

$$\bar{\mathbf{D}}_0 = 4C_{10}\mathscr{J} + 2k_1\, H(\overline{\overline{E}}_1)\, \mathbf{a}_1 \otimes \mathbf{a}_1 \otimes \mathbf{a}_1 \otimes \mathbf{a}_1 \quad , \tag{4.10}$$

where $\mathscr{J}$ is the fourth-order unit tensor and $H(x)$ is the Heaviside unit step function, which ensures the contribution from the fibres only in tension. Similar as in the strain energy density function the isotropic part and the contribution of the fibres are decoupled. The deviatoric part of the elasticity tensor with arbitrary material symmetry can be obtained with projection tensors for spherical and deviatoric decomposition of stress and strain tensors, see the Appendix A. The identity fourth order tensor, $\mathscr{J}$, can be split into symmetrical and asymmetrical parts as $\mathscr{J} = \mathscr{J}^{\mathrm{s}} + \mathscr{J}^{\mathrm{a}}$. The symmetrical part of the identity fourth order tensor can be further decomposed into the spherical and deviatoric projection tensors, $\mathscr{P}_1$ and $\mathscr{P}_2$ respectively, as $\mathscr{J}^{\mathrm{s}} = \mathscr{P}_1 + \mathscr{P}_2$. The projection tensors are defined as

$$\mathscr{P}_1 = \frac{1}{3}\mathbf{I} \otimes \mathbf{I} \quad , \tag{4.11}$$

$$\mathscr{P}_2 = \mathscr{J}^{\mathrm{s}} - \mathscr{P}_1 \quad , \tag{4.12}$$

and are used to decompose the stress and the strain tensors into volumetric and deviatoric parts

$$\begin{aligned} \boldsymbol{\sigma} &= \mathscr{J}^{\mathrm{s}} : \boldsymbol{\sigma} \\ &= (\mathscr{P}_1 + \mathscr{P}_2) : \boldsymbol{\sigma} \\ &= \boldsymbol{\sigma}_{\mathrm{V}} + \boldsymbol{s} \end{aligned} \tag{4.13}$$

and

$$\begin{aligned} \boldsymbol{\varepsilon} &= \mathscr{J}^{\mathrm{s}} : \boldsymbol{\varepsilon} \\ &= (\mathscr{P}_1 + \mathscr{P}_2) : \varepsilon \\ &= \boldsymbol{\varepsilon}_{\mathrm{V}} + \boldsymbol{e} \quad , \end{aligned} \tag{4.14}$$

where $\boldsymbol{\sigma}_{\mathrm{V}}$, $\boldsymbol{\varepsilon}_{\mathrm{V}}$ and $\boldsymbol{s}$, $\boldsymbol{e}$ denote the volumetric and deviatoric stress and strain, respectively. A deviatoric elasticity tensor, $\bar{\mathbf{D}}$, maps the strain, $\boldsymbol{\varepsilon}$, to deviatoric stress, $\boldsymbol{s}$. From Hooke's law, $\boldsymbol{\sigma} = \mathbf{E} : \boldsymbol{\varepsilon}$, it follows

$$\begin{aligned} \boldsymbol{s} &= \mathbf{E} : \boldsymbol{e} \\ &= \mathbf{E} : \mathscr{P}_2 : \boldsymbol{\varepsilon} \\ &= \bar{\mathbf{D}} : \boldsymbol{\varepsilon} \quad , \end{aligned} \tag{4.15}$$

where the deviatoric elasticity tensor is defined in index notation as

$$\bar{D}_{ijmn} = E_{ijkl}\, \mathscr{P}_{2(klmn)} \quad . \tag{4.16}$$

The initial behaviour of FRE composite with unidirectional fibres can be approximated as linear elastic with transversely isotropic symmetry. The transversely isotropic elasticity tensor can be defined with the Hill parameters [94]. For isotropy in the 1-2 plane the elasticity tensor reads in Voigt-Nye notation as

$$\mathbf{E}_{\mathrm{triso}} = \begin{bmatrix} \underline{k}+\underline{m} & \underline{k}-\underline{m} & \underline{l} & 0 & 0 & 0 \\ \underline{k}-\underline{m} & \underline{k}+\underline{m} & \underline{l} & 0 & 0 & 0 \\ \underline{l} & \underline{l} & \underline{n} & 0 & 0 & 0 \\ 0 & 0 & 0 & \underline{m} & 0 & 0 \\ 0 & 0 & 0 & 0 & \underline{p} & 0 \\ 0 & 0 & 0 & 0 & 0 & \underline{p} \end{bmatrix} \quad , \tag{4.17}$$

with the Hill parameters

$$\underline{n} = E_{33} + 4k_{12}\nu_{13}^2 \quad , \tag{4.18}$$

$$\underline{l} = 2k_{12}\nu_{13} \quad , \tag{4.19}$$

$$\underline{k} = \frac{E_{33}}{2(1-\nu_{12})(E_{33}/E_{11}) - 4\nu_{13}^2} = k_{12} \quad , \tag{4.20}$$

$$\underline{m} = G_{12} \quad , \tag{4.21}$$

$$\underline{p} = G_{13} \quad , \tag{4.22}$$

where E_{33} and E_{11} denote the axial and transverse Young's modulus, G_{13} and G_{12} the axial and transverse shear modulus and ν_{13} and ν_{12} the axial and transverse Poisson ratio.

Individual components of the initial deviatoric tensor, $\bar{\mathbf{D}}_0$, Eq. (4.10) can be compared to the corresponding components in the deviatoric part of a transversely isotropic elasticity tensor, $\bar{\mathbf{D}}_{\text{triso}}$. Thereby the material parameters C_{10} and k_1 are calibrated with the effective properties of a transversely isotropic linear elastic composite. Note that this approach is only valid when the composite exhibits a very high contrast between the shear modulus of fibres and the matrix, for example when fibres can be considered as rigid compared to the matrix. In such case, the following assumptions can be made for the effective properties of the initial behaviour. First, the effective axial and transverse shear moduli are approximately equal, $G_{12} \approx G_{13} \rightarrow \underline{m} \approx \underline{p}$. Thereby, the C_{10} parameter can be calibrated via the transverse shear component, i.e. 1212 component, in both deviatoric tensors as

$$\bar{D}_{0(1212)} \equiv \bar{D}_{\text{triso}(1212)} \tag{4.23}$$

$$\bar{D}_{0(1212)} = E_{\text{triso}(12ij)}\mathscr{P}_{2(ij12)} \tag{4.24}$$

$$4C_{10} = 2\underline{m} \tag{4.25}$$

$$C_{10} = \frac{1}{2}G_{12} \tag{4.26}$$

In the same way the k_1 parameter is calibrated via the axial component. In this case via the 3333 component where it follows

$$\bar{D}_{0(3333)} \equiv \bar{D}_{\text{triso}(3333)} \tag{4.27}$$

$$\bar{D}_{0(3333)} = E_{\text{triso}(33ij)} \mathscr{P}_{2(ij33)} \tag{4.28}$$

$$2k_1 + 4C_{10} = \frac{2}{3}(\underline{n} - \underline{l}) \tag{4.29}$$

$$k_1 = \frac{1}{3}(E_{33} + 4k_{12}\nu_{13}(\nu_{13} - 0.5)) - G_{12} \tag{4.30}$$

At this point further simplifications are made. Assuming that the effective axial Young's modulus, E_{33}, is several orders of magnitude higher than the effective shear modulus, G_{12}, and that $E_{33} >> 4\widehat{k}_{12}\nu_{13}(\nu_{13} - 0.5)$ we can set the k_1 simply with the effective Young's modulus as

$$k_1 \approx \frac{1}{3}E_{33} \quad . \tag{4.31}$$

The material parameters D and k_2 are not included in the initial deviatoric elasticity as D relates to the volumetric part of the strain energy and parameter k_2 is eliminated during the derivation of the initial deviatoric elasticity and therefore acts as a parameter which influences the fibre contribution at larger strains. The material parameters C_{10} and k_1 are evaluated at the initial state, therefore the linearised behaviour at the initial state of the anisotropic hyperelastic composite material must be obtained. For this purpose, the initial linearised response of the isotropic hyperelastic matrix material and the linear elastic fibre properties is taken, which gives a combination of linear elastic constituents in a composite. This enables the use of homogenisation schemes such as microfield models and mean field methods to predict the effective material properties.

4.4 Results and discussion

The predictions from the multi-fibre unit cells (MFUC) with material properties in Tab. 4.1 are compared to the single element simulations utilizing the HGO material model with calibrated material parameters for transverse, axial and combined load cases. Fibre volume fractions of 10, 20, 30 and 40% are investigated for each load case. The HGO material is calibrated based on the initial behaviour estimated by the Mori-Tanaka method [73]. The estimates for different fibre volume fraction are listed in Tab. 4.2. The effective properties are obtained for constituent materials in Tab. 4.1, with the initial properties for the matrix and fibres. With the effective estimates, the material parameters of the HGO model are set based on the calibration method Eq. (4.26) and Eq.(4.31) as $C_{10} = \frac{1}{2}G_{12}$, $k_1 = \frac{1}{3}E_{33}$. The parameter D is set to 10^4 1/MPa to approximate nearly incompressible behaviour while the parameter k_2 is set to 1 as no fitting at higher stretches is conducted. At each fibre volume fraction a single realization of the multi-fibre unit cell is considered. In single element simulations an eight node hexahedral continuum element with linear interpolation functions is used. Note that the material parameters of the HGO model have not been fitted to responses of the unit cells and are purely derived with the calibration approach described in the previous section. All load cases are isochoric and displacement controlled. Volume is preserved throughout the simulations, cf. Appendix B. Nonlinear homogenisation is done with built-in scripts in `Medtool` *(Dr. Pahr Ingenieurs e.U., Pfaffstätten, Austria)* which are used to evaluate the effective response by the incremental method of macroscopic degrees of freedom.

Table 4.2: Mori-Tanaka estimates for effective linear elastic moduli.

f [%]	10	20	30	40
E_{33} [MPa]	$8 \cdot 10^3$	$16 \cdot 10^3$	$24 \cdot 10^3$	$32 \cdot 10^3$
G_{12} [MPa]	$4.266 \cdot 10^{-1}$	$5.235 \cdot 10^{-1}$	$6.481 \cdot 10^{-1}$	$8.143 \cdot 10^{-1}$

4.4.1 Transverse load

The transverse load case prescribes deformations in the plane transverse to the fibre direction. All deformations out of this plane are zero. The displacement loading is derived from the isochoric macroscopic deformation gradient

$$\mathbf{F}^{\mathrm{trv}} = \begin{bmatrix} 1 & 0.5 & 0 \\ 0 & 1 & 0 \\ 0 & 0 & 1 \end{bmatrix} \quad , \qquad (4.32)$$

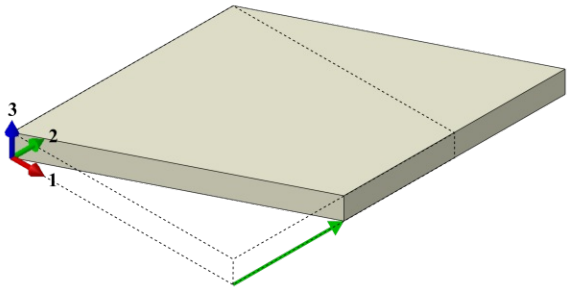

Figure 4.8: Proportional load for the transverse load case.

which describes the final deformation state. Effectively this is simple shear loading, cf. proportional loading on Fig. 4.8. The maximum principal stretch is $\lambda_{\max} = 1.28$. Figure 4.9 shows the normal components and the in-plane shear component of the second Piola-Kirchoff stress deviator, S^{dev}, in relation to the in-plane shear Green strain, E_{12}. The dashed lines depict the predictions from the single element with calibrated HGO model. The solid lines with shaded area between them are the results given by the unit cell models. The range of the unit cell results is obtained by applying the transverse case, Eq. (4.32), in range of directions ϕ from zero to π radians, see Fig. 4.4, with an increment of $\pi/36$. For fibre volume fractions up to 30% the calibrated HGO model is in very good agreement with the unit cell predictions for all stress components. With higher volume fraction the scatter of the unit cell response is higher, a consequence of the non representativeness of the unit cells. At all fibre volume fractions in Fig. 4.9, the calibrated HGO model response is toward the lower values of the unit cell's stress response. At 40% fibre volume fraction, the calibrated HGO model is unable to match the unit cell's response, even at small stretches. Note that in the HGO model only the "isotropic" part is activated,

where a simplified matrix-fibre interaction is contained within the C_{10} parameter, which is calibrated using Mori-Tanaka estimates for the initial behaviour. At higher fibre volume fraction and nearly incompressible matrix material, it is unclear if such configurations exceed the limitations of the Mori-Tanaka method.

In Ref. [19] it is reported that for a composite with spherical inclusions, incompressible matrix, contrast between the shear modulus of inclusions and matrix of 10^2 and fibre volume fraction of 40% the Mori-Tanaka estimates deviate from the generalised self-consistent method for approximately 30%. Alternatively, the HGO material parameters can be calibrated using the initial effective properties given by the numerical linear homogenisation method. In this case, the effective shear modulus for the unit cell with 40% fibre volume fraction is approximately 22% higher than estimate given by the Mori-Tanaka method, cf. Tab 4.3. Figure 4.10 shows the response of the single element test of the HGO model, which has been calibrated with the initial linearised properties of the multi-fibre unit cell for 40% fibre volume fraction. Thereby, the HGO model gives results which are within the bounds of the unit-cell response.

Table 4.3: Initial effective shear modulus, $\widehat{G}_{12}$, across fibre volume fractions, f, predicted by the Mori-Tanaka method (MTM) and linear homogenisation approach with the multi-fibre unit cells (MFUC).

f [%]	$\widehat{G}_{12}^{MTM}$ [MPa]	$\widehat{G}_{12}^{MFUC}$ [MPa]	δ [%]
10	0.427	0.441	+3.4
20	0.524	0.545	+4.1
30	0.648	0.740	+14.2
40	0.814	0.997	+22.4

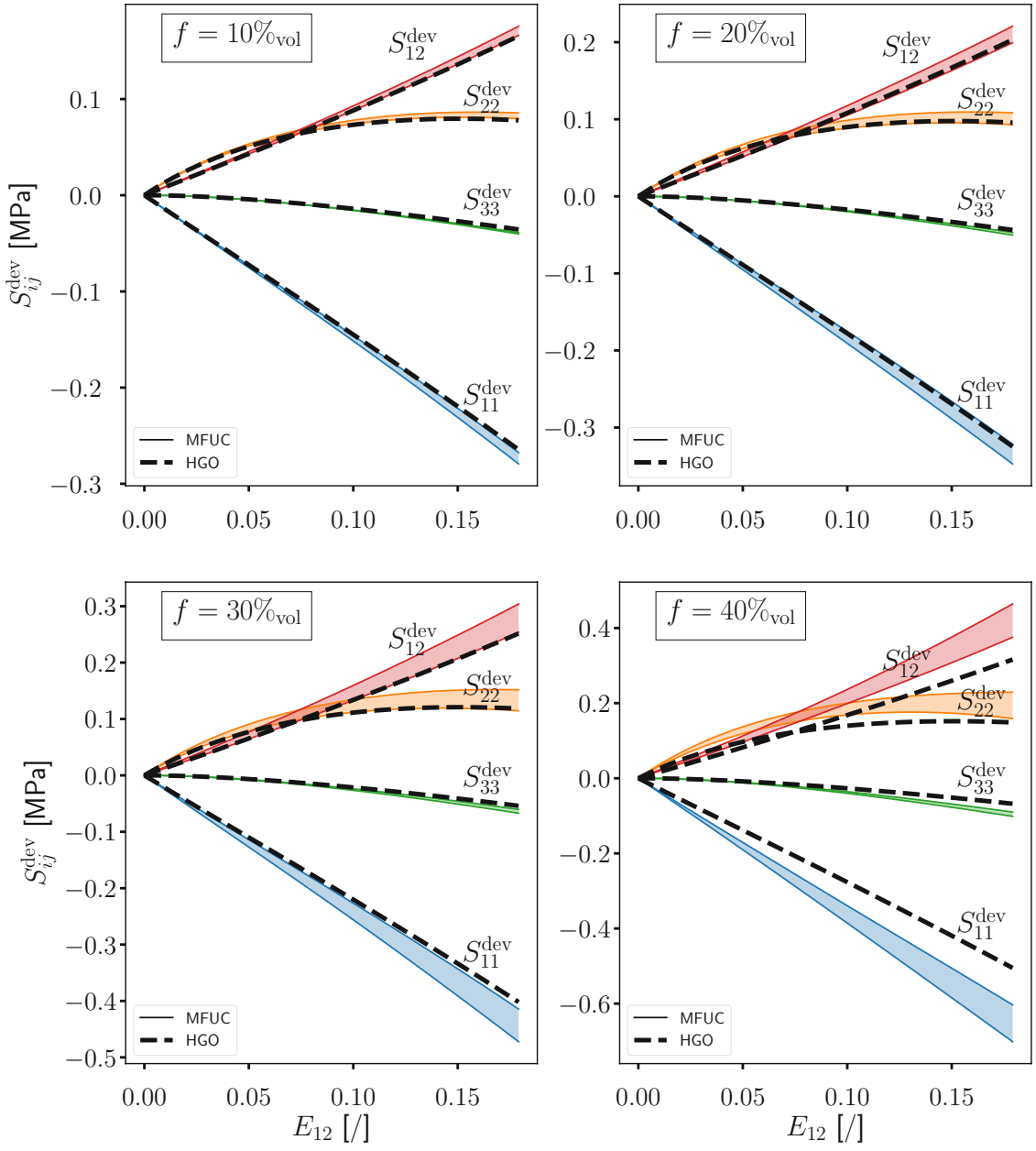

Figure 4.9: Predictions for the FRE material behaviour under transverse load given by multi-fibre unit cell (MFUC) simulation and single element simulations with the calibrated HGO model. Components of the second Piola-Kirchoff stress deviator, S_{ij}^{dev}, are plotted versus the in-plane component of the Green strain, E_{12}, for different fibre volume fractions.

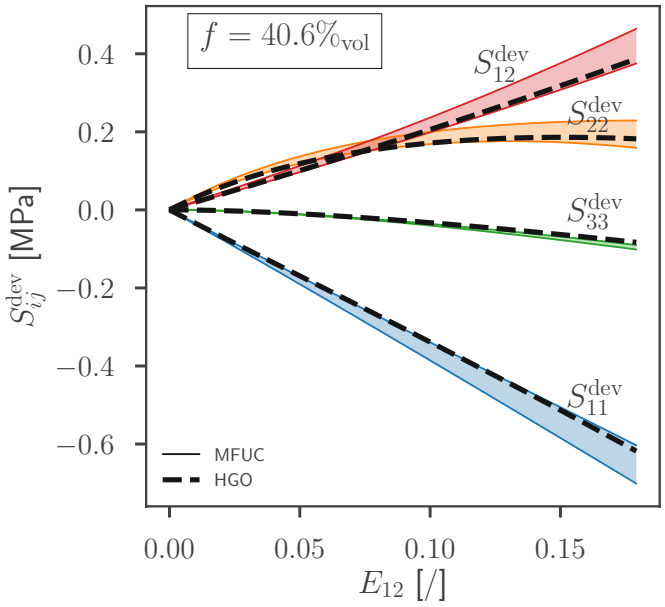

Figure 4.10: Single elements result of the HGO model calibrated with the initial properties of the multi-fibre unit cell with 40.6% fibre volume fraction.

4.4.2 Axial load

The axial load case applies shear in the fibre direction which is combined with small fibre extension to ensure tensile loads in the fibre direction. To maintain an isochoric state, the necessary contraction in the 2 direction is applied. Displacement boundary conditions are prescribed to obtain the final macroscopic deformation gradient

$$\mathbf{F}^{\text{axi}} = \begin{bmatrix} 1 & 0 & 0.5 \\ 0 & 0.999 & 0 \\ 0 & 0 & 1.001 \end{bmatrix} , \quad (4.33)$$

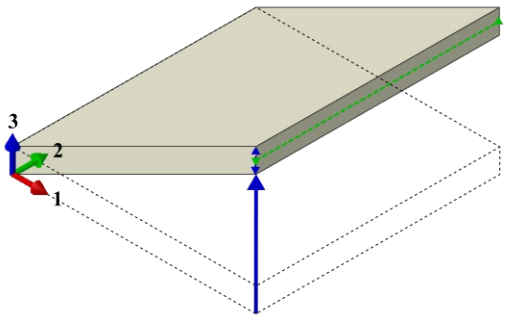

Figure 4.11: Proportional load for the axial load case.

where the maximum principal stretch is $\lambda_{\text{max}} = 1.31$. Figure 4.12 compares the

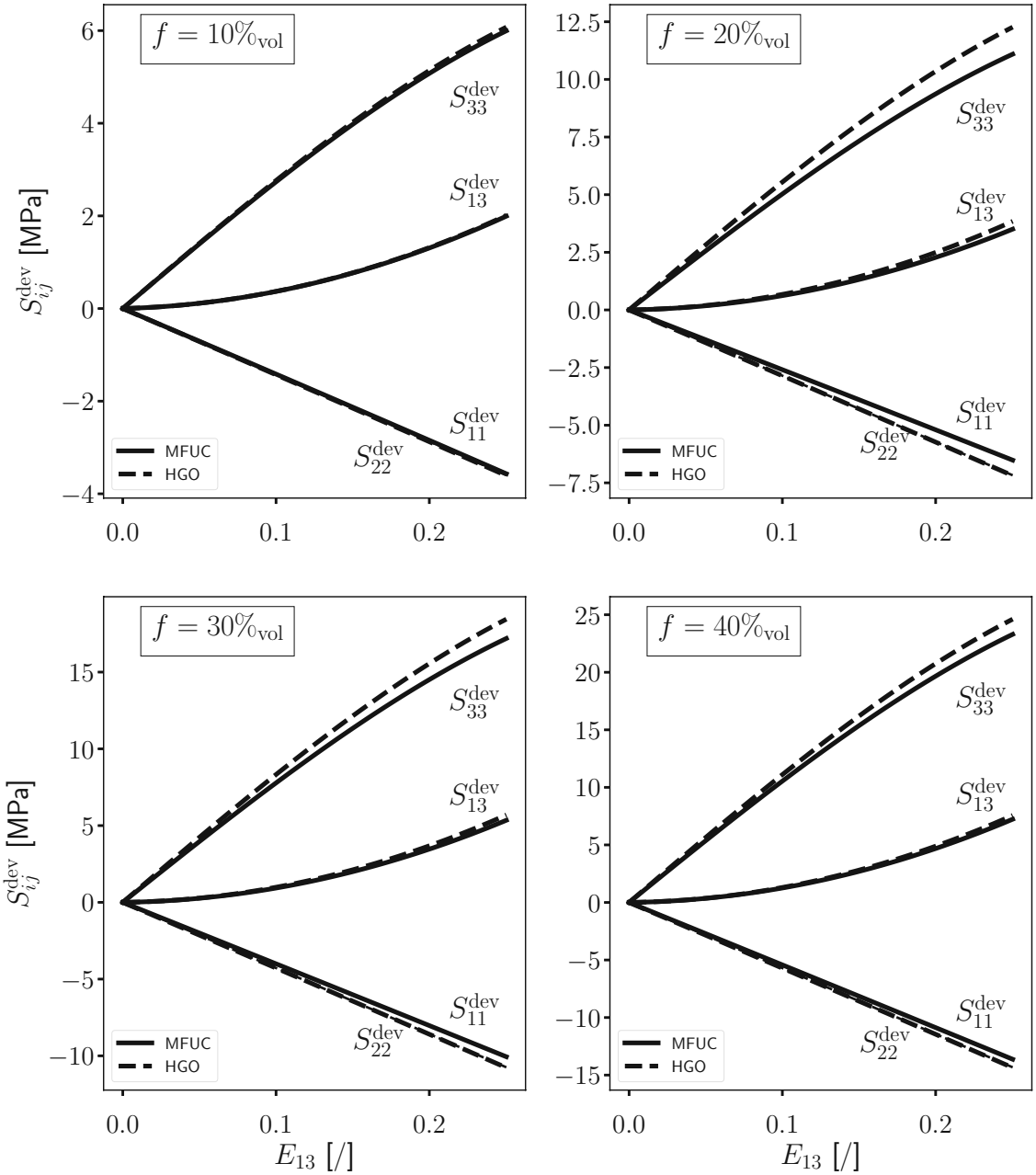

Figure 4.12: Predictions of the FRE material behaviour under axial load given by multi-fibre unit cell (MFUC) simulation and the calibrated HGO model for different fibre volume fractions, f. Components of the second Piola-Kirchoff stress deviator, S_{ij}^{dev} are plotted versus the in-plane shear component of the Green strain, E_{13}.

response of multi-fibre unit cells and single elements with the calibrated HGO model. Results of the unit cells are given for a single direction of zero radians. Predictions

from the calibrated HGO model are in a very good agreement with the effective response from the unit cell throughout the load and fibre volume fractions. Overall the calibrated HGO model overpredicts the effective deviatoric stresses obtained by the multi-fibre unit cells.

4.4.3 Combined load

The combined load effectively combines the previous load cases together, resulting in in-plane shear, out-of-plane shear and axial extension in the fibre direction. The displacement boundary conditions are derived from an isochoric macroscopic deformation gradient

$$\mathbf{F}^{\text{comb}} = \begin{bmatrix} 1 & 0.5 & 0.5 \\ 0 & 0.999 & 0 \\ 0 & 0 & 1.001 \end{bmatrix} , \quad (4.34)$$

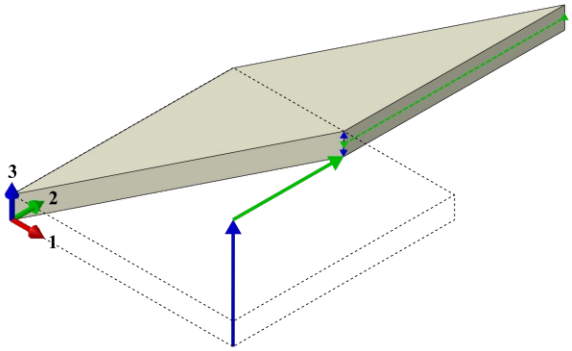

Figure 4.13: Proportional load for the combined load case.

where the maximum principal stretch is $\lambda_{\max} = 1.41$. Figure 4.14 compares the response of the multi-fibre unit cell and the calibrated HGO material model under the combined load for different fibre volume fractions. Predictions for the deviatoric shear stress, S_{13}^{dev}, by the HGO model captures well the progressive response of multi-fibre unit cells.

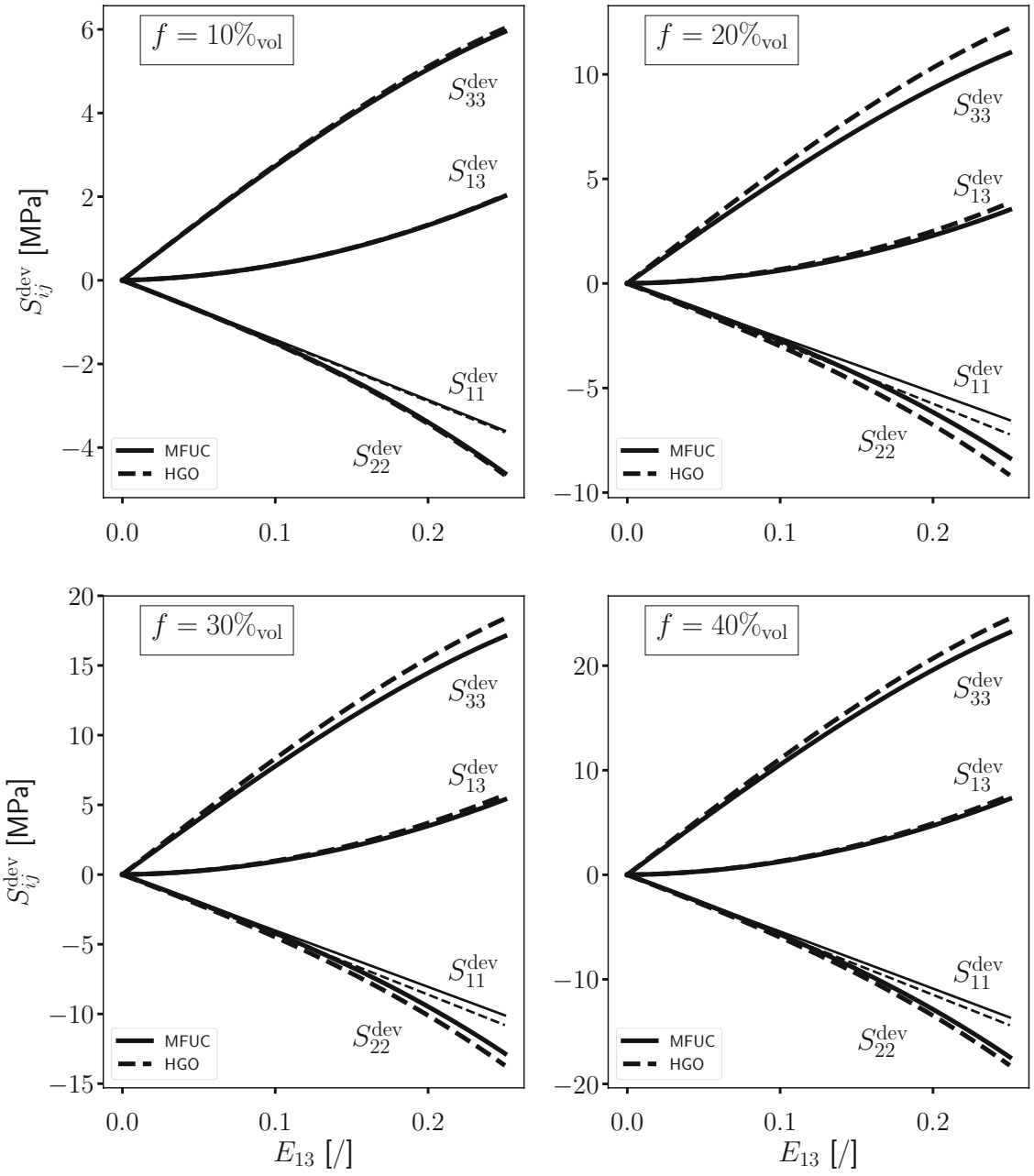

Figure 4.14: Predictions of the FRE material behaviour under combined load given by multi-fibre unit cell (MFUC) simulation and the calibrated HGO material model for different fibre volume fraction, f. Components of the second Piola-Kirchoff stress deviator, S_{ij}^{dev} are plotted versus the in-plane shear component of the Green strain, E_{13}.

4.5 Summary

Fibre reinforced elastomers are studied in the perspective of structural simulations for which a suitable material model is needed. This work uses the readily available Holzapfel-Gasser-Ogden form of the strain energy density function, where a simple but successful calibration method for the material parameters is presented. The effective behaviour of fibre reinforced elastomers is first estimated using multi-fibre unit cells with periodic boundary conditions and quasi random unidirectional fibre arrangements. The behaviour in the plane transverse to the fibres is shown in the initial linearised and in the finite strain regime to assess the direction dependency of the unit cells. Instead of fitting material parameters of the HGO model to obtain a good agreement with the effective behaviour of unit cells, the material parameters are calibrated based on the initial behaviour, which is approximated as linear elastic with transversely isotropic material symmetry. The initial deviatoric elasticity tensor is obtained for both the HGO model and the multi-fibre unit cell prediction. By correlating individual components, material parameters of the HGO model are calibrated with the effective initial shear and Young's modulus of the composite at the "undeformed" state of the material. The initial behaviour is approximated with the Mori-Tanaka method and consequently the calibration avoids the numerical homogenisation schemes altogether. Results show very good agreement between the predictions of the calibrated HGO model and the effective behaviour of multi-fibre unit cells under various load cases and for a range of fibre volume fractions. Nevertheless, the calibration method is limited to composites with very high contrast between the initial shear modulus of fibres and matrix, which justifies the assumptions of equal initial shear modulus in the axial and transverse direction. However, the advantage is the simplicity of the calibration method, which is shown to work well for the presented load cases. In engineering applications where tailoring the material to specific loads is important, such method can help to substantially reduce the optimisation process due to its simplicity and accuracy.

Chapter 5

Nonlinear homogenisation of a FRE laminated unit cell

5.1 Introduction

The effective response of a cross-ply FRE laminate with four plies assembled in a $[90/0]_s$ layup is studied with the nonlinear homogenisation framework used in Chapter 4. The effective response of a laminated multi-fibre unit cell is compared to a homogenised model under two load cases, i.e. pure shear and simple shear loading. The homogenised model is equipped with the anisotropic hyperplastic HGO material and material parameter calibration given in Chapter 4.

5.2 Modelling

5.2.1 Laminate unit cell model

The laminate unit cell is created by taking two multi-fibre unit cells, assembling them in a [90/0] sublaminate, which is mirrored over the top surface and hence creating a symmetric $[90/0]_s$ laminate layup as depicted in Fig. 5.1, where the fibres are oriented

in the 1 and 2 axis. The fibre distribution for the multi-fibre unit cells is generated using `Digimat FE`.

The fibres account for 40,91% volume fraction in each ply. The fibre arrangements are generated using `Digimat-FE`. Thereby, cut-off fibres are only allowed on one pair of surfaces, as the plies exhibit plane periodicity only (1–2 plane), cf. Fig. 5.1. In addition, a thin layer (with the width of a fibre) of pure matrix material is placed between the plies where large shear deformation is expected. Consequently, this reduces the need for a very fine discretization in the region between the plies, making the model more computationally efficient. Overall, the fibres represent 38.88% of the total volume of the laminate unit cell. The material properties of the constituents are the same as in the previous Chapter, cf. Tab. 4.1. The interface between the fibres and the matrix is assumed to be perfect. Continuum eight and six node elements are used for discretization. The average element size in the laminate unit cell is 0.01 mm, which results in approximately one and a half million elements and six million variables (degrees of freedom plus number of Lagrange multiplier variables) for the whole model. The model is equipped with planar periodic boundary conditions in the 1-2 plane.

5.2.2 Homogenised model

Following the approach from Chapter 4, where single element test results are compared to the effective response of the multi-fibre unit cell, a so called homogeneous unit cell is used here, which represents the laminate using continuum element based model equipped with the calibrated HGO material and periodic boundary conditions. Each ply in the model is discretizied using eight node continuum elements and assigned with the corresponding local coordinate system to create the $[90/0]_s$ material orientation. Note that the non-hybrid finite elements have to be used for anisotropic hyperelastic materials [23]. The HGO material parameters for 40% fibre volume fraction are used, see Tab. 4.2 and Eqs. (4.31) and (4.26).

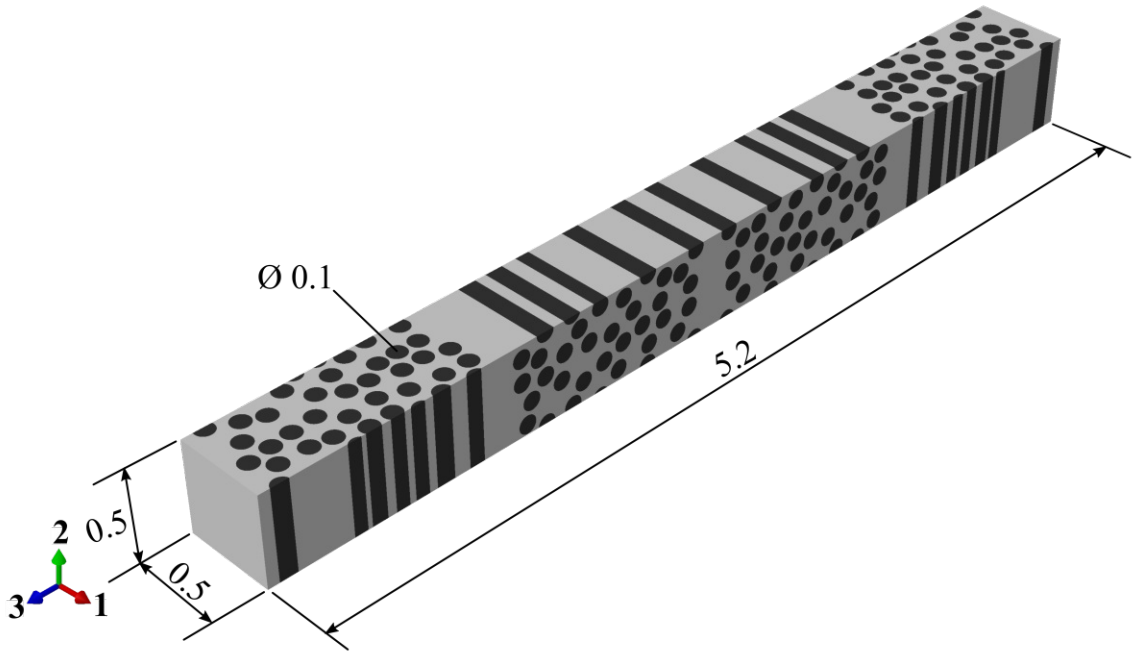

Figure 5.1: Cross ply laminate unit cell with $[90/0]_s$ ply layup. The dimensions are in millimetres.

5.3 Results and discussion

5.3.1 Pure shear loading

The pure shear loading in the 1-2 plane is defined with the isochoric macroscopic deformation gradient in the end state

$$\mathbf{F} = \begin{bmatrix} 1.25 & 0.75 & 0 \\ 0.75 & 1.25 & 0 \\ 0 & 0 & 1 \end{bmatrix} , \qquad (5.1)$$

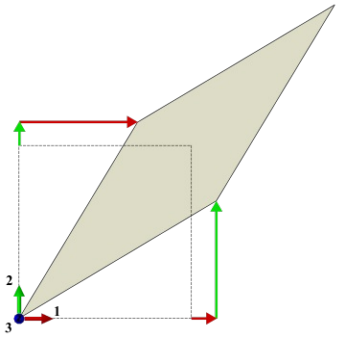

Figure 5.2: Proportional load for pure shear loading.

from which the displacements of master nodes are derived and prescribed in the simulation. Throughout the loading the volume is preserved, which requires non-linear displacement increase for selected displacement direction on master nodes, cf. Appendix B.

Effective strain energy density is evaluated for the multi-fibre unit cell and the homogenised model in Fig. 5.3. On the bottom, deformation state of the laminate unit cell is depicted at $\lambda_{12} = 0.4$ and $\lambda_{12} \approx 0.75$, respectively. Up to $\lambda_{12} = 0.4$ both the homogenised model and the laminate unit cell models are in good agreement. Upon further loading, the homogenised model exhibits larger exponential increase in the effective strain energy density. Pure shear is a non-rotational strain, hence the material orientations in the homogenised model do not change during the loading and remain co-aligned with the global coordinate system. The fibre directions in the HGO model are defined in terms of the local material coordinate system. Consequently, the material orientation in the HGO model remain aligned with the global coordinate system. However, it is clear that fibres do rotate in the microstructure as seen in the Fig. 5.3 (right) and in fact are parallel to unit cell faces. The HGO model is unable to model fibre rotation in this case, which leads to a "lock-up" effect at higher stretches, which is a results of extensive fibre extension compared to the laminate unit cell.

As the unit cell is expanding in 1 and 2 direction, the strain energy density in both models is mainly attributed to the contribution from the fibres. At relatively low stretch, where the fibre rotation is small, the homogenised model predicts the effective behaviour of the laminate unit cell with good agreement. This is also shown on Figs. 5.5 and 5.4 which depict the deviatoric PK2 stress components, S_{12}^{dev} and S_{11}^{dev}, in relation to the stretch λ_{12}, respectively. On the right side of the figure, the stress response is compared at lower stretches that indicate more clearly at which point the homogenised model predictions start to deviate from the laminate unit cell.

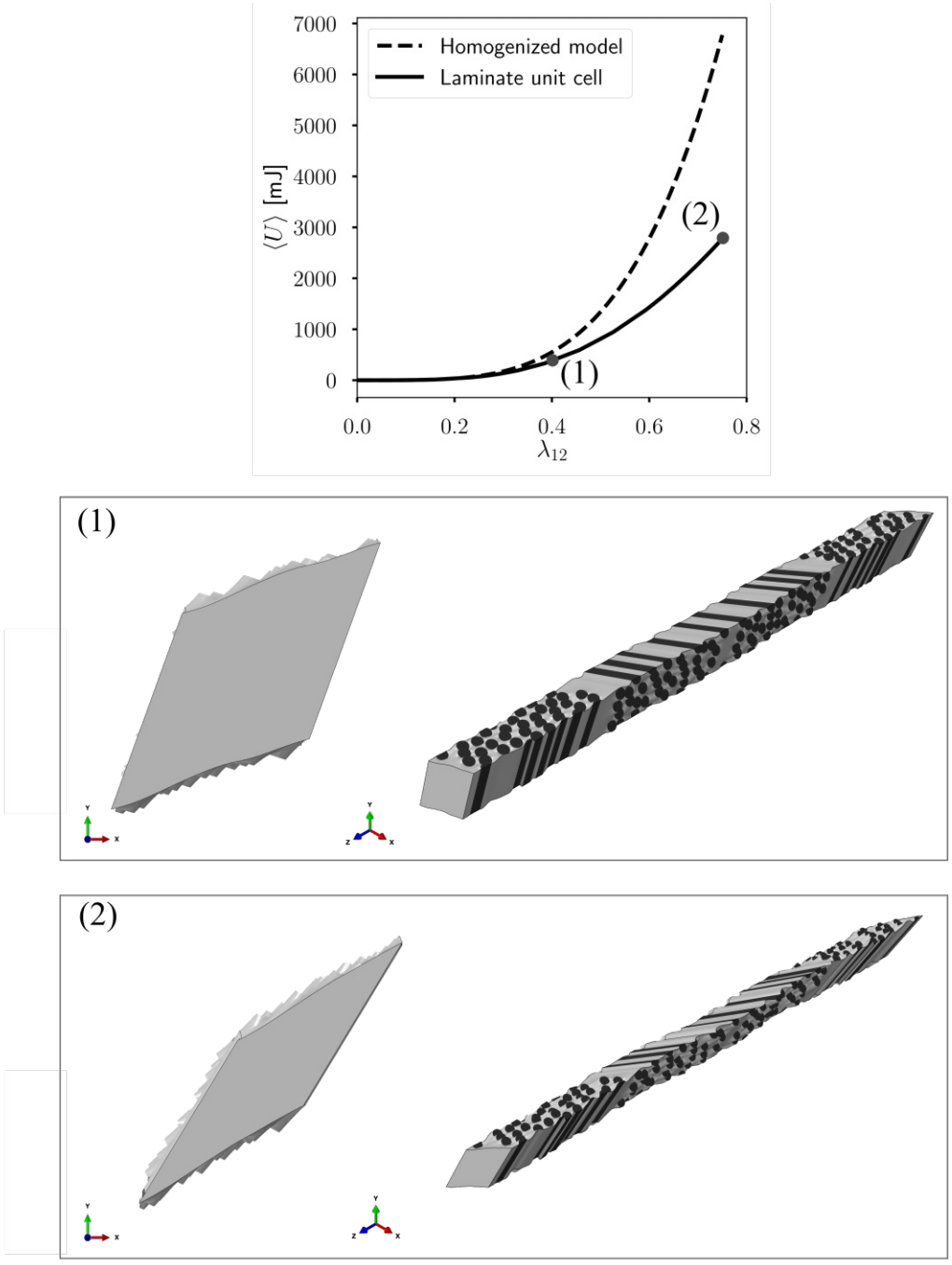

Figure 5.3: Effective strain energy density comparison between the homogenized model with calibrated HGO material and the laminate unit cell model under pure shear loading. On the bottom the deformation states are shown at depicted stretch λ_{12}.

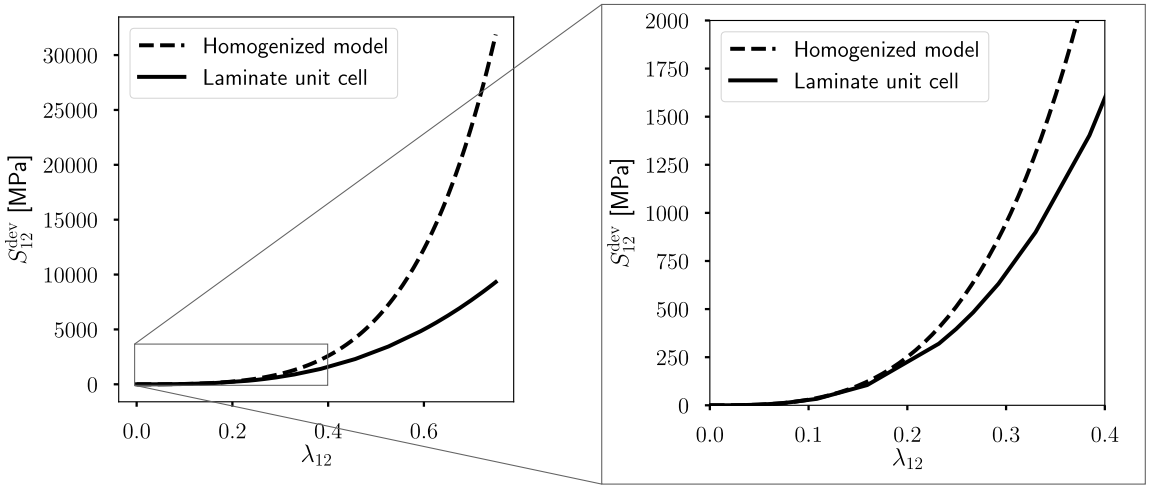

Figure 5.4: Deviatoric PK2 stress component, S_{12}^{dev}, versus the stretch component λ_{12}.

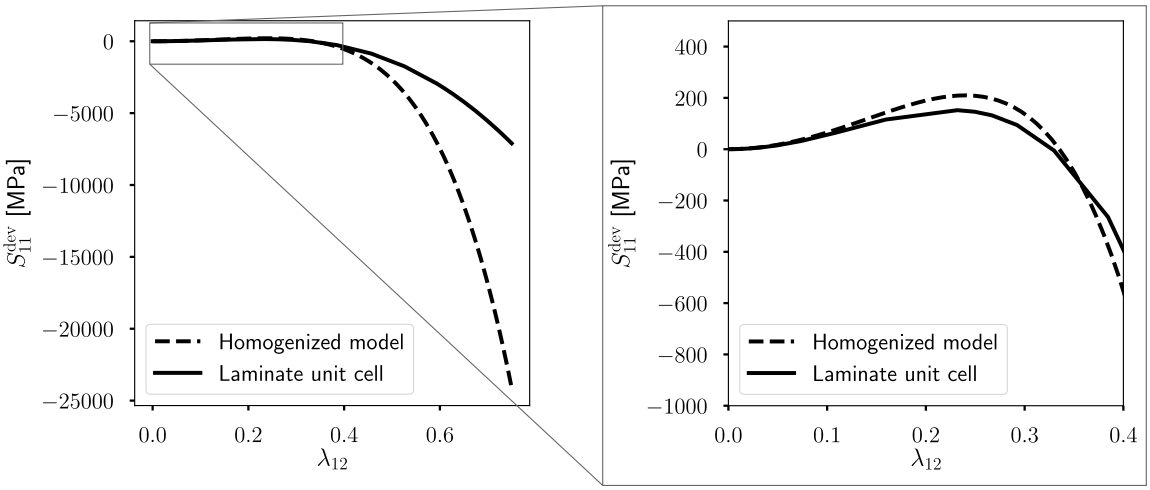

Figure 5.5: Deviatoric PK2 stress component, S_{11}^{dev}, versus the stretch component λ_{12}.

5.3.2 Simple shear loading

The second load case is a simple shear loading in the 1-2 plane. Note that the deformation gradient is the same as in the transverse load case for the FRE material in Chapter 4, but the fibre directions are different in this case, therefore for a single ply, this load case is similar to the axial load case, cf. Eq. (4.33). The displacement of the master nodes are derived from the macroscopic deformation gradient

$$\mathbf{F} = \begin{bmatrix} 1 & 0.5 & 0 \\ 0 & 1 & 0 \\ 0 & 0 & 1 \end{bmatrix} \quad , \qquad (5.2)$$

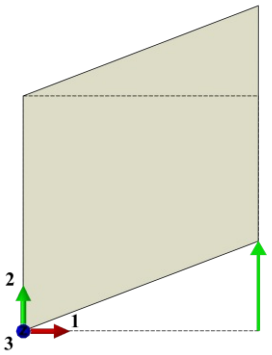

Figure 5.6: Proportional load for pure simple loading.

Compared to the pure shear load case, simple shear is a rotational strain. Therefore, rotation of the material orientation is expected in the homogenised model.

Figure 5.7 compares the effective strain energy density of the laminate unit cell model with the homogenised model. In Chapter 4 it has been shown that for 40% fibre volume fraction the estimates for the initial effective shear modulus is 22% higher when obtained with the linear homogenisation unit cell method (MFUC) compared to the Mori-Tanaka method (MTM). In Fig. 5.7 both cases are included in the homogenised model. In the case of simple shear loading, fibre extension is much less present, resulting in overall much lower effective strain energy densities compared to the pure shear load case. The prediction of the homogenised model with material parameters calibrated by the Mori-Tanaka method shows lower strain energy density compared to the laminate unit cell, as expected from the results in the previous Chapter for 40% fibre volume fraction. The homogenised model with material parameters calibrated by the initial multi-fibre unit cell response gives a higher prediction of the strain energy density and is in very good agreement with the laminate unit cell results. In general the homogenised model gives a good prediction of the strain energy density under the simple shear loading, since in this case the material orientation does rotate as depicted on the Fig. 5.8 (right). Thereby, the fibre directions in the homogenised model are still orthogonal, but are closer to the fibre orientation in the laminate unit cell model, cf. Fig. 5.8 (right).

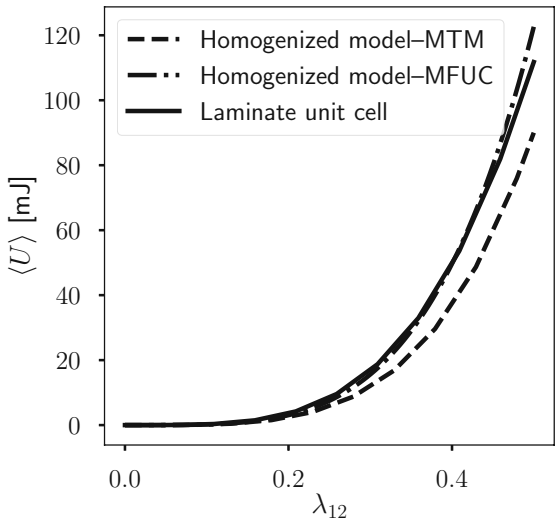

Figure 5.7: Effective strain energy density comparison between the homogenised models with calibrated HGO material and the laminate unit cell model under simple shear loading.

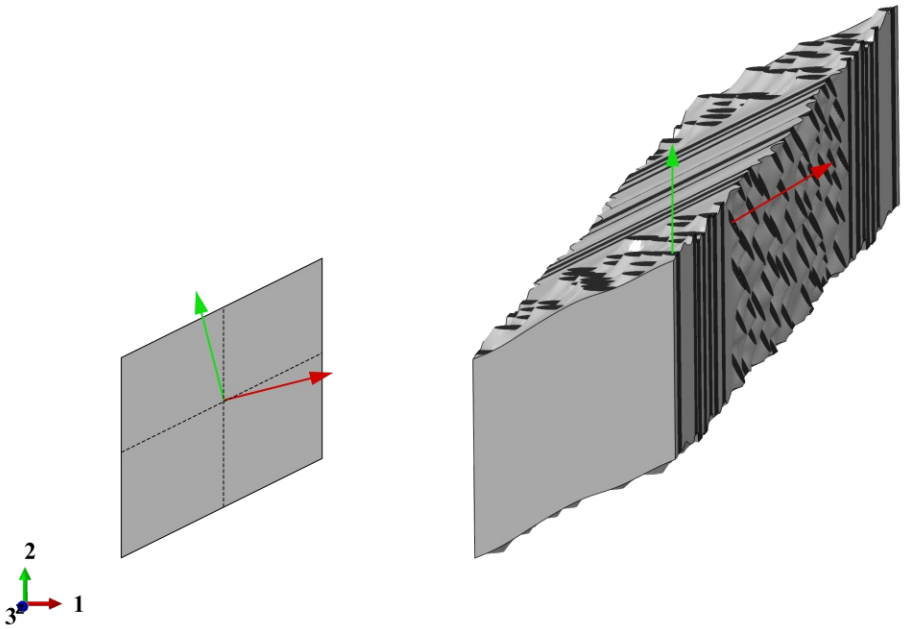

Figure 5.8: Local material direction in the homogenised model (left) compared to the fibre direction in the laminate unit cell (right).

5.4 Summary

The effective behaviour of cross-ply FRE laminate is studied using the nonlinear homogenisation unit cell approach. In the homogenised model, the HGO material is used and the calibration of the material parameters is given in Chapter 4. Therefore, no material parameter fitting is conducted and the homogenised model represents real predictions of the effective behaviour of the laminate unit cell. The effective response of both models are compared under pure shear and simple shear load cases The shear deformation is applied in the 1-2 plane, with fibres oriented in the 1 and 2 axis, respectively. The fibre contribution in the HGO model relies on the local material orientation, which in pure shear does not rotate. Consequently, the homogenised model overpredicts the effective strain energy density of the laminate unit cell model due to excessive contribution of the fibre component in the HGO strain energy density function. Simple shear on the other hand is a rotational strain. In this case the local material coordinate system remains orthogonal, however, it does rotate which somewhat better approximates the fibre orientation in the laminate unit cell. Thereby, the homogenised model is able to predict the effective response of the laminated unit cell with good agreement for moderate stretches.

Chapter 6

Wrinkling of thin FRE shells under tensile load

6.1 Introduction

Instabilities such as buckling or snap-through phenomena are typically associated to compressive loads. However, in lightweight structures it is common that instabilities can occur for elastic structures under global tensile loads, for which the Ref. [80] gives a comprehensive review. A particular case of such instability is wrinkling of thin shells under tensile load, which has received considerable interest within the literature, in particular for isotropic materials [31, 32, 45, 60, 75]. More recently, wrinkling of thin fibre reinforced anisotropic shells has been addressed in Ref. [62, 99], where the orientation of the wrinkle is studied with respect to the material and loading direction. Wrinkling of thin shells can be used to realize structures with multiple functions such as measuring of material properties [51], tunable optical transmittance [61], highly electroactive surface [34], and respiration sensors [102].

In this work, an analysis on wrinkling of thin FRE shells under tensile load is presented using standard computational methods such as the Newthon-Raphson iterative method and the linear buckling analysis as implemented in the FEM package `Abaqus`.

6.2 Modelling

The rectangular shell measures 1000 mm in length (L), 500 mm in width (B) and 0.5 mm in thickness (t), thus having an aspect ratio $L/B = 2$, cf. Fig. 6.1. The calibrated HGO material is used with 10% fibre volume fraction from Chapter 4, cf. Tab. 4.2 and Eqs. (4.31) and (4.26). Two models are considered, a single ply model with fibres oriented under -45 degrees and a laminate model with a [+45/-45] ply layup. The short edges are clamped which prevents the lateral displacement due to Poisson's contraction. Tension in the plate is introduced by displacing one of the clamped edges along the longitudinal axis, x, see Fig. 6.1. The plate is discretized using four node thin shell elements with reduced integration at the mid-surface. The element size is 10 mm and three integration points are used through the thickness of a ply.

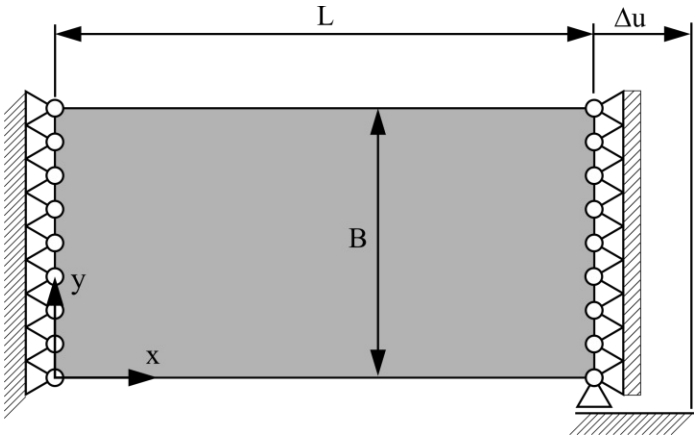

Figure 6.1: The geometry and boundary conditions of a confined FRE tape under tension.

6.3 Linear eigenvalue analysis

Wrinkling of the thin shell under global tensile loads is predicted by the linear eigenvalue analysis. In order to find positive eigenvalues, a preload close to the critical load is necessary. Otherwise, the linear eigenvalue analysis predicts the lowest eigenval-

ues to be negative which would describe the buckling under compressive loads. The preload analysis is conducted with a restart capability, which enables the analysis to be restarted from any increment. This is used to conduct the linear buckling analysis and to estimate the critical load for wrinkling as

$$F^* = F_{\text{pre}} + \lambda F_{\text{buckle}} \quad , \tag{6.1}$$

where F_{pre} is the reaction force in the preload step, λ the eigenvalue and F_{buckle} is the force applied in the linear eigenvalue analysis. If the F_{pre} approaches the critical load, the lowest eigenvalue approaches zero.

The linear eigenvalue analysis always predicts the eigenvalues with the smallest magnitude and sorts them with increasing magnitude. If the preload is far from the critical point the eigenvalue with the smallest magnitude could be negative, and so might be also the consecutive eigenvalues. Only when the preload is close to the critical load the magnitudes of the lowest positive eigenvalues become smaller than the negative ones. In this work, the linear eigenvalue analysis is run at selected increments of the preload and the first two eigenmodes are extracted. Consequently, the critical load is estimated only when the lowest eigenvalue is a positive one.

When the critical load is exceeded, negative eigenvalue warning is issued by the `Abaqus` implicit solver and the linear eigenvalue analysis finds either negative eigenvalues or fails to converge. The linear eigenvalue analysis uses the subspace iteration algorithm as implemented in `Abaqus` [7, 23].

Single -45 ply model

Figure 6.2 depicts the load displacement response (top left) with estimated critical loads for the first two eigenmodes from the linear eigenvalue analysis. On the top right, the minimal principal stress is illustrated at the estimated critical load, showing the compressive stresses influenced by the fibre orientation (local material orientation) at the shell's mid surface. The minimal principal stress is used, since the

stress distribution transverse to the fibres, σ_{22}, includes contributions from the global tension due to the fibre direction. Consequently, stresses transverse to the fibres are positive throughout the model. At the bottom, the first two positive eigenmodes are depicted. The eigenmodes exhibit wrinkles between the two regions with the highest amplitude of compressive stress in Fig. 6.2 top right. Thereby, the wrinkles appear under a slight angle relative to the material orientation. Higher eigenmodes exhibit larger number of wrinkles.

Laminate [+45/-45] model

Figure 6.3 shows the linear eigenvalue analysis with a preload of the cross ply laminate. On the top right, the minimum principal stresses in the -45 ply are illustrated (the stress distribution is similar in both plies). Thereby, a clear pattern from the cross ply layup is shown, with a rectangular area of compressive stress at the centre of the shell. In the bottom of the Fig. 6.3 the first two positive eigenmodes are shown. The wrinkles are aligned with the longitudinal direction and are symmetric with respect to the lateral plane y-z at the middle of the shell. In contrast to the single ply, the first positive eigenmode exhibits a higher number of wrinkles compared to the second mode.

6.4 Post-buckling analysis

A geometrical imperfection is introduced on the shell mid-surface in the undeformed configuration (initial state) by using the eigenmodes from the linear eigenvalue analysis. The predicted post-buckling behaviour in general may depend on the number of eigenmodes and their amplitude that are used as the imperfection. An imperfection sensitivity analysis can be used to determine this influence, in particular for bifurcation behaviour under compressive loads. In the case of wrinkling of shells under tension, the imposed imperfection can have a strong influence on the convergence of the solution.

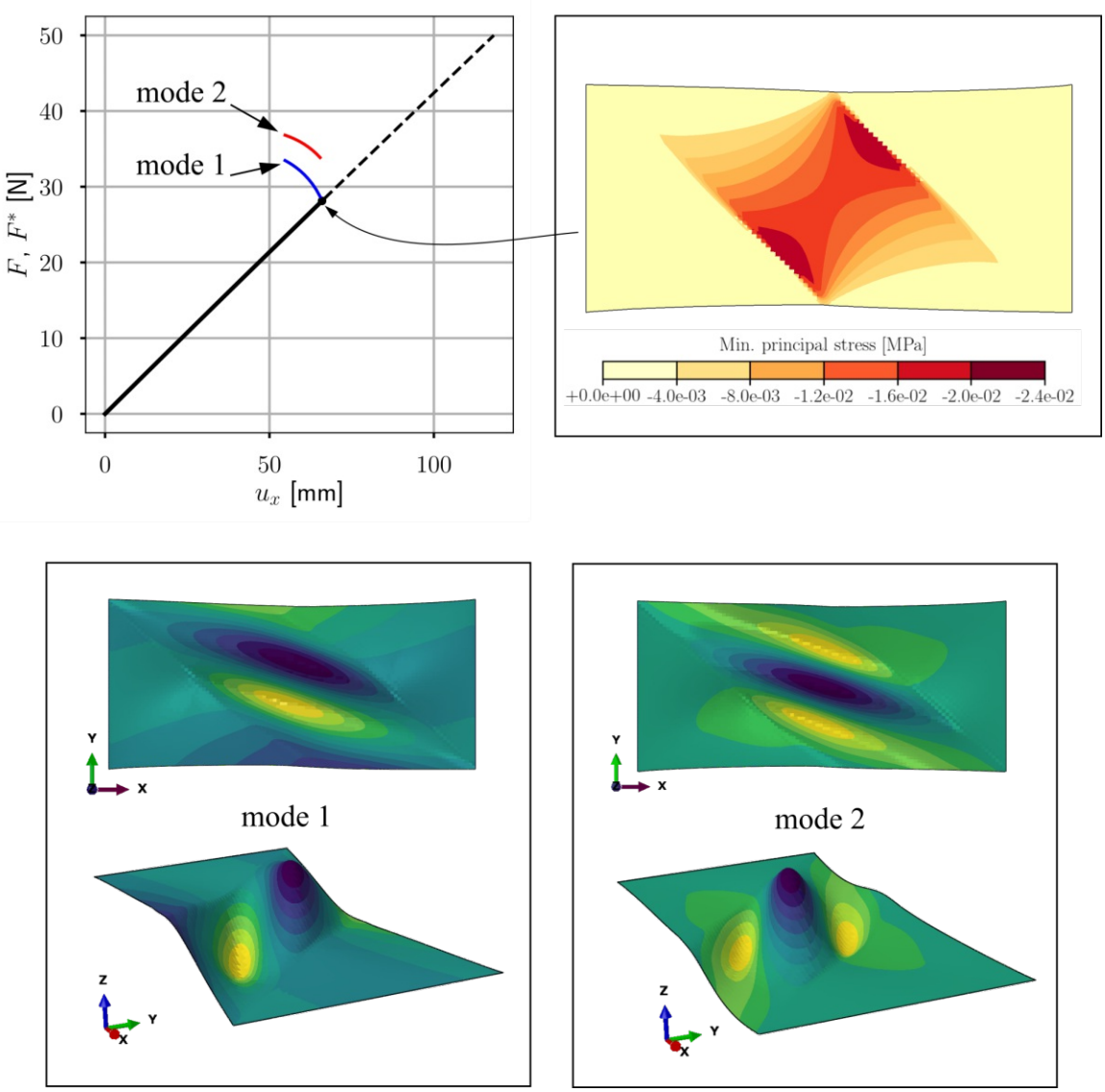

Figure 6.2: Linear eigenvalue analysis with a preload of a single ply FRE tape with -45 fibre orientation. The minimum principal stresses at the critical load are depicted on the top right. The first two eigenmodes are depicted on the bottom.

In this work, only the eigenforms corresponding to the first two positive eigenvalues from the linear eigenvalue analysis at the critical load are used as imperfection. For both single ply and laminate models the imperfection is mapped on the shell mid-

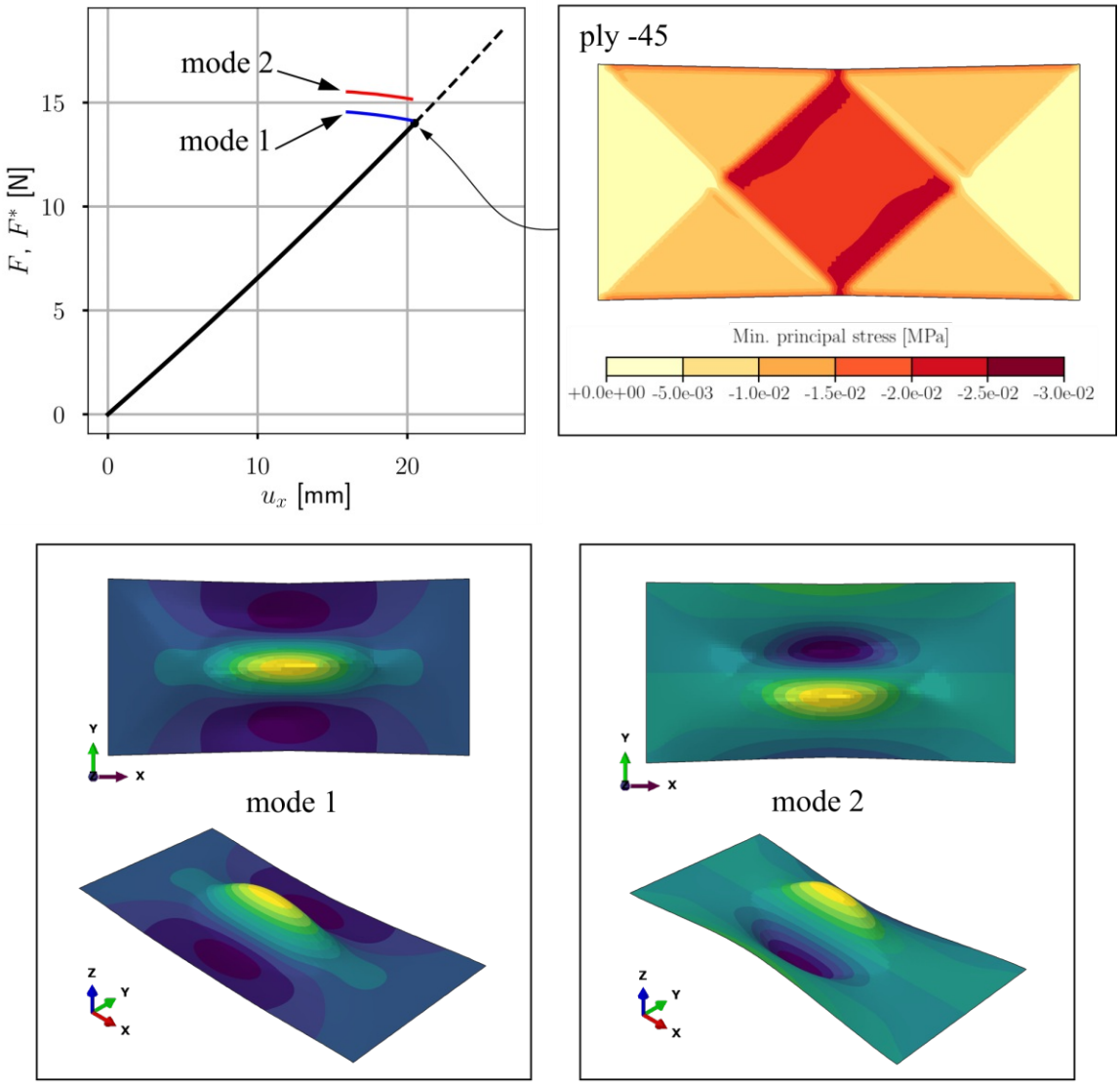

Figure 6.3: Linear eigenvalue analysis with a preload of the cross ply laminate FRE shell with a [+45/-45] ply layup. The minimum pricipal stresses in the -45 ply at the critical load is depicted on the top right. The first two eigenmodes are illustrated at the bottom.

surface as a superposition of the first two corresponding eigenmodes. The first eigenmode is scaled with 0.1% of the shell thickness and the second mode with 0.05%. A displacement controlled Newton-Raphson iterative method as implemented in `Abaqus` is employed for the post-buckling simulations.

Figure 6.4 shows the evolution of the stretch-induced wrinkles for the single -45 ply FRE shell. At three different load points, cf. Fig. 6.4 (top left), the lateral cross sections at the middle of the shell are depicted on the Fig. 6.4 (top right). Prior to the critical load, i.e. point (1) in Fig. 6.4, the wrinkling develops from the imperfection in an exponential way, with the largest wrinkling amplitude at the critical load. Beyond the critical load, the wrinkling amplitude is decreasing. In addition, the analysis shows a change in the wrinkling pattern. At the critical load, i.e. point (1) in Fig. 6.4, the wrinkles are formed according to the first eigenmode, cf. Fig. 6.2, with an amplitude of 2.5% of the shell thickness. At point (2), the wrinkling pattern gradually switches to the second positive eigenmode from the buckling analysis with lower amplitude. This pattern continues with increasing load where at point (3) a higher number of wrinkles is predicted but with very low amplitude. At the bottom of the Fig. 6.4 the out-of-plane deformation of the whole shell is shown at corresponding loading points. The dashed line at the middle indicate the lateral cross sections in Fig. 6.4 (top right).

Figure 6.5 shows the post-buckling analysis of the [+45/-45] laminate shell. On the top left, the out-of-plane displacement, u_z, of the point in the centre of the shell is depicted versus the longitudinal displacement of the clamped edge. The out-of-plane displacement of the central point is increasing towards the critical load, i.e. point (1), and one increment before a snap-through phenomenon occurs, resulting in a wrinkling pattern that is a mirrored shape of the first eigenform predicted by the linear buckling analysis. The exact reason for this behaviour is unknown and needs further investigation. However, there are several possible reasons which may lead or contribute to this behaviour:

(i) The eigenforms computed from the linear eigenvalue analysis might not be the correct ones, since the buckling analysis as implemented in `Abaqus` linearises the material behaviour. Consequently the post-buckling behavior might not be estimated correctly.

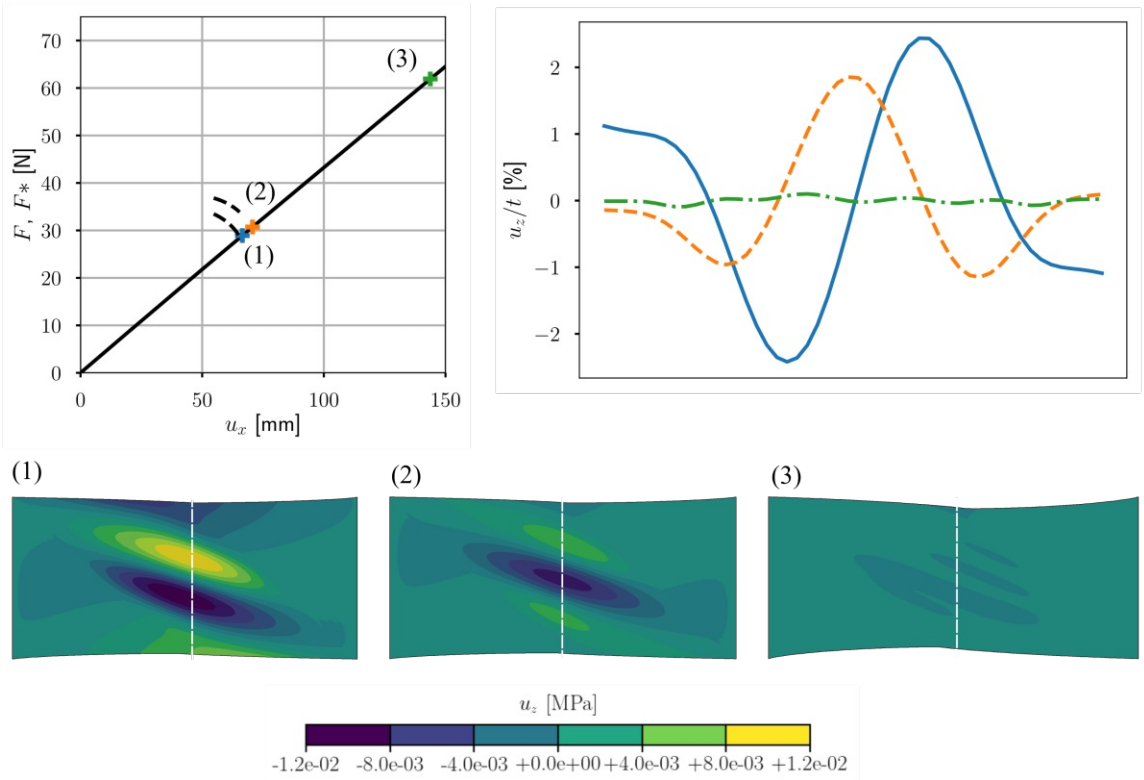

Figure 6.4: Post buckling analysis of a single -45 ply FRE shell. On the top left, the load displacement response with the imperfection is depicted with the critial loads for the first two eigenmodes. On the top right, the lateral cross sections at the middle of the shell are illustrated at load points annotated on the load displacement curve. In the bottom, the out-of-plane deformation of the whole shell is shown for the corresponding load points.

(ii) The HGO material model is formulated such that the fibres do not contribute to the compressive stress state. This causes a different material behaviour under tension and compression, which may lead to significant stiffness increase in regions which were under compression prior to buckling and under tension after buckling. The formulation of the HGO model may also lead to issues in the prediction of the eigenforms so this point is closely related to point (i).

(iii) The unsymmetrical ply layup of the laminate produces out-of-plane deformation on its own, which might in combination with the wrinkling lead to the snap-

through behaviour. However, the snap-through behaviour still occurs if the eigenforms are mapped with negative amplitudes as imperfection.

At the critical load, point (1), the wrinkles reach the maximum amplitude of approximately 30% of the shell's thickness, followed by a sharp decrease in amplitude. The deformation shape at the lateral cross section in the centre retains the shape of the first positive eigenmode, cf. Fig. 6.5 (top right). At the bottom of Fig. 6.5 the out-of-plane deformation of the whole shell is depicted at the corresponding loads. At the critical load, i.e. point (1), the out-of-plane deformation resembles the first eigenmode from the buckling analysis, cf. Fig 6.3. However, the deformation is point symmetric with respect to the centre whereas the first eigenmode is symmetric with respect to the lateral plane y-z at the middle of the shell, cf. Fig. 6.3. The unsymmetrical ply layout results in out-of-plane deformation at the free edges which is increasing with load. The total out-of-plane deformation is a superposition of the wrinkling caused by the compressive loads around the centre of the shell and the deformation due to unsymmetric layup. At load point (3) the wrinkle in the middle of the shell almost flattens out. At the same time, the out-of-plane deformations increase at the free edges of the shell due to the unsymmetrical ply layup, and the point symmetric out-of-plane deformation with respect to the centre point remains throughout the longitudinal stretching.

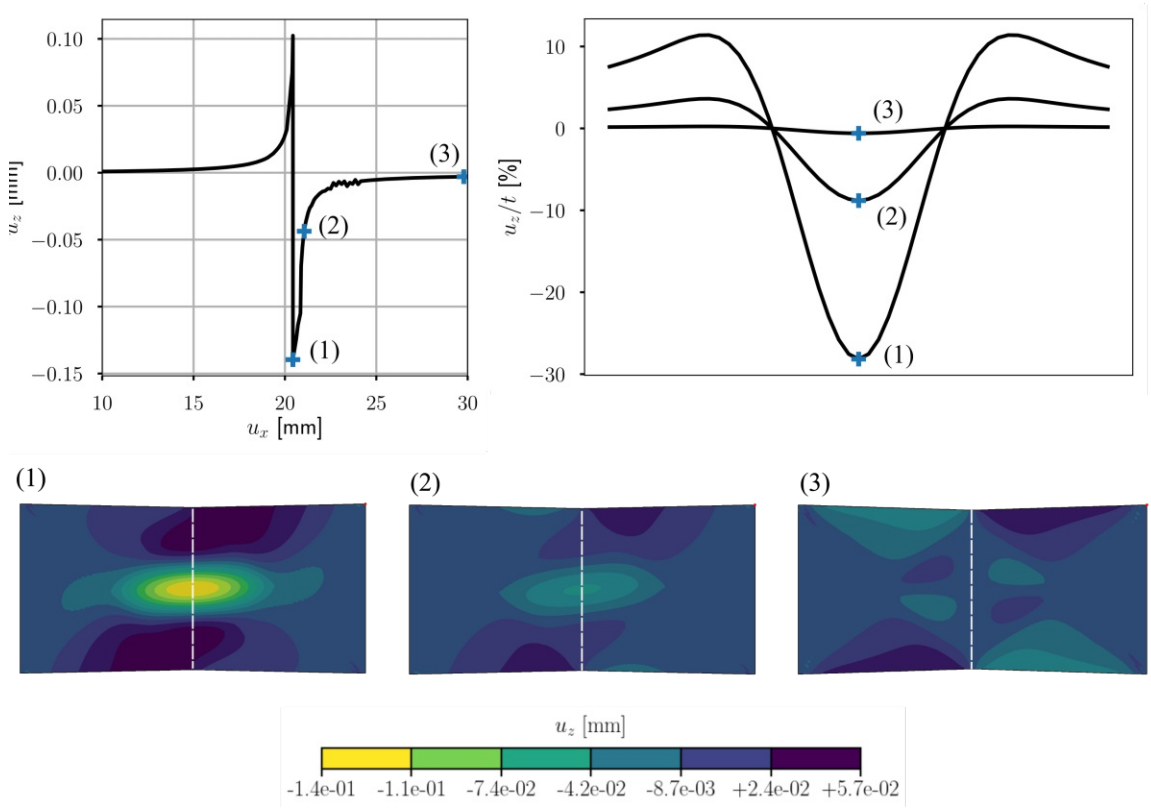

Figure 6.5: Post buckling analysis of a [+45/-45] laminate FRE shell. On the top left, the out-of-plane displacement, u_z, of the point in the centre of the shell versus the longitudinal displacement of the clamped edge is depicted. On the top right, the lateral cross section at the middle of the shell is illustrated at corresponding load points. The out-of-plane displacement of the whole shell at the corresponding load points is shown at the bottom.

6.5 Summary

The behaviour of thin FRE shells under tensile loads is studied by means of FEM simulations. A small aspect ratio shell is clamped on short edges and stretched in the longitudinal direction by displacing one of the clamped edges. The calibrated HGO material with 10% fibre volume fraction from Chapter 4 is employed in a single -45 ply model as well as in a cross-ply [+45/-45] laminate model. A linear eigenvalue analysis is conducted to find the positive eigenvalues close to the critical buckling load. The compressive stress distribution in the shell is influenced by the material orientation, which in the case of the single -45 ply model results in wrinkles that are aligned with the fibre direction. The cross-ply laminate model exhibits symmetric compressive stress distribution at the critical load which yields symmetric eigenmodes. In both the single ply and the laminate model, the first two eigenmodes are used as imperfection. The post-buckling analysis of the single -45 ply model is in agreement with the observations from the literature, which report appearance of wrinkles around the critical load with their disappearance at larger global tensile loads. Moreover, the results indicate mode change of wrinkling as the amplitude of the wrinkles decreases whilst the number of wrinkles increases. In contrast, the wrinkling of the [+45/-45] laminate model follows the first eigenmode with increasing tensile load. However, the post-buckling analysis predicts a snap-through behaviour, which could be a result of multiple reasons and would require further investigation to identify if such behaviour is representative or an artefact. One of the main reasons could be the fact that in the HGO model the fibre contribution is excluded in the compressive stress state, which could result in significant stiffness increase or decrease in regions which switch from compression to tension and vice versa. Beyond the critical load the amplitude of wrinkles is decreasing and the out-of-plane deformation is a superposition of the wrinkles and the out-of-plane deformation caused by the unsymmetrical ply layup.

Chapter 7

Conclusion

In this work, two types of fibre reinforced composites are considered with the perspective of nonlinear FEM simulations.

First, an efficient multi-scale embedding approach for simulation of delamination in textile laminates is presented. Thereby, a detailed representation of the textile plies at the delaminating interface is embedded by a homogenised laminate, which is modelled by the conventional laminate approach. Except for the cohesive interfaces, the entire model is represented by shell elements, making it exceptionally efficient in terms of the computational effort. Moreover, the embedded textile structure offers high predictive capabilities with a resolution that captures the effects during the delamination at the length scales of individual tows. The modelling approach is employed for simulation of delamination in 2/2 Twill Weave carbon reinforced epoxy laminates under the DCB and ENF test set-ups using standard desktop hardware. A clear relation between the local ply stiffness and the size of the process zone in the cohesive interface is obtained, which manifests in a quasi step-wise force reduction in ongoing delamination. This is in agreement with experimental observations in the literature. However, the shell based modelling restricts intra-ply delamination, i.e. separation of individual tows, due to the kinematic constraints between the tows and the matrix. Therefore, modelling phenomena such as delamination migration is very

limited. A possible improvement would be to use cohesive elements to tie the tows to the matrix instead of the "direct" kinematic constrains. In general, the validation of cohesive interfaces is non-trivial since an interface is a structural property rather than a material itself. Nevertheless, the modelling approach recognizes different types of interfaces based on the laminate's topology and has the potential to study in-depth the effects of interface properties.

The second type of composites that are studied within this work are fibre reinforced elastomers, which are used in very different applications compared to fibre reinforced polymers. The advantage of FRE is the rubber-like matrix which allows for large deformations, while the fibres carry loads and dictate the direction dependent response. The combination of both makes FRE suitable not only for structures but also complete mechanisms such as robotic arms or deployable structures. In order to study FRE in such structures an appropriate material model that can accurately predict the effective behaviour is required. A unit cell homogenisation approach is employed in order to estimate the effective behaviour of FRE across different fibre volume fractions. The response of multi-fibre unit cells with quasi random fibre arrangement is studied in the initial linearised and finite strain regime to evaluate the direction dependency of the unit cells. Within this work, the readily available HGO material model is used to predict the effective response of the multi-fibre unit cells. The main contribution is a simple calibration method for the material parameters of the HGO model, which takes place at the initial or undeformed state of the material. The calibration method takes the deviatoric part of the initial linearised elasticity and derives relations between the material parameters and the material properties such as the shear modulus and Young's modulus of a transversely isotropic material. In order to estimate the initial shear and Young's modulus of the FRE material, the analytical Mori-Tanaka method is employed. Thereby, the calibration method entirely omits any numerical homogenisation schemes. Predictions for FRE with high contrast between the initial shear modulus of fibres and matrix are made for various load cases, which do not exhibit compressive stresses in the fibre direction, as the

HGO model cannot model fibre compression. The results show very good agreement between the calibrated HGO model and the effective multi-fibre unit cells for fibre volume fraction up to 40%. The comparison is extended to cross-ply FRE laminates under shear deformations. The HGO model relies only on the material orientation for the fibre contribution in the strain energy density. Consequently, the HGO model is unable to model fibre rotation under moderate shear deformations. This is most evident in the case of pure shear deformation, where the material orientation does not change. Clearly, there is a need for a more suitable anisotropic hyperelastic material model, which would include fibre orientation during deformation. Within the same funding scheme as the present work, such material model has been recently developed by Mansouri et al. [68].

Finally, the calibrated HGO model is employed in a structure. The wrinkling behaviour of thin FRE shells under tensile loads is studied by means of linear eigenvalue analyses with a preload and post buckling analyses. The single ply and the laminate shell model used in this work show the dependency of the wrinkling direction on the material orientation in the shell. The highest amplitude of wrinkles is observed at the critical load and upon further global tension load, the amplitude decreases to the point where no more wrinkling is observed. The post-buckling analysis exposes the limitation of the HGO model, where the lack of fibre contribution under compressive state could lead to non-representative post-buckling behaviour, however, that requires further investigation.

Appendix A

Spherical and deviatoric projection tensors

Fourth order projection tensor can be used to obtain spherical and deviatoric parts (projections) of stress, strain and consequently the elasticity tensor.

The identity fourth order tensor

$$\mathscr{J} = \delta_{ik}\delta_{jl}\,\mathbf{e}_i \otimes \mathbf{e}_j \otimes \mathbf{e}_k \otimes \mathbf{e}_l \quad , \tag{A.1}$$

where δ is the Kronecker delta component and $\mathbf{e}$ are the orthogonal basis vectors. The identity fourth order tensor can be split up into its symmetrical and antisymmetrical parts as

$$\mathscr{J} = \mathscr{J}^{\mathrm{s}} + \mathscr{J}^{\mathrm{a}} \quad . \tag{A.2}$$

The symmetrical part of the identity fourth order tensor is defined as

$$\mathscr{J}^{\mathrm{s}} = \frac{1}{2}(\delta_{ik}\delta_{jl} + \delta_{il}\delta_{jk})\,\mathbf{e}_i \otimes \mathbf{e}_j \otimes \mathbf{e}_k \otimes \mathbf{e}_l \quad . \tag{A.3}$$

The symmetrical identity tensor can be decomposed into the spherical and the deviatoric projection tensors as

$$\mathscr{J}^{\mathrm{s}} = \mathscr{P}_1 + \mathscr{P}_2 \quad , \tag{A.4}$$

where $\mathscr{P}_1$ is the spherical projection tensor defined as

$$\mathscr{P}_1 = \frac{1}{3}\,\mathbf{I} \otimes \mathbf{I} = \frac{1}{3}\delta_{ij}\delta_{kl}\,\mathbf{e}_i \otimes \mathbf{e}_j \otimes \mathbf{e}_k \otimes \mathbf{e}_l \quad , \tag{A.5}$$

where $\mathbf{I}$ is the identity second order tensor. The deviatoric projection tensor, $\mathscr{P}_2$, is defined as

$$\begin{aligned} \mathscr{P}_2 &= \mathscr{J}^{\mathrm{s}} - \mathscr{P}_1 && \text{(A.6)} \\ &= \left[\frac{1}{2}(\delta_{ik}\delta_{jl} + \delta_{il}\delta_{jk}) - \frac{1}{3}\delta_{ij}\delta_{kl}\right] \mathbf{e}_i \otimes \mathbf{e}_j \otimes \mathbf{e}_k \otimes \mathbf{e}_l \quad . && \text{(A.7)} \end{aligned}$$

With the projection tensors, the elasticity tensor, $\mathbf{E}$, can be decomposed into the spherical part as

$$\mathbf{E}^{\mathrm{vol}} = \mathbf{E} : \mathscr{P}_1 \tag{A.8}$$

or in index notation

$$\begin{aligned} E^{\mathrm{vol}}_{ijmn} &= E_{ijkl}\, P_{1(klmn)} && \text{(A.9)} \\ &= \frac{1}{3}\, E_{ijkl}\, \delta_{kl}\delta_{mn} \quad . && \text{(A.10)} \end{aligned}$$

Deviatoric projection of the elasticity tensor is

$$\bar{\mathbf{D}} = \mathbf{E} : \mathscr{P}_2 \tag{A.11}$$

or in index notation

$$\bar{D}_{ijmn} = E_{ijkl}\, P_{2(klmn)} \tag{A.12}$$

$$= E_{ijkl} \left[\frac{1}{2} \left(\delta_{km}\delta_{ln} + \delta_{kn}\delta_{lm} \right) - \frac{1}{3}\delta_{kl}\delta_{mn} \right] \quad . \tag{A.13}$$

Appendix B

Isochoric load application

The load application for unit cells with periodic boundary conditions is derived from the prescribed final deformation gradient. Thereby, the displacements of master nodes are determine for each increment of the simulation. For this purpose a python script is used, which is explained here in a descriptive manner.

The load case definition starts with a deformation gradient, $\mathbf{F}$, which describes the deformation state of the unit cell in the final state. The displacements of the master nodes are simply derived from the deformation gradient and the size of the unit cell as

$$\mathbf{u}^{\mathrm{SWB}} = \begin{pmatrix} 0 \\ 0 \\ 0 \end{pmatrix}, \quad \mathbf{u}^{\mathrm{SEB}} = \begin{pmatrix} (F_{11}-1)\,l_x \\ F_{12}\,l_y \\ F_{13}\,l_z \end{pmatrix}, \quad \mathbf{u}^{\mathrm{NWB}} = \begin{pmatrix} F_{21}\,l_x \\ (F_{22}-1)\,l_y \\ F_{23}\,l_z \end{pmatrix}, \quad \mathbf{u}^{\mathrm{SWT}} = \begin{pmatrix} F_{31}\,l_x \\ F_{32}\,l_y \\ (F_{33}-1)\,l_z \end{pmatrix}. \tag{B.1}$$

In the first step, the volume change $J = \det(\mathbf{F})$ of the deformation gradient is checked. If the volume is not preserved, each master node displacement is assigned with linear amplitude increase of the deformation gradient components.

If the prescribed deformation gradient is isochoric, the amplitude increase of the master node displacements are set dependently of each other in a way, that the volume

is preserved in each increment of the simulation. The increment size, number, and distribution is defined by the user.

The amplitude increase of the master node displacements are defined in the following way. The deformation gradient, $\mathbf{F}$, can be expressed as the product of the rotation altensor, $\mathbf{R}$, and the right stretch tensor, $\mathbf{U}$, using polar decomposition. Inherently, the principal stretches, λ_α, and the principal directions, $\mathbf{n}_\alpha$, are obtained from the eigenvalues and eigenvectors of the right Cauchy-Green tensor as

$$\mathbf{C} = \mathbf{U}^{\mathrm{T}}\mathbf{U} \tag{B.2}$$

$$= \sum_{\alpha=1}^{3} \lambda_\alpha^2 \mathbf{n}_\alpha \otimes \mathbf{n}_\alpha \quad . \tag{B.3}$$

Once the stretch tensor, $\mathbf{U}$, is known, the rotation tensor can be obtained as $\mathbf{R} = \mathbf{F}\mathbf{U}^{-1}$.

In general, a rotational matrix can be defined as a rotation by angle, θ, around a unit vector, $\mathbf{u}$, as

$$\mathbf{R} = \begin{bmatrix} u_x^2\left(1-\cos\left(\theta\right)\right)+\cos\left(\theta\right) & u_x u_y\left(1-\cos\left(\theta\right)\right)-u_z\sin\left(\theta\right) & u_x u_z\left(1-\cos\left(\theta\right)\right)+u_y\sin\left(\theta\right) \\ u_x u_y\left(1-\cos\left(\theta\right)\right)+u_z\sin\left(\theta\right) & u_y^2\left(1-\cos\left(\theta\right)\right)+\cos\left(\theta\right) & -u_x\sin\left(\theta\right)+u_y u_z\left(1-\cos\left(\theta\right)\right) \\ u_x u_z\left(1-\cos\left(\theta\right)\right)-u_y\sin\left(\theta\right) & u_x\sin\left(\theta\right)+u_y u_z\left(1-\cos\left(\theta\right)\right) & u_z^2\left(1-\cos\left(\theta\right)\right)+\cos\left(\theta\right) \end{bmatrix} \tag{B.4}$$

Thereby, a unit vector, $\mathbf{u}$, and rotation angle, θ, are solved for the rotational tensor, $\mathbf{R}$, obtained from the polar decomposition.

Next, the right stretch tensor, $\mathbf{U}$, is defined for each increment. If one of the principal stretches is equal to one, than the remaining two stretches are codependent. For example:

$$\text{if} \quad \lambda_1 = 1 : \qquad \lambda_2 = 1/\lambda_3 \tag{B.5}$$

$$\text{if} \quad \lambda_2 = 1 : \qquad \lambda_1 = 1/\lambda_3 \tag{B.6}$$

$$\text{if} \quad \lambda_3 = 1 : \qquad \lambda_1 = 1/\lambda_2 \tag{B.7}$$

In such case, linear amplitude increase is set to one of the codependent principal stretches, which inherently defines the amplitude of the second principal stretch.

If none of the principal stretches is equal to one, than the amplitudes of the first two principal stretches, i.e. λ_1 and λ_2, are set with linear increase, while the amplitude increase of the third principal stretch is defined from the relation

$$\lambda_3 = \frac{1}{\lambda_1 \lambda_2} \,. \tag{B.8}$$

Thereby, principal stretches are defined for each increment and consequently the incremental right stretch tensor as

$$\mathbf{U}^{(n)} = \sum_{\alpha=1}^{3} \lambda_\alpha^{(n)} \mathbf{n}_\alpha \otimes \mathbf{n}_\alpha \,, \tag{B.9}$$

where $^{(n)}$ denotes the increment. By adding the rotation of the stretch in an incremental way, i.e. by linear incremental increase of the angle from zero to θ around the unit vector $\mathbf{u}$, the incremental deformation gradient is obtained as

$$\mathbf{F}^{(n)} = \mathbf{R}^{(n)} \mathbf{U}^{(n)} \quad . \tag{B.10}$$

The incremental deformation gradient is than used to define displacements of the master nodes, Eq. (B.1) for each increment. Note that if the increment is changed (decreased) by the automatic simulation control, than the displacements are linearly

interpolated between the closest known values. For this reason it is important to set a high enough number of increments.

Bibliography

[1] M. Agoras, O. Lopez-Pamies, and P. Ponte Castañeda. A general hyperelastic model for incompressible fiber-reinforced elastomers. *Journal of the Mechanics and Physics of Solids*, 57(2):268–286, feb 2009.

[2] Airbus. Composites in Airbus. `https://www.airbusgroup.com/dam/assets/airbusgroup/int/en/investor-relations/documents/2008/presentations/GIF2008/gif2008_workshop_composites_hellard.pdf`. viewed: November 2016.

[3] G. Alfano and M. Crisfield. Finite element interface models for the delamination analysis of laminated composites: mechanical and computational issues. *International Journal for Numerical Methods in Engineering*, 50(7):1701–1736, 2001.

[4] N. Alif, L. A. Carlsson, and L. Boogh. The effect of weave pattern and crack propagation direction on mode I delamination resistance of woven glass and carbon composites. *Composites Part B: Engineering*, 29(5):603–611, sep 1998.

[5] G. I. Barenblatt et al. The mathematical theory of equilibrium cracks in brittle fracture. *Advances in Applied Mechanics*, 7(1):55–129, 1962.

[6] W. Bascom, J. Bitner, R. Moulton, and A. Siebert. The interlaminar fracture of organic-matrix, woven reinforcement composites. *Composites*, 11(1):9–18, jan 1980.

[7] K.-J. Bathe and E. L. Wilson. Large eigenvalue problems in dynamic analysis. *Journal of the Engineering Mechanics Division*, 98(6):1471–1485, 1972.

[8] M. Benzeggagh and M. Kenane. Measurement of mixed-mode delamination fracture toughness of unidirectional glass/epoxy composites with mixed-mode bending apparatus. *Composites Science and Technology*, 56:439–449, 1968.

[9] M. L. Benzeggagh and M. Kenane. Measurement of mixed-mode delamination fracture toughness of unidirectional glass/epoxy composites with mixed-mode bending apparatus. *Composites Science and Technology*, 56(4):439–449, 1996.

[10] H. J. Böhm. A short introduction to basic aspects of continuum micromechanics. *Cdl-fmd Report*, 3, 1998.

[11] H. J. Böhm. *Mechanics of microstructured materials*, volume 464. Springer, 2014.

[12] J. Bonhomme, A. Argüelles, J. Viña, and I. Viña. Fractography and failure mechanisms in static mode I and mode II delamination testing of unidirectional carbon reinforced composites. *Polymer Testing*, 28(6):612–617, sep 2009.

[13] M. Brun, O. Lopez-Pamies, and P. Ponte Castañeda. Homogenization estimates for fiber-reinforced elastomers with periodic microstructures. *International Journal of Solids and Structures*, 44(18-19):5953–5979, sep 2007.

[14] P. Camanho, C. Dávila, and M. D. Moura. Numerical Simulation of Mixed-mode Progressive Delamination in Composite Materials. *Journal of Composite Materials*, 37(16):1415–1438, 2003.

[15] P. P. Camanho and C. G. Dávila. Mixed-mode decohesion finite elements for the simulation of delamination in composite materials, 2002.

[16] P. Castañeda. The effective mechanical properties of nonlinear isotropic composites. *Journal of the Mechanics and Physics of Solids*, 39(1):45–71, jan 1991.

[17] P. P. Castañeda. Exact second-order estimates for the effective mechanical properties of nonlinear composite materials. *Journal of the Mechanics and Physics of Solids*, 44(6):827–862, 1996.

[18] P. P. Castaneda. Second-order homogenization estimates for nonlinear composites incorporating field fluctuations: I—theory. *Journal of the Mechanics and Physics of Solids*, 50(4):737–757, 2002.

[19] R. Christensen, H. Schantz, J. Shapiro, et al. On the range of validity of the mori-tanaka method. *Journal of the Mechanics and Physics of Solids*, 40(1): 69–73, 1992.

[20] C. Chuong and Y. Fung. Three-dimensional stress distribution in arteries. *Journal of Biomechanical Engineering*, 105(3):268–274, 1983.

[21] F. Dadgar-Rad and A. Imani. Theory of gradient-elastic membranes and its application in the wrinkling analysis of stretched thin sheets. *Journal of the Mechanics and Physics of Solids*, 132:103679, 2019.

[22] *Abaqus Documentation, version 2019*. Dassault Systèmes Simulia Corp., Providence, RI, USA, 2017.

[23] *Abaqus Documentation*. Dassault Systèmes Simulia Corp., Providence, RI, USA, version 2020.

[24] L. Datashvili, N. Nathrath, M. Lang, H. Baier, D. Fasold, and S. Pellegrino. New Concepts and Reflecting Materials for Space Borne Large Deployable Reflector Antennas. *28th ESA Antenna Workshop on Space Antenna Systems and Technologies*, (1):1–8, 2005.

[25] P. Davies, B. Blackman, and A. Brunner. Mode II delamination. In D. Moore, A. Pavan, and J. Williams, editors, *Fracture mechanics testing methods for polymers adhesives and composites*, pages 307–334. Elsevier Amsterdam, London, New York, 2001.

[26] G. DeBotton. Transversely isotropic sequentially laminated composites in finite elasticity. *Journal of the Mechanics and Physics of Solids*, 53(6):1334–1361, jun 2005.

[27] G. DeBotton, I. Hariton, and E. Socolsky. Neo-Hookean fiber-reinforced composites in finite elasticity. *Journal of the Mechanics and Physics of Solids*, 54 (3):533–559, mar 2006.

[28] DIN EN 6033:2015. Aerospace series - Carbon fibre reinforced plastics - Test method - Determination of interlaminar fracture toughness energy - Mode I - GIC, 2016.

[29] DIN EN 6034:2013. Aerospace series - Carbon fibre reinforced plastics - Test method - Determination of interlaminar fracture toughness energy - Mode II - G_{II}, 2016.

[30] D. S. Dugdale. Yielding of steel sheets containing slits. *Journal of the Mechanics and Physics of Solids*, 8(2):100–104, 1960.

[31] N. Friedl, F. Rammerstorfer, and F. Fischer. Buckling of stretched strips. *Computers & Structures*, 78(1-3):185–190, nov 2000.

[32] C. Fu, T. Wang, F. Xu, Y. Huo, and M. Potier-Ferry. A modeling and resolution framework for wrinkling in hyperelastic sheets at finite membrane strain. *Journal of the Mechanics and Physics of Solids*, 124:446–470, mar 2019.

[33] Y. Fung, K. Fronek, and P. Patitucci. Pseudoelasticity of arteries and the choice of its mathematical expression. *American Journal of Physiology-Heart and Circulatory Physiology*, 237(5):H620–H631, 1979.

[34] C. M. Gabardo, R. C. Adams-McGavin, B. C. Fung, E. J. Mahoney, Q. Fang, and L. Soleymani. Rapid prototyping of all-solution-processed multi-lengthscale electrodes using polymer-induced thin film wrinkling. *Scientific Reports*, 7(1): 1–9, 2017.

[35] J. Gager and H. Pettermann. Numerical homogenization of textile composites based on shell element discretization. *Composites Science and Technology*, 72 (7):806–812, 2012.

[36] J. Gager and H. Pettermann. Fem modeling of multilayered textile composites based on shell elements. *Composites Part B: Engineering*, 77:46–51, 2015.

[37] K. C. Galloway, P. Polygerinos, C. J. Walsh, and R. J. Wood. Mechanically programmable bend radius for fiber-reinforced soft actuators. In *2013 16th International Conference on Advanced Robotics (ICAR)*, pages 1–6. IEEE, nov 2013.

[38] T. C. Gasser, R. W. Ogden, and G. A. Holzapfel. Hyperelastic modelling of arterial layers with distributed collagen fibre orientations. *Journal of The Royal Society Interface*, 3(6):15–35, 2005.

[39] Q. Ge, X. Luo, E. D. Rodriguez, X. Zhang, P. T. Mather, M. L. Dunn, and H. J. Qi. Thermomechanical behavior of shape memory elastomeric composites. *Journal of the Mechanics and Physics of Solids*, 60(1):67–83, jan 2012.

[40] H. Hadavinia and H. Ghasemnejad. Effects of mode-i and mode-ii interlaminar fracture toughness on the energy absorption of cfrp twill/weave composite box sections. *Composite Structures*, 89(2):303–314, 2009.

[41] P. W. Harper and S. R. Hallett. Cohesive zone length in numerical simulations of composite delamination. *Engineering Fracture Mechanics*, 75(16):4774–4792, nov 2008.

[42] S. Hashemi, A. Kinloch, and J. Williams. The analysis of interlaminar fracture in uniaxial fibre-polymer composites. *Proceedings of the Royal Society of London. Series A*, 427:173–199, 1990.

[43] Z. Hashin. Failure criteria for unidirectional fiber composites. *Journal of Applied Mechanics*, 47(2):329–334, 1980.

[44] Z. Hashin and A. Rotem. A fatigue failure criterion for fiber reinforced materials. *Journal of Composite Materials*, 7(4):448–464, 1973.

[45] T. J. Healey, Q. Li, and R. B. Cheng. Wrinkling behavior of highly stretched rectangular elastic films via parametric global bifurcation. *Journal of Nonlinear Science*, 23(5):777–805, oct 2013.

[46] A. Hillerborg, M. Modéer, and P.-E. Petersson. Analysis of crack formation and crack growth in concrete by means of fracture mechanics and finite elements. *Cement and Concrete Research*, 6(6):773–781, 1976.

[47] C. Hochard, P.-A. Aubourg, and J.-P. Charles. Modelling of the mechanical behaviour of woven-fabric CFRP laminates up to failure. *Composites Science and Technology*, 61(2):221–230, feb 2001.

[48] G. A. Holzapfel. Comparison of a Multi-Layer Structural Model for Arterial Walls With a Fung-Type Model, and Issues of Material Stability. *Journal of Biomechanical Engineering*, 126(2):264, may 2004.

[49] G. A. Holzapfel, T. C. Gasser, and R. W. Ogden. A new constitutive framework for arterial wall mechanics and a comparative study of material models. *Journal of Elasticity*, 61(1-3):1–48, 2000.

[50] G. A. Holzapfel, T. C. Gasser, and M. Stadler. A structural model for the viscoelastic behavior of arterial walls: Continuum formulation and finite element analysis. *European Journal of Mechanics, A/Solids*, 21(3):441–463, 2002.

[51] J. Huang, M. Juszkiewicz, W. H. De Jeu, E. Cerda, T. Emrick, N. Menon, and T. P. Russell. Capillary wrinkling of floating thin polymer films. *Science*, 317 (5838):650–653, 2007.

[52] W. Hufenbach, A. Hornig, M. Gude, R. Böhm, and F. Zahneisen. Influence of interface waviness on delamination characteristics and correlation of through-

thickness tensile failure with mode I energy release rates in carbon fibre textile composites. *Materials & Design*, 50:839–845, sep 2013.

[53] J. D. Humphrey. Mechanics of the arterial wall: review and directions. *Critical Reviews™ in Biomedical Engineering*, 23(1-2), 1995.

[54] M. Kanninen and C. Popelar. *Advanced Fracture Mechanics*. Oxford Engineering Science Series. Oxford University Press, 1985.

[55] M. Kessler and S. White. Self-activated healing of delamination damage in woven composites. *Composites Part A: Applied Science and Manufacturing*, 32 (5):683–699, may 2001.

[56] Z. Khisaeva and M. Ostoja-Starzewski. Mesoscale bounds in finite elasticity and thermoelasticity of random composites. *Proceedings of the Royal Society A: Mathematical, Physical and Engineering Sciences*, 462(2068):1167–1180, apr 2006.

[57] Z. F. Khisaeva and M. Ostoja-Starzewski. On the size of RVE in finite elasticity of random composites. *Journal of Elasticity*, 85(2):153–173, nov 2006.

[58] J.-K. Kim and M.-L. Sham. Impact and delamination failure of woven-fabric composites. *Composites Science and Technology*, 60(5):745–761, apr 2000.

[59] I. Lapczyk and J. A. Hurtado. Progressive damage modeling in fiber-reinforced materials. *Composites Part A: Applied Science and Manufacturing*, 38(11): 2333–2341, 2007.

[60] Q. Li and T. J. Healey. Stability boundaries for wrinkling in highly stretched elastic sheets. *Journal of the Mechanics and Physics of Solids*, 2016.

[61] Z. Li, Y. Zhai, Y. Wang, G. M. Wendland, X. Yin, and J. Xiao. Harnessing surface wrinkling–cracking patterns for tunable optical transmittance. *Advanced Optical Materials*, 5(19):1700425, 2017.

[62] F. Liu, F. Xu, and C. Fu. Orientable wrinkles in stretched orthotropic films. *Extreme Mechanics Letters*, 33:100579, 2019.

[63] F. López Jiménez. On the isotropy of randomly generated representative volume elements for fiber-reinforced elastomers. *Composites Part B: Engineering*, 87: 33–39, feb 2016.

[64] O. Lopez-Pamies and P. P. Castañeda. Second-order estimates for the macroscopic response and loss of ellipticity in porous rubbers at large deformations. *Journal of Elasticity*, 76(3):247–287, sep 2004.

[65] O. Lopez-Pamies and P. P. Castañeda. On the overall behavior, microstructure evolution, and macroscopic stability in reinforced rubbers at large deformations: II - Application to cylindrical fibers. *Journal of the Mechanics and Physics of Solids*, 54(4):831–863, 2006.

[66] O. Lopez-Pamies and P. P. Castañeda. On the overall behavior, microstructure evolution, and macroscopic stability in reinforced rubbers at large deformations: II - Application to cylindrical fibers. *Journal of the Mechanics and Physics of Solids*, 54(4):831–863, 2006.

[67] X. Luo and P. T. Mather. Preparation and characterization of shape memory elastomeric composites. *Macromolecules*, 42(19):7251–7253, 2009.

[68] M. Mansouri, P. Fuchs, J. Criscione, B. Schrittesser, and J. Beter. The contribution of mechanical interactions to the constitutive modeling of fiber-reinforced elastomers. *European Journal of Mechanics-A/Solids*, 85:104081, 2020.

[69] J. Mejia-Ariza, T. Murphey, and E. Pollard. Manufacture and Experimental Analysis of a Concentrated Strain Based Deployable Truss Structure. In *47th AIAA/ASME/ASCE/AHS/ASC Structures, Structural Dynamics, and Materials Conference 14th AIAA/ASME/AHS Adaptive Structures Conference 7th*, Reston, Virigina, may 2006. American Institute of Aeronautics and Astronautics.

[70] Y. Mi, M. Crisfield, G. Davies, and H. Hellweg. Progressive delamination using interface elements. *Journal of Composite Materials*, 32(14):1246–1272, 1998.

[71] J. Michel, H. Moulinec, and P. Suquet. Effective properties of composite materials with periodic microstructure: a computational approach. *Computer Methods in Applied Mechanics and Engineering*, 172(1-4):109–143, apr 1999.

[72] J. Moraleda, J. Segurado, and J. LLorca. Finite deformation of incompressible fiber-reinforced elastomers: A computational micromechanics approach. *Journal of the Mechanics and Physics of Solids*, 57(9):1596–1613, sep 2009.

[73] T. Mori and K. Tanaka. Average stress in matrix and average elastic energy of materials with misfitting inclusions. *Acta Metallurgica*, 21(5):571–574, 1973.

[74] J.-y. Nagase, S. Wakimoto, T. Satoh, N. Saga, and K. Suzumori. Design of a variable-stiffness robotic hand using pneumatic soft rubber actuators. *Smart Materials and Structures*, 20(10):105015, oct 2011.

[75] V. Nayyar, K. Ravi-Chandar, and R. Huang. Stretch-induced stress patterns and wrinkles in hyperelastic thin sheets. *International Journal of Solids and Structures*, 2011.

[76] J. F. Nye et al. *Physical properties of crystals: their representation by tensors and matrices*. Oxford university press, 1985.

[77] T. Ogasawara, A. Yoshimura, T. Ishikawa, R. Takahashi, N. Sasaki, and T. Ogawa. Interlaminar fracture toughness of 5 harness satin woven fabric carbon fiber/epoxy composites. *Advanced Composite Materials*, 21(1):45–56, 2012.

[78] R. W. Ogden. *Non-linear elastic deformations*. Courier Corporation, 1997.

[79] P. Polygerinos, Z. Wang, J. T. B. Overvelde, K. C. Galloway, R. J. Wood, K. Bertoldi, and C. J. Walsh. Modeling of Soft Fiber-Reinforced Bending Actuators. *IEEE Transactions on Robotics*, 31(3):778–789, jun 2015.

[80] F. G. Rammerstorfer. Buckling of elastic structures under tensile loads. *Acta Mechanica*, 229(2):881–900, 2018.

[81] F. Rehnmark, M. Pryor, B. Holmes, D. Schaechter, N. Pedreiro, and C. Carrington. Development of a Deployable Nonmetallic Boom for Reconfigurable Systems of Small Spacecraft. In *48th AIAA/ASME/ASCE/AHS/ASC Structures, Structural Dynamics, and Materials Conference*, Reston, Virigina, apr 2007. American Institute of Aeronautics and Astronautics.

[82] J. Schön, T. Nyman, A. Blom, and H. Ansell. Numerical and experimental investigation of a composite ENF-specimen. *Engineering Fracture Mechanics*, 65(4):405–433, mar 2000.

[83] M. Schwab and H. E. Pettermann. Modelling and simulation of damage and failure in large composite components subjected to impact loads. *Composite Structures*, 158:208–216, 2016.

[84] M. Schwab, M. Todt, and H. E. Pettermann. Simulation of the intermediate velocity impact behaviour of woven composite laminates applying progressive damage models for plies and interfaces. In O. Thomsen, C. Berggreen, and B. Sørensen, editors, *Proceedings of the 20th International Conference on Composite Materials, Paper-ID 4417-4*, 2015.

[85] M. Schwab, M. Todt, and H. E. Pettermann. A multiscale approach for modelling impact on woven composites under consideration of the fabric topology. *Journal of Composite Materials*, 52(21):2859–2874, 2018.

[86] A. J. M. Spencer. Constitutive Theory for Strongly Anisotropic Solids. In *Continuum Theory of the Mechanics of Fibre-Reinforced Composites*, pages 1–32. Springer Vienna, Vienna, 1984. doi: 10.1007/978-3-7091-4336-0_1. URL `http://link.springer.com/10.1007/978-3-7091-4336-0{_}1`.

[87] K. Suzumori, S. Endo, T. Kanda, N. Kato, and H. Suzuki. A Bending Pneumatic Rubber Actuator Realizing Soft-bodied Manta Swimming Robot. In

Proceedings 2007 IEEE International Conference on Robotics and Automation, pages 4975–4980. IEEE, apr 2007.

[88] M. Taylor and M. Shirani. Simulation of wrinkling in incompressible anisotropic thin sheets with wavy fibers. *International Journal of Non-Linear Mechanics*, 127(August):103610, 2020.

[89] M. Taylor, K. Bertoldi, and D. J. Steigmann. Spatial resolution of wrinkle patterns in thin elastic sheets at finite strain. *Journal of the Mechanics and Physics of Solids*, 2014.

[90] A. Turon, P. Camanho, J. Costa, and C. Dávila. A damage model for the simulation of delamination in advanced composites under variable-mode loading. *Mechanics of Materials*, 38(11):1072–1089, nov 2006.

[91] A. Turon, C. Dávila, P. Camanho, and J. Costa. An engineering solution for mesh size effects in the simulation of delamination using cohesive zone models. *Engineering Fracture Mechanics*, 74(10):1665–1682, jul 2007.

[92] A. Turon, C. G. Davila, P. P. Camanho, and J. Costa. An engineering solution for mesh size effects in the simulation of delamination using cohesive zone models. *Engineering Fracture Mechanics*, 74(10):1665–1682, 2007.

[93] A. Turon, P. Camanho, J. Costa, and J. Renart. Accurate simulation of delamination growth under mixed-mode loading using cohesive elements: definition of interlaminar strengths and elastic stiffness. *Composite Structures*, 92(8): 1857–1864, 2010.

[94] L. Walpole. On the overall elastic moduli of composite materials. *Journal of the Mechanics and Physics of Solids*, 17(4):235–251, 1969.

[95] Y. Wang, C. Gregory, and M. A. Minor. Improving Mechanical Properties of Molded Silicone Rubber for Soft Robotics Through Fabric Compositing. *Soft Robotics*, 5(3):272–290, jun 2018.

[96] J. P. Wilber and J. R. Walton. The convexity properties of a class of constitutive models for biological soft issues. *Mathematics and Mechanics of Solids*, 7(3): 217–235, 2002.

[97] J. Williams. The fracture mechanics of delamination tests. *The Journal of Strain Analysis for Engineering Design*, 24(4):207–214, 1989.

[98] T. Yamanaka, H. Ghiasi, M. Heidari-Rarani, L. Lessard, V. Feret, and P. Hubert. Multiscale finite element analysis of mode I delamination growth in a fabric composite. *Composite Structures*, 133:157–165, dec 2015.

[99] H. Yang, X.-F. Yao, H. Yan, Y.-n. Yuan, Y.-F. Dong, and Y.-H. Liu. Anisotropic hyper-viscoelastic behaviors of fabric reinforced rubber composites. *Composite Structures*, 187:116–121, mar 2018.

[100] Q. Yang and B. Cox. Cohesive models for damage evolution in laminated composites. *International Journal of Fracture*, 133(2):107–137, 2005.

[101] Y. Yang, C. Fu, and F. Xu. A finite strain model predicts oblique wrinkles in stretched anisotropic films. *International Journal of Engineering Science*, 155: 103354, 2020.

[102] Y. Yu, L. Ye, Y. Song, Y. Guan, and J. Zang. Wrinkled nitrile rubber films for stretchable and ultra-sensitive respiration sensors. *Extreme Mechanics Letters*, 11:128–136, 2017.

[103] C. Zener. *Elasticity and anelasticity of metals*. University of Chicago press, 1948.